UNIVERSITÄTSKLINIKUM HAMBURG-EPPENDORF

Klinik und Poliklinik für Neurologie

Prof. Dr. med. Tim Magnus und Prof. Dr. med. Götz Thomalla

Multimodal Investigation of the Cerebello-thalamo-cortical Network in Parkinson's Disease Tremor

Dissertation

zur Erlangung des Doktorgrades PhD

an der Medizinischen Fakultät der Universität Hamburg

vorgelegt von:

Fatemeh Sadeghi

aus Teheran (Iran)

Hamburg 2024

Angenommen von der
Medizinischen Fakultät der Universität Hamburg am: 16.12.2024

Veröffentlicht mit Genehmigung der
Medizinischen Fakultät der Universität Hamburg.

Prüfungsausschuss, der/die Vorsitzende: PD Dr. Simone Zittel-Dirks

Prüfungsausschuss, zweite/r Gutachter/in: Prof. Dr. Andreas K. Engel

The present work has been conducted from October 2020 until October 2023 in the Department of Neurology at the University Medical Center Hamburg-Eppendorf under the supervision of Priv. -Doz. Dr. Simone Zittel, with further supervision from Prof. Dr. Christian Gerloff.

To cite this dissertation:

Sadeghi, Fatemeh. Multimodal Investigation of the Cerebello-thalamo-cortical Network in Parkinson's Disease Tremor. 2024, Universität Hamburg, Doctoral dissertation. URN: urn:nbn:de:gbv:18-ediss-124699

Table of Contents

List of Figures

Supplementary Figures

List of Tables

Supplementary Tables

Chapter 1 : General Introduction

1.1 Parkinson's Disease

Parkinson's disease (PD), the second most prevalent neurodegenerative disorder, impacts 2–3% of individuals over 65 (Poewe et al., 2017). Its prevalence has risen over the past two decades, influenced by ageing demographics and advancements in diagnostic methods (Bloem et al., 2021; Maclagan et al., 2023). The age-related increase in PD is evident, ranging from 41 per 100,000 in the 40-49 age group to 1,903 per 100,000 in the population over 80 years old (Pringsheim et al., 2014). In Germany, a unique trend is observed with a prevalence of 1.6%, peaking in individuals older than 90 years and exhibiting higher rates in men.

This incapacitating movement disorder is diagnosed primarily based on the manifestation of motor symptoms. According to the Movement Disorder Society Clinical Diagnostic Criteria for PD, bradykinesia should be present, combined with rigidity or tremor or both even in the early stages (Berg et al., 2018; Postuma et al., 2015). Bradykinesia is characterized by slowness of movement with a decrease in movement amplitude or speed. Rigidity refers to an increased muscle tone leading to a resistance to passive movement in major joints (Postuma et al., 2015). Tremor is defined by the involuntary rhythmic movement of the distal limbs, predominantly hands, at a frequency of 4 to 6 Hz (Bhatia et al., 2018; Helmich, 2018). When the movement is observed in a resting limb, it is identified as rest tremor. This type of tremor is the most prevalent by affecting approximately 70% of PD patients and serves as a critical diagnostic marker (Gupta et al., 2020). However, tremor can also appear during voluntary limb movement, known as kinetic tremor, or as the arm is held in a specific position or posture, referred to as postural tremor (Bhatia et al., 2018).

Movement Disorder Society-Sponsored Revision of the Unified Parkinson's Disease Rating Scale (MDS-UPDRS) is the standardized and essential tool for evaluating the range and severity of PD symptoms (Christopher G Goetz et al., 2008; Postuma et al., 2015). In particular, parts II and III involve a self-based and a clinician-based assessment of motor symptoms respectively. Based on the balance ratio between MDS-UPDRS tremor scores and postural instability and gait difficulty scores, PD patients can be clinically categorized into tremor-dominant (TD), indeterminate (ID), or postural instability/gait disorders (PIGD) subtypes (Stebbins et al., 2013). Tremor-dominant subtype indicates slower disease progression and a lower probability of developing dementia (Toni et al., 2012).

The neuropathological hallmark of PD includes the widespread aggregation of α-synuclein in the form of Lewy bodies, primarily in the substantia nigra (SN). This aggregation disrupts dopamine signalling and contributes to the degeneration of dopaminergic neurons in this region (Choong and Mochizuki, 2022; Kalia and Lang, 2015). The loss of dopamine, in turn, disrupts the normal balance of excitatory and inhibitory signals in the basal ganglia, affecting motor control (Wu et al., 2012). This imbalance leads to altered output from the basal ganglia to the thalamus and subsequently to the motor cortex, impairing the initiation and execution of voluntary movements (Chen et al., 2023; Martel and Galvan, 2022). Furthermore, the cerebellum, which plays a crucial role in fine-tuning motor actions and coordination, receives abnormal input due to the disrupted circuitry, leading to further motor deficits (Wu

and Hallett, 2013; Xu et al., 2019). These changes are accompanied by altered interactions between the entire basal ganglia-motor cortex-cerebellum network, which explains the key motor symptoms of PD including tremor, freezing, and impairments in action sequencing, and highlights PD as a system-level disorder (Caligiore et al., 2016; Helmich, 2018).

Tremor is a prominent symptom of PD due to its distinct neural mechanisms compared to other motor symptoms such as bradykinesia or rigidity and its response to dopaminergic medication is notably inconsistent (Helmich, 2018). Although the pathophysiology of PD tremor is not fully understood, it is known that tremor has its unique oscillatory signature in the brain, implicates multiple regions, and is associated with network connectivity impairments mentioned above (Hallett, 2012).

1.2 The Role of the CTC Network in PD Tremor

Numerous hypotheses have been proposed to elucidate the mechanism underlying the tremor in PD, such as the Thalamic Pacemaker, the Subthalamic Nucleus (STN)-External Globus Pallidus (GPe) Pacemaker, and the Loss-of-Segregation Hypothesis (Zhong et al., 2022). Among these, the 'dimmer-switch' model as proposed by Helmich et al. (2018) provides a comprehensive theory for describing PD tremor generation and extension across multiple brain networks. This model is grounded in experimental evidence that links tremor activity to a variety of functional and metabolic irregularities throughout the brain while accounting for the regional neurophysiological intricacies. According to this framework, the basal ganglia are the initial site for PD tremor, referred to as 'the switch' that is activated by the degeneration of dopaminergic neurons. This neuronal loss leads to subsequent disturbances in dopamine-mediated synaptic connections within the basal ganglia. Consequently, these disruptions result in altered functional connectivity (FC) in the basal ganglia-thalamo-cortical (BTC) circuitry, manifesting as pathological bursting activities. The tremor-related pathological activity further propagates to implicate the cerebello-thalamo-cortical (CTC) network or 'the dimmer' due to hyper-synchronisation between the BTC and CTC networks in the tremor state. Consequently, the tremor oscillation is maintained and amplified with the CTC network (Dirkx and Bologna, 2022; Duval et al., 2016; Helmich, 2018; Helmich et al., 2021). The model schematics are presented in Figure 1.

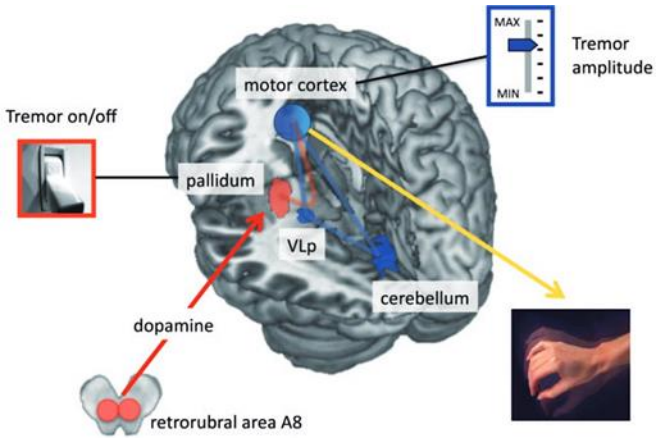

Figure 1. The dimmer-switch model of tremor in PD. The basal ganglia act as 'the switch', activated by dopaminergic neuron degeneration. This disruption alters the basal ganglia-thalamo-cortical (BTC) network connectivity, leading to pathological bursting activity. This tremor-related oscillatory activity then propagates to the cerebello-thalamo-cortical (CTC) network ('the dimmer'), where the tremor oscillations are amplified (Dirkx and Bologna, 2022; Helmich, 2018).

Within a similar but extended paradigm, Duval et al. have introduced the 'finger-dimmer-switch' (FDS) model (Duval et al., 2016). This model breaks down the tremor generation process into distinct stages of initiation and consolidation. Tremor initiation is attributed to pathological neuronal activities within the basal ganglia, referred to as ‘the finger’. This neural activity remains as transient bursts until they are projected from the globus pallidus internus (GPi) to the thalamus, where they become entwined in a complex interplay of excitatory and inhibitory mechanisms among thalamic nuclei. Within the inner circuitry of the thalamus, these bursts manifest an oscillatory rhythm, therefore it is the thalamus which is metaphorically referred to as ‘the switch’ in this model. Subsequently, the CTC gets involved through the thalamus and takes on ‘the dimmer’ role similar to the previous model. The FDS model integrates specific experimental findings that highlight the thalamus's pivotal role in modulating PD tremor. The thalamus possesses a distinctive intrinsic self-regulation mechanism which is facilitated by excitatory inputs from the anterior and posterior ventrolateral thalamic nuclei (VLa and VLp, respectively) to the thalamic reticular nucleus (TRN), and the corresponding inhibitory feedback from the TRN to these ventrolateral nuclei (Duval et al., 2016; Huguenard and McCormick, 2007; Paré et al., 1990).

1.3 The Role of the Cerebellum in PD Tremor

The cerebellum plays a crucial role in coordinating voluntary movements, maintaining balance and posture, and integrating sensory inputs to fine-tune motor activities (Paulin, 2008). Interestingly, this region is involved in various types of limb tremor, mainly with distinct cerebello-cortical fingerprints (Caligiore et al., 2017; Muthuraman et al., 2018). In PD tremor, the cerebellum is implicated structurally, functionally, and as part of the CTC network. Significant structural alterations include cellular level alterations, including the aggregation of α-synuclein-formed Lewy bodies and Purkinje cell loss, decreased grey matter volume and white matter abnormalities in the middle and superior cerebellar peduncles, as well as iron accumulation within its deep nuclei (Piao et al., 2003; Rusholt et al., 2020; Takada et al., 1993; Vignola et al., 1994; Wu and Hallett, 2013).

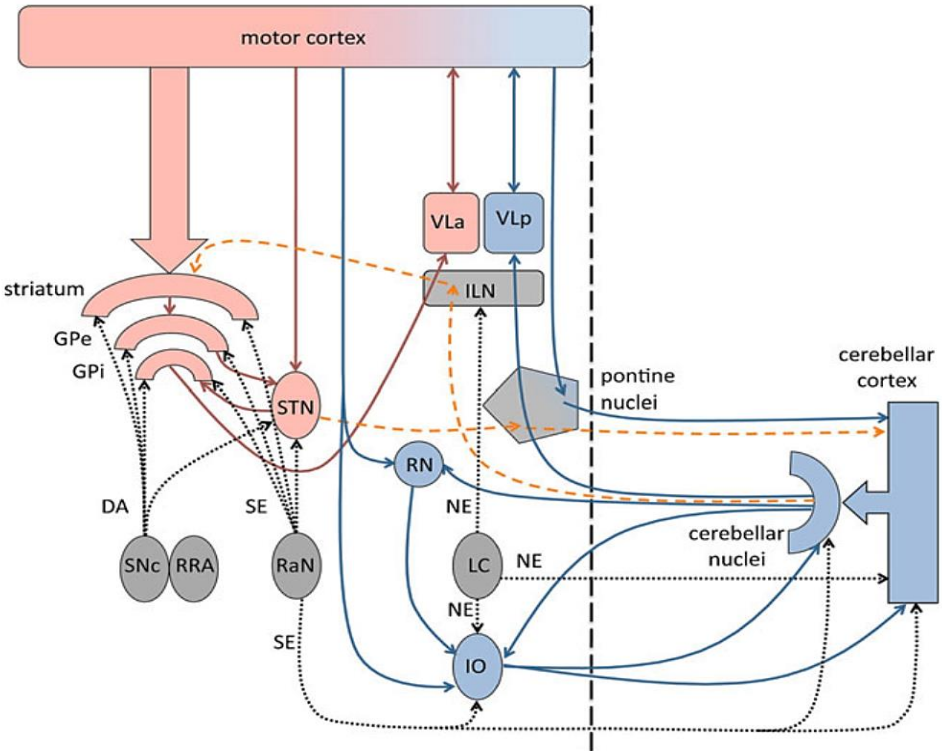

Figure 2. Cerebellar contribution to tremor pathophysiology. The cerebellar system and its connections within the CTC network are depicted in blue, medicated through the cerebellar nuclei, mainly the dentate nucleus, emphasizing its role in the anatomical framework of tremor. The BTC network, responsible for the generation of tremor is shown in red, and its interactions with the cerebellum are marked by dashed yellow lines. The dotted black lines represent the modulatory neurotransmitter projections (Helmich et al., 2013).

Functionally, tremor oscillations can be directly traced from the cerebellum to the arm muscles, highlighting the cerebellum's key role in driving tremor (Muthuraman et al., 2018). Furthermore, glucose metabolism and connectivity patterns are altered in the cerebellum of PD patients with tremor, and the activity in the cerebellar cortex and nuclei are increased in association with tremor severity (Bharti et al., 2019; Caligiore et al., 2017; Zhong et al., 2022). Of note, the mentioned cerebellar deep nuclei, particularly the dentate nucleus (DN), serve as relay nodes that receive projections from cerebellar hemispheres and send output projections to the ventrolateral thalamus and subsequently to the cerebral cortex (Miall, 2022). Figure 2 illustrates the cerebellum's functional role in tremor pathophysiology. It highlights the cerebellum's extensive and interactive connections within the CTC network and its further interactions with the BTC network and other relevant brain regions. The network-level role of the cerebellum in PD tremor predominantly involves the maintenance and amplification of the rhythmic activity within the CTC network. More details have been provided in the section 1.2 on the topic of the FDS theory (Helmich, 2018). Given that the cerebellum is a critical node within the CTC network and exhibits both pathological and compensatory roles in PD tremor (Wu and Hallett, 2013), focusing on this region can help reveal network-level dynamics underlying tremor pathophysiology. Moreover, the cerebellum is readily accessible as a target for transcranial non-invasive brain stimulation (NIBS) techniques, making it a viable target for both research investigations and therapeutic interventions.

Chapter 2 : Material and Methods

2.1 Magnetic Resonance Imaging

Magnetic resonance imaging (MRI) is an imaging technique that uses the unique properties of atomic nuclei possessing nonzero spin when subjected to a robust magnetic field to generate images (Plewes and Kucharczyk, 2012). This method involves positioning the individual within a potent magnetic field and subjecting them to transient pulses of electromagnetic energy, leading to an alteration in the spin orientations of protons. Upon cessation of the energy pulse, these spins undergo a relaxation process, realigning back to their equilibrium state. The speed at which this realignment occurs varies based on the nuclei's chemical surroundings, enabling the MR signals gathered during this process to be transformed into detailed anatomical visuals of the targeted tissues (Grover et al., 2015; Plewes and Kucharczyk, 2012). Additionally, this technique's sensitivity to different tissue environments allows for the distinction between various types of tissues, demonstrating the diagnostic capabilities of MRI in identifying abnormalities and diseases within the body (Grover et al., 2015).

Conventional three-dimensional T1-weighted (T1-w) sequences are acclaimed for their ability to provide high contrast between grey and white matter, particularly within the cortex and certain basal ganglia structures. This capability facilitates detailed volumetric and morphometric analyses, enabling the detection of subtle changes in cortical volume and thickness as well as morphological alterations within the regions involved in PD (Benninger et al., 2009; Kerestes et al., 2023; Schwarz et al., 2011). In addition to anatomical imaging techniques, diffusion-based methods such as diffusion-weighted imaging (DWI) and tractography can reveal water diffusion in biological tissues and enable the reconstruction of fibre tracts, respectively. Using these sequences, reduced fractional anisotropy (FA) and a decreased likelihood of connections have been reported in PD, shedding light on the disease's impact on brain connectivity (Pyatigorskaya et al., 2014). Functional MRI (fMRI) further expands the utility of MRI in PD research by focusing on the brain's functional aspects. Conventional fMRI relies on detecting changes in blood oxygenation level-dependent (BOLD) contrast, which reflects variations in deoxygenated haemoglobin concentration. By analysing the synchronisation or temporal correlation of fMRI signals across different brain areas, researchers can infer FC. This approach has been instrumental in studying the functional architecture of the brain and its alteration in PD, offering valuable insights into the disease's pathophysiology and potential therapeutic targets (Matthews and Jezzard, 2004; Weingarten et al., 2015).

2.1.1 MRI-based Biomarkers in PD

Biomarkers are quantifiable indicators of biological or pathological states and are particularly valuable when derived from MRI data (Califf, 2018). MRI can identify specific alterations in the brain’s morphology, structure, or function that are characteristic of a certain disease, such as PD (Bidesi et al., 2021). These biomarkers are crucial for reflecting the presence, severity, and progression of the disease, offering the potential for early diagnosis and prognosis (Pyatigorskaya et al., 2014). This is especially important in PD, where early detection of neuropathological features and understanding of the mechanisms of neurodegeneration are essential. Some key pathological hallmarks of PD have been

identified through biomarkers, such as the elevated iron levels and α-synuclein (α-Syn) aggregation within the SN and the degeneration of nigrostriatal dopamine neurons, changes in mean diffusivity and fractional anisotropy indicating microstructural degeneration in the nigrostriatal pathways, altered FC patterns particularly in the dopaminergic and cognitive networks, and distinct metabolic network involvement in CTC pathways primarily mediating PD tremor (Kim et al., 2017; Mure et al., 2011; Ryman and Poston, 2020).

2.2 Computational Modelling

Utilizing computational models in the study of neurological disorders, such as PD, presents several advantages over solely relying on empirical data, which often involves limited sample sizes due to practical constraints. Computational models offer increased accuracy, provide robust theoretical frameworks, and facilitate the integration of diverse methodologies and scales of brain behaviour analysis (Deco and Kringelbach, 2014; Teufel and Fletcher, 2016). These models are particularly advantageous in transforming our understanding and management of specific symptoms of PD, such as tremor, where employing computational models has led to the identification and description of underlying mechanisms while proposing innovative treatment approaches (Caligiore et al., 2016; Schiff, 2010; Yu et al., 2020). Specifically, dynamic and multi-scale computational models that are capable of integrating data from various sources, including brain imaging techniques, are adept at addressing the complex origin and mechanisms of PD tremor, which involve multiple brain regions and networks and remain poorly understood. This comprehensive approach allows for making causal inferences about the mechanisms of tremor, the consequent neural dynamics, and the efficacy of potential treatments, thus providing a more holistic understanding of the disorder (Caligiore et al., 2016; Humphries et al., 2018; Yu et al., 2020). For instance, mechanistic models by Caligiore et al. have clarified how dopaminergic neurodegeneration impacts basal ganglia function, establishing a direct link to tremor (Caligiore et al., 2019). In another study, systematic exploration of BTC connections and the relevant sub-circuits via modelling has contributed to revealing the dynamical malfunctions, such as synchronisation issues, that are crucial for understanding the tremor's neurobiological basis (Yu et al., 2020). A cornerstone of these advancements is the FDS theory, as described in section 1.2 , which has been thoroughly investigated and affirmed through dynamic causal modelling (Dirkx et al., 2017). In diagnostic methodologies, the application of machine learning for tremor classification and analysis, leveraging high-resolution accelerometric data, has significantly improved diagnostic accuracy and minimized bias in diagnoses (De et al., 2023). Translating these findings into clinical applications, computational models have enabled the investigation of complex treatment strategies such as deep brain stimulation (DBS) in alleviating PD tremor and have contributed to advancements in hardware design, optimization stimulation targets and parameters, and exploring alternative NIBS techniques (Little and Bestmann, 2015; Mcintyre and Foutz, 2013; Rahimi et al., 2023; Saenger et al., 2017). These examples showcase the broad applicability of computational methods in identifying tremor markers, potentially leading to earlier diagnosis and intervention.

2.3 Non-invasive Brain Stimulation

NIBS techniques, established in the mid-to-late 20th century, are recognized as effective tools for investigating and modulating neural activity (Barker et al., 1985; Woods et al., 2016). These methods enable targeted interventions with minimal side effects, positioning them as attractive options for therapeutic applications such as PD (Brittain and Cagnan, 2018; Fregni, 2005). Recent randomized controlled trials have shown promising outcomes in managing PD symptoms such as tremor using NIBS, yet they remain secondary to the established pharmacological or invasive treatments such as DBS (Erro et al., 2022; Madrid and Benninger, 2021). Transcranial alternating current stimulation (tACS) is a NIBS method designed specifically for exploring and modulating brain oscillations, rendering it a compelling approach for addressing an oscillatory phenomenon like tremor (Brittain and Cagnan, 2018; Ganguly et al., 2020). This technique involves administering a weak sinusoidal electric current to specified brain regions by placing two or more electrodes on the scalp (Herrmann et al., 2013; Tavakoli and Yun, 2017). The application of tACS influences the brain at both microscopic and macroscopic levels through various mechanisms of action. At the microscopic level, tACS affects ion channels and neurotransmission systems, impacting the fundamental biochemical pathways of neuronal communication. At the macroscopic level, tACS influences brain oscillations and FC, primarily through a phenomenon known as entrainment (Shirehjini et al., 2023). The periodic nature of tACS can entrain or synchronise the intrinsic brain oscillations at the targeted region, implying that the oscillatory activity within the brain begins to align with the periodicity of the external current. Essentially, the oscillator within the brain becomes entrained or locked to this external stimulus. In this scenario, the terms synchronisation, entrainment, and locking are used interchangeably to describe this phenomenon (Strogatz, 2003; Thut et al., 2011). Entrainment is most effective when the stimulation amplitude is strong enough and the frequency matches the endogenous oscillations (Helfrich et al., 2014; Shirehjini et al., 2023).

Among the brain regions implicated in PD symptoms, tACS is particularly suited for those that are relatively superficial and close to the scalp, allowing weak electrical currents to reach them effectively. Consequently, the motor cortex has been a preferred site for stimulation due to its accessibility and involvement in motor functions (Guerra et al., 2022; Krause et al., 2014). More recently, however, the cerebellum has been identified as a promising target for tACS, supported by a growing body of research (Manto et al., 2021; Miterko et al., 2019). Advanced tACS techniques fine-tune stimulation signals to effectively entrain and modulate neural oscillations within this region, enhancing the exploration of cerebellar functions across various neural networks in both healthy and diseased states (Antal and Herrmann, 2016; Fiene et al., 2020; Wessel et al., 2022). This approach has proven instrumental in studying mechanisms such as cerebellum-motor cortex inhibition (CBI) and motor adaptation (Manto et al., 2021; Naro et al., 2016; Wessel et al., 2022). The entrainment of neural oscillations through tACS also has clinical implications, particularly in the management of PD symptoms. It has been applied to entrain and suppress tremor in PD and essential tremor (ET), demonstrating significant therapeutic potential (Brittain et al., 2015; Schreglmann et al., 2021). These developments not only deepen our understanding of the complex functions of the cerebellum but also highlight the potential for targeted neurological interventions.

Chapter 3 : Thesis Hypothesis and Structural Outline

We have established the significance of the CTC network and its key nodes such as the cerebellum in the dynamics of PD tremor. Methodologically, MRI-based techniques allow for the identification of structural and functional changes within this network that could serve as potential biomarkers. Moreover, computational modelling approaches, particularly combined with MRI data, can provide insights into the underlying network dynamics of PD tremor. Finally, NIBS techniques such as tACS allow for entrainment and modulation of intrinsic oscillatory activity within networks such as the CTC and can lead to an in-depth understanding of the network and further to the development of innovative therapeutic strategies to manage this challenging motor symptom of PD.

There are currently no comprehensive multimodal approaches that combine MRI imaging, computational modelling, and stimulation to focus on the CTC network and cerebellum in PD tremor. This thesis aims to address this gap by investigating these areas through diverse modalities. Specifically, the research questions addressed in this thesis are threefold:

i. Are there structural alterations in the cerebellum, a critical region of the CTC, directly associated with PD tremor severity?
ii. Are there distortions in the dynamics of the whole brain and the CTC network due to PD which could potentially be associated with tremor, and how influential is the cerebellum in the whole-brain dynamics?
iii. How can the dynamics of the cerebellum be modulated by non-invasive stimulation? Particularly, what are the optimum experimental design and stimulation device required to achieve effective modulation?

To address the research questions outlined, a series of studies were designed and conducted. I took the lead in executing the majority of this work and was the primary author of all related publications. The subsequent chapters are each dedicated to a single research question and its corresponding study, with the exception of Chapter 6, which encompasses two related studies. Due to the distinct nature of each study, every chapter includes a brief introduction, methodology, results, and conclusions. All findings are then brought together in a conclusion chapter that consolidates and discusses the research outcomes.

Chapter 4 : Alterations of the Cerebellar Structure in PD Tremor

This chapter presents an in-depth exploration of the alterations observed in the structure of the cerebellum within the CTC network in individuals with PD, based upon the previously published paper, '**Smaller Cerebellar Lobule VIIb is Associated with Tremor Severity in Parkinson's Disease**' by Sadeghi et al. (2023). In this study, my contributions were as follows: Conceptualization and design, data collection and analysis, and manuscript writing.

4.1 Introduction

As discussed in the general introduction, the cerebellum's structure is implicated in PD tremor mainly due to its involvement in the CTC network. Notably, the cerebellum contains detailed somatotopic body maps (Boillat et al., 2020; Choi et al., 2012) and a complex topographical organization, enabling its various sub-regions to intricately connect with the cerebral cortex, thus supporting a spectrum of motor functions (Diedrichsen et al., 2019; Xue et al., 2021). The anterior and posterior lobes of the cerebellum are key to primary and secondary somatomotor functions, respectively (Buckner et al., 2011). Specifically, regions corresponding to hand movements are located in ipsilateral lobules III-VI, VIIb, and VIIIa, which interact closely with the primary motor cortex (M1) through a series of bidirectional projections within the CTC network (Buckner et al., 2011; Stoodley et al., 2012). Furthermore, in a recent study, we showed that these and their adjacent lobules are associated with more favourable hand-related recovery outcomes after a stroke (Sadeghihassanabadi et al., 2022a).

Although several studies have identified volume reductions in the cerebellar white and grey matter, correlating with PD severity and clinical symptoms (Benninger et al., 2009; Kovács et al., 2019; Lopez et al., 2020; Myers et al., 2017), there is inconsistency in terms of the cerebellum's anatomical and microstructural alterations associated with tremor severity (Gellersen et al., 2017; Wu and Hallett, 2013). Particularly, examining structural changes in cerebellar regions with disynaptic projections to the regions in the BTC network would be beneficial for understanding the pathoanatomy of PD tremor (Caligiore et al., 2017; Lopez et al., 2020; O'Callaghan et al., 2016).

Advances in technology have led to the development of fully automated MRI techniques that can accurately isolate and segment cerebellar lobules from standard T1-weighted images used in clinical settings (Abdelgabar et al., 2019; Carass et al., 2018; Manto et al., 2021). Regardless, MRI-based lobular morphology of the cerebellum in relation to distinct PD motor symptoms remains to be explored (Diedrichsen et al., 2019). Therefore, in this study, we aimed to identify the relationship between the volumes of cerebellar lobules and the severity of PD tremor (TR). Furthermore, associations with other PD motor symptoms including bradykinesia/rigidity (BR) and PIGD were investigated.

4.2 Methods

4.2.1 Participants

We retrospectively analysed data from 55 individuals (22 females) who have been diagnosed with PD and underwent MRI imaging at the University Medical Center Hamburg-Eppendorf from 2014 to 2017. The inclusion criteria for participants were: (1) age between 45 and 80 years, (2) a PD diagnosis conforming to the Parkinson's Disease UK Brain Bank criteria (Litvan et al., 2003) (3) no history of other neurological disorders (such as vascular malformations, ischemic or haemorrhagic stroke, cerebral neoplasia) or significant psychiatric illnesses, (4) availability of high-resolution T1-weighted images, and (5) provision of written informed consent. The study's procedure received approval from the local ethics committee of Hamburg and adhered to the Declaration of Helsinki standards.

For all PD patients, we collected demographic information including age, sex, disease duration, more affected body-side, and Hoehn and Yahr stage. Motor symptom severity was assessed using the MDS-UPDRS part III scale (Christopher G. Goetz et al., 2008) by PD nurses trained according to the Movement Disorder Society's protocols and under the guidance of movement disorder experts and experienced neurologists. The more affected body side of each patient was determined by comparing right and left side MDS-UPDRS part III scores. Patients were classified into two PD subtypes: TD and PIGD, based on their MDS-UPDRS motor scores and a method proposed by (Stebbins et al., 2013). This classification involves calculating the ratio of mean tremor scores to mean PIGD scores from specific MDS-UPDRS III items, with ratios ≤1 indicating PIGD subtype, >1 and ≤1.5 as indeterminate (excluded from analysis), and ≥1.5 indicating TD subtype. Furthermore, symptom-specific sub-scores were extracted for tremor (TR) from the sum of MDS-UPDRS items 2.10, 3.15 (postural tremor), 3.16 (kinetic tremor), 3.17, and 3.18 (rest tremor severity, constancy and frequency); BR from items 3.3, 3.4, 3.5, 3.6, 3.7, and 3.8; and PIGD from items 2.12, 2.13, 3.10, 3.11, and 3.12 (Poston et al., 2020). These sub-scores were individually included in the statistical analysis to investigate the associations between the corresponding motor symptoms and cerebellar volumes. All scores were calculated in OFF-medication status.

4.3 MRI Analysis

T1-weighted MRI images were acquired using a Siemens 3T Skyra scanner (Siemens Healthcare, Forchheim, Germany) equipped with a 32-channel head coil, employing magnetization-prepared rapid gradient echo (MPRAGE) sequences. The imaging parameters included an echo time (TE) of 2500 ms, a repetition time (TR) of 1.9 ms, a flip angle of 9°, a slice thickness of 1 mm, and a voxel resolution of 0.85. Imaging took place within a week following the MDS-UPDRS assessments. To minimize MRI artefacts from head motion, particularly in PD participants with tremor, a snug head coil and stabilizing cushions were used to secure the head.

The T1-weighted images were anonymized, defaced, visually inspected for quality, and adjusted for orientation using SPM12 (Penny et al., 2007). Volumetry analysis of the cerebellum was performed based on the automated CERES pipeline while controlling for individual age and sex variability (Carass et al., 2018; Romero et al., 2017). The process included segmentation, denoising (Manjón et al., 2010),

linear and non-linear registration to the MNI152 template (Avants et al., 2009), intensity normalization, and subject-specific extraction of 13 cerebellar lobules including lobules I, II, III, IV, V, VI, VIIb, VIIIa, VIIIb, IX, X, crus I and crus II in each cerebellar hemisphere as absolute values in cm3 (Giraud et al., 2016; Manjón et al., 2014; Park et al., 2014; Romero et al., 2017). An automatic inhomogeneity correction was performed before and after linear registration (Ashburner and Friston, 2005; Tustison et al., 2010). Additionally, total cerebellar volume and total intracranial volume (ICV) were extracted and further used to normalize the absolute values. All calculated volumes underwent visual verification to confirm the absence of outliers.

4.4 Statistical Analysis

In this study, we employed multiple linear regression models to examine the relationship between MDS-UPDRS part III, TR, BR, and PIGD scores as dependent variables and total cerebellar volume along with individual cerebellar lobule volumes as independent variables. Acknowledging the prevalence of age-related atrophy in both the cerebrum and cerebellum (Jernigan et al., 2001), we adjusted for ICV and age in our models, following a linear residualization method as per Rojas Albert et al. (Rojas Albert et al., 2022), and also considered sex as a covariate. To enhance data normality, TR, BR, and PIGD scores were logarithmically transformed (LOG_{10}). We applied a leave-one-out analysis (LOOA) to improve the robustness of our findings by identifying and excluding influential outliers. Multiple comparison corrections were performed using the false discovery rate (FDR) method (Benjamini and Hochberg, 1995) for 15 volumes of interest in the analyses of MDS-UPDRS part III, TR, BR, and PIGD scores. We further analysed distinct tremor types—postural, kinetic, and rest tremor—utilizing a predefined post-hoc multiple regression analysis to examine their association with cerebellar lobule volumes. Additionally, to isolate the impact of hand tremor and mitigate potential confounding influences from leg and jaw/lip tremors on our findings, we conducted a targeted post-hoc analysis on the upper extremities. This involved adjusting the overall tremor score by excluding the MDS-UPDRS scores related to leg and jaw/lip tremors. The adjusted scores were then analysed using the same multiple-regression framework to explore associations with cerebellar volume. All statistical analyses were conducted using R version 4.0.3 (r-project.org), and a corrected p-value of <0.05 was set as the threshold for statistical significance.

4.5 Results

4.5.1 Demographic and Clinical Results

Table 1 presents the demographic and clinical characteristics of PD patients. The median age of the group was 65 years, with an age range between 48 and 79 years (interquartile range, IQR). The duration of the disease varied, with a median of 11 years and an IQR of 1 to 25 years. Motor symptom severity in the cohort was generally mild to moderate, evidenced by a median motor symptom score of 33 (IQR of 14 to 65) and a median Hoehn and Yahr stage of 2, ranging from 1 to 4 (IQR).

Table 1. Demographic and clinical characteristics of PD patients

	Group size (%)	Mean (SD)	Median [Min, Max]
Sex	55		
Female	22 (40.0%)		
Male	33 (60.0%)		
Age		62.6 (7.60)	65.0 [48.0, 79.0]
Disease Duration		11.5 (4.14)	11.0 [1.00, 25.0]
PD Subtype			
PIGD	45 (81.8%)		
TD	10 (18.2%)		
MDS-UPDRS total (OFF)		62.6 (20.8)	58.5 [33.0, 121]
MDS-UPDRS III (OFF)		35.5 (13.3)	33.0 [14.0, 65.0]
BR Score		20.4 (8.2)	20.0 [5.00, 41.0]
TR Score		6.4 (6.9)	4.00 [0, 26.0]
PIGD Score		6.3 (4.1)	6.00 [0, 15.0]
Hoehn & Yahr (OFF)		2.4 (0.7)	2.00 [1.00, 4.00]

MDS-UPDRS: Movement Disorder Society-Sponsored Revision of the Unified Parkinson's Disease Rating Scale, **MDS-UPDRS III**: part III motor examination, **BR**: bradykinesia, **TR**: tremor, **PIGD**: postural instability and gait disorders, **SD**: standard deviation

4.5.2 Cerebellar Volumes vs. Symptom Severity

Our linear regression analyses identified a significant negative correlation between the volume of the cerebellar lobule VIIb and tremor severity score ($p = 0.004$, see Figure 3 and Table 2). No significant correlations were observed between tremor severity and the volumes of the total cerebellum or other individual lobules (Table 2). Additionally, disease duration was significantly associated with tremor severity score ($p = 0.006$), while age, sex, and ICV did not show a significant impact (Table 3). Further results related to individual cerebellar lobules are provided in Supplementary Table S1.

The analysis exploring associations between cerebellar structure and motor symptoms of bradykinesia and rigidity, as indicated by BR and PIGD scores, did not identify any significant relationships (all p-values > 0.13, refer to Supplementary Table S2 and Table S3). Further investigation into different types of tremor through post-hoc analysis highlighted that the severity of kinetic tremor was driving the significant association observed between tremor severity and volume of lobule VIIb, a finding which remained robust after both LOOA and FDR correction ($p = 0.002$). However, neither postural tremor ($p = 0.066$) nor rest tremor ($p = 1.000$) demonstrated a significant relationship with the volume of lobule VIIb (refer to Supplementary Table S4, Table S5, and Table S6). Additionally, a post-hoc regression analysis focusing specifically on hand tremor confirmed the primary result, revealing a significant correlation between the volume of lobule VIIb and hand tremor severity ($p = 0.005$, see Supplementary Table S7).

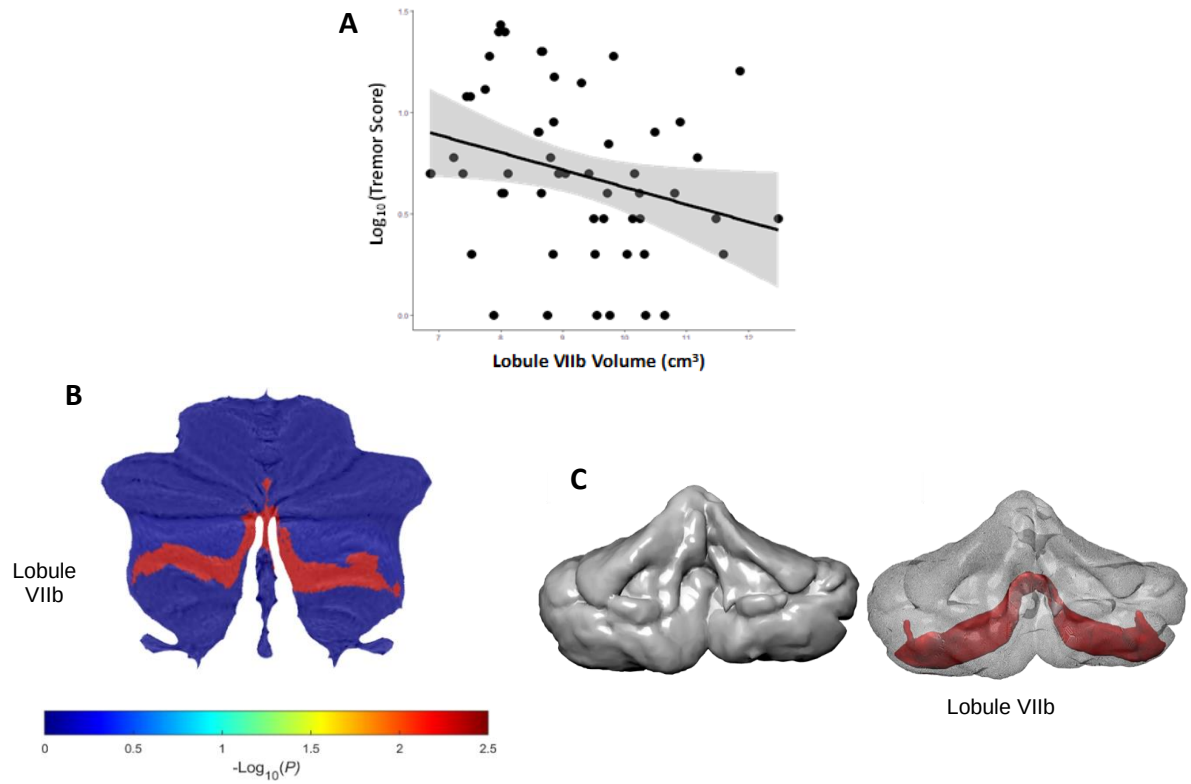

Figure 3. Association between volume of cerebellar lobule VIIb and tremor severity score in PD through linear regression analysis. A) The plot features a logarithmic scale on the y-axis, with individual lobule VIIb volumes and total tremor scores represented as scatter points. The grey area around the regression line indicates the 95% confidence interval. **B)** cerebellar flatmap, with the colour scale representing p-values (expressed as -Log10(*P*) for clearer visualization) that correspond to the beta coefficients of lobule volume with total PD tremor score. **C)** a 3D reconstruction of the cerebellum, with bilateral lobule VIIb specifically highlighted.

Table 2. Association between cerebellar volumes and tremor scores in PD patients

Cerebellar regions	Beta coefficient (95% CI)	p-values
Cerebellum	-0.01	0.166
Lobule I-II	-2.70	0.031
Lobule III	-0.38	0.063
Lobule IV	0.06	0.510
Lobule V	-0.03	0.546
Lobule VI	<0.00	0.835
Crus I	0.01	0.690
Crus II	-0.04	0.094
Lobule VIIb	-0.13	0.004*
Lobule VIIIa	-0.05	0.152
Lobule VIIIb	-0.03	0.385
Lobule IX	-0.05	0.284
Lobule X	-0.15	0.502

*p-values that are significant after LOOA analysis as well as FDR correction. Results of multiple linear regression models are presented and the primary outcome is demonstrated via beta coefficient. The confidence interval is considered as 95%. Cerebellar lobules exhibiting a significant association with tremor severity score are highlighted in bold. Results are adjusted for age, sex, disease duration, and ICV. **LOOA**: leave-one-out analysis; **FDR**: false discovery rate; **ICV**: intracranial volume

Table 3. Co-factors in the relationship of lobule VIIb volume and tremor severity

Model variables	Beta coefficient (95% CI)	p-values	95% CI	
			lower	upper
Volume of VIIb (cm^3)	-0.13	0.024*	-0.21	-0.04
Age (years)	-0.01	0.339	-0.02	0.01
Sex (M/F)	0.05	0.289	-0.20	0.30
Disease Duration (years)	-0.03	0.006*	-0.06	-0.01
ICV (cm^3)	<0.01	0.386	0.00	0.00

*p-values that are significant after LOOA analysis as well as FDR correction. The results are controlled for age, sex, disease duration, and ICV as covariables. Significant factors are highlighted in bold. The primary outcome is reported as a beta coefficient and the confidence interval is considered as 95%. **LOOA**: leave-one-out analysis; **FDR**: false discovery rate; **ICV**: intracranial volume

4.6 Discussion

This study reveals significant correlations between the volume of cerebellar lobule VIIb and tremor severity in PD, highlighting the structural implications of the cerebellum in the pathophysiology of tremor. Previous research suggests that structural alterations within the cerebellum are linked to reduced resting-state FC between the cerebellum and the sensorimotor network and are therefore associated with the severity of PD tremor (O'Callaghan et al., 2016). In general, the cerebellum's involvement in PD tremor is best understood through a network perspective, particularly through the FDS framework as discussed in the general introduction. The cerebellum further interacts directly with SN and other regions within the basal ganglia in PD through disynaptic projections, highlighting its integrated role in motor functions (Manto et al., 2021; Washburn et al., 2024). Specifically, cerebellar lobule VII has topographically organized connections not only to the M1 but also to the sensorimotor portion of the STN, a key site for pathological tremor oscillations (Bostan and Strick, 2010; Caligiore et al., 2017). These connections facilitate the STN's influence on cerebellar activity, thereby completing a feedback loop crucial for tremor dynamics (Bostan and Strick, 2010). The specific involvement of cerebellar lobule VIIb in PD tremor, reflected by the FDS model, has been identified through grey matter atrophy among tremor-dominant PD patients (Piccinin et al., 2017). Nonetheless, refining the complex relationship between cerebellar atrophy and tremor severity in PD proves challenging due to inconsistent findings across various cerebellar regions. Studies often report various levels of atrophy in lobules IV, V, VI, VIIIa, VIIIb, Crus I, and the vermis, which highlights the cerebellum's intricate and diverse role in manifesting tremor in PD (Benninger et al., 2009; Gellersen et al., 2017; Li et al., 2020; Lopez et al., 2020; Van Den Berg and Helmich, 2021).

Our study describes a novel structural-clinical correlation in the cerebellum in PD tremor, specifically linking structural changes in individual cerebellar lobules to the severity of kinetic tremor. Such distinct delineation between the types of tremor, especially focusing on kinetic tremor and its cerebellar associations is relatively underexplored in the literature (Van Den Berg and Helmich, 2021). Our findings are distinct from previous associations, which primarily connected rest tremor severity with morphological alternations in cerebellar lobules such as IV and VIIIa but did not report significant results for kinetic or postural tremor types (Benninger et al., 2009; Lopez et al., 2020). However, in other types of tremor such as in ET, significant associations between kinetic tremor and the volume of cerebellar lobule VIIb, among others, have been documented (Broersma et al., 2016; Dyke et al., 2017). The

inconsistency in findings may stem from the diverse pathophysiological mechanisms underlying different tremor manifestations (Dirkx et al., 2019; Helmich et al., 2013).

This study identifies a volumetric relationship that is specific to tremor severity and does not extend to rigidity or bradykinesia. Furthermore, this association is limited to hand tremor, with no significant findings for tremor manifestations in the legs, jaw, or lips. These observations are consistent with recent research that has highlighted a cerebellar correlation exclusively with MDS-UPDRS tremor scores for the upper limbs (Bohnen et al., 2021; Lopez et al., 2020). In this study, age was not a contributing factor to the primary outcome, while a longer duration of the disease was significantly linked to decreased tremor severity. Although both age and disease duration might influence the clinical manifestations of PD (Cilia et al., 2015), the high variability in disease duration and the small effect size pose challenges to the interpretation of these results (Marras and Lang, 2013).

The limited sample size of this study restricts the generalizability of the findings. To address this limitation and enhance the robustness of our statistical analysis, LOOA was employed, prioritizing specificity over sensitivity. The study did not explore structural variations between subtypes of PD (TD vs. PIGD) due to the inadequate number of participants within each subtype to form comparably sized groups, and performing regression models with insufficient sample sizes would lead to reduced statistical power (Button et al., 2013).

Our findings suggest that a reduced volume of lobule VIIb could be considered a potential biomarker for tremor severity in PD, echoing the relative criteria in the field (Miller and O'Callaghan, 2015) and further contribute to enhancing the cerebellar morphological mapping of tremor-associated regions and networks. The identification of this structural characteristic holds promise for prognostic assessment and therapeutic interventions. Future research is encouraged to include larger cohorts of PD participants, categorized into age- and sex-matched groups according to PD subtypes. Additionally, incorporating longitudinal studies with both MDS-UPDRS assessment and imaging data could offer greater insights into how age and disease progression influence volumetric changes in PD over time. Particularly relying on higher-resolution MRI technology (>3T) alongside specialized sequences such as quantitative susceptibility mapping (QSM) can reveal detailed structures within the cerebellum that are relevant in tremor pathophysiology, including the dentate nucleus (He et al., 2017).

Chapter 5 : Distortions of the Whole Brain and CTC Equilibrium in PD

This chapter explores the broader neurological implications of PD and presents findings from a collaborative study between the University Medical Center Hamburg-Eppendorf, Germany and Pompeu Fabra University, Spain. The focus of this research is on disturbances within the brain's equilibrium, specifically targeting the CTC network. The corresponding paper, titled "**The Arrow of Time in Parkinson's Disease**" by Sadeghi et al. (2024) is currently under review. My contribution to this project included the conceptualization and design, data collection and analysis, interpretation, and manuscript writing.

5.1 Introduction

The healthy brain relies on time-sensitive computations to ensure survival and efficient processing of information. These computations are orchestrated within a dynamic, spatiotemporal hierarchy (Carr, 1993). The flow of information and energy are organized within this complex system in ways that adhere to physical laws, especially those of thermodynamics. The notion of the 'arrow of time', introduced by Nobel Laureate Sir Arthur Eddington, describes the directional progression of events within a system, which is closely linked to the flow of information and energy (Murphy and Eddington, 1928). In a perfectly balanced system with complete equilibrium, information ceases to flow, resulting in events unfolding symmetrically with no definable start or finish. However, any disturbance to this equilibrium leads to a directional information flow, signifying a deviation from temporal symmetry or reversibility. This principle is instrumental in examining causality within complex systems. The presence of a directed information flow suggests an underlying causal link offering insights into the interconnected dynamics of system components (Liang, 2018; Pearl, 2009; Runge, 2015).

The healthy human brain inherently functions as a non-equilibrium system, driven by energy-consuming and non-reversible molecular and cellular activities, including neuronal firing and information processing, which are essential for survival and maintaining consciousness (Lynn et al., 2021; Sanz Perl et al., 2021; Tomé and De Oliveira, 2012). In disease state, deviations from this non-equilibrium baseline may occur, stemming from pathological changes in structure and function or through compensatory mechanisms (Cruzat et al., 2023; Deco et al., 2021). Expanding on the innovative approaches by Seif et al. (2021), who introduced a machine learning method to analyse temporal asymmetries and understand causal dynamics in non-equilibrium systems, Deco et al. (2022) developed a method to measure non-reversibility in the brain. This method uses temporal variations in fMRI BOLD signals to assess information flow dynamics.

To maintain equilibrium and ensure energy-efficient information flow, brain regions must operate and interact within specific hierarchical organizations (Buzsáki, 2009). These spatiotemporal patterns include directional influences, with the influencing region considered higher in the hierarchy than the influenced region (Shettigar et al., 2022). A non-equilibrium system inherently operates within a layered hierarchical organization (Kringelbach et al., 2023); therefore, identifying the directional arrow of time can enable the computation of hierarchical indices or relative 'heights' of brain regions. Methods such

as those by Mackay et al. (2020) facilitate this quantification. Numerous studies have utilized the characteristic hierarchical organization of various brain states to explore underlying mechanisms and distinguish between conditions such as cognitive tasks, levels of consciousness, and neurological disorders (Bolton et al., 2023; Cruzat et al., 2023; de la Fuente et al., 2023; G-guzmán et al., 2023; Kringelbach et al., 2023; Sanz Perl et al., 2021; Zanin et al., 2020).

The extensive implications caused by PD neuropathology in the brain have been discussed in the general introduction. Among those, the functionality and synchronisation impairment within the BTC and the CTC networks are of relevance for investigations of brain balance (Dirkx and Bologna, 2022; Helmich, 2018). Even though various structural and functional impairments of PD are well-documented (Delaveau et al., 2010; Filippi et al., 2019; Kim et al., 2017; Tahmasian et al., 2015; van Eimeren et al., 2009; Wolters et al., 2019), there remains a gap in our understanding of whether these impairments affect the overall balance of the brain and disrupt its hierarchical organization. The arrow of time approach, as described above, is capable of leveraging conventional fMRI data to detect dynamical abnormalities i.e. temporal asymmetries by computing pairwise correlations between forward and artificially reversed BOLD timeseries. For this study, we hypothesized that PD would be associated with dynamical alterations across the brain, namely altered reversibility and equilibrium levels at the global, network, and local scales during the resting state. We sought to test the informative quality of the arrow of time approach in revealing underlying PD pathology by performing pattern separation of reversibility profiles between the healthy and disease cohorts. Additionally, we explored alterations in the hierarchical organization of the brain due to this neurodegenerative disease.

5.2 Methods

5.2.1 Participants

30 individuals diagnosed with PD (mean age 60 years, SD = 10.80) were recruited from the outpatient clinic of the Department of Neurology of the University Medical Center Hamburg-Eppendorf, as well as 20 healthy age- and gender-matched participants (mean age 64 years, SD = 9.02). The inclusion criteria were as follows: (1) being within the age range of 40 to 85 years; (2) for patients: a confirmed diagnosis of PD based on the UK Brain Bank criteria (Litvan et al., 2003); (3) absence of any history of head trauma, concurrent neurological disorders, psychiatric conditions, or substance misuse; (4) non-pregnant state ;(5) adherence to MRI safety standards; (6) ability to provide informed consent.

All participants underwent identical MRI scanning protocols. One patient and one healthy individual were excluded from the study due to the inability to finish the scanning session and insufficient quality of MRI images respectively. The patients underwent a clinical neurological examination by a board-certified neurologist with specialty training in movement disorders who was blinded to the MRI data. Symptom severity was assessed using the MDS-UPDRS parts II and III (Christopher G. Goetz et al., 2008) and Hoehn and Yahr stages (Hoehn and Yahr, 1967). All participants provided written consent, and experiments were conducted according to the Declaration of Helsinki and local ethical regulations, with precedent approval from the local ethics committee of Hamburg. One Parkinson's disease patient was excluded due to a hand tremor during the MRI session, which caused significant movement artefacts that could not be corrected. Additionally, one healthy control was excluded because a complete MRI

session could not be recorded, and the necessary diffusion-weighted imaging (DWI) for model construction was not obtained Demographic information and clinical assessment results are summarized in Table 4.

Table 4. Demographical and clinical characteristics of PD patients and healthy controls.

	PD patients n = 29	Healthy controls n = 19	p-values
Age	63.76 (9.02)	59.68 (10.80)	0.16
Sex (number of females)	13	10	0.60
Disease Duration [a]	3.69 (2.75)		
MDS-UPDRS II	7.72 (5.55)		
MDS-UPDRS III	31.03 (9.18)		
Hoehn and Yahr			
Stage I	3		
Stage II	22		
Stage III	1		
Stage IV	0		
PD Subtype			
TD	20		
PIGD	9		

[a]Disease duration is from the time of official diagnosis. Values are presented as mean, with SD in parentheses, unless otherwise specified. Demographic homogeneity regarding age and sex was assessed between cohorts by using a 2-tailed and 2-sample t-test and the Kruskal–Wallis test respectively. **SD:** standard deviation; **MDS-UPDRS III:** Movement Disorder Society-Sponsored Revision of the Unified Parkinson's Disease Rating Scale, part III; **TD:** tremor-dominant; **PIGD:** postural instability and gait disorders

5.2.2 MRI Acquisition

T1-weighted MRI images were acquired via an MPRAGE sequence on a 3T scanner (Siemens MAGNETOM Prisma, Erlangen, Germany) with a standard 64-channel head coil, 256 coronal slices with a field of view (FOV) = 230 mm, TE = 2.15 ms, TR = 2500 ms, flip angle = 8°, voxel size = $0.8 \times 0.8 \times 0.8$ mm, matrix dimension = 232 x 288 x 256, scanning time = 5':49'', and bandwidth = 240 Hz/pixel. For resting-state fMRI (rs-fMRI) images, we used a gradient echo planar imaging (EPI) sensitive to BOLD contrast, 200 slices with FOV = 216 mm, TR = 2220 ms, TE = 30 ms, flip angle = 80°, voxel size = 3 x 3 x 3 mm, matrix dimension = 504 x 504 x 200, distance factor 20%, scanning time = 7':32'', and bandwidth = 2170 Hz/pixel. Diffusion-weighted imaging (DWI) was performed using FOV = 218 mm, TR = 6800 ms, TE = 76 ms, voxel size = 1.8 x 1.8 x 1.8 mm, matrix size = 122 x 122 x 480, and bandwidth of 1640 Hz/pixel. The data were recorded with 96 optimal nonlinear diffusion gradient directions at b = 0 and b = 2000 s/mm2.

5.2.3 MRI Processing

The MRI processing was primarily conducted using the Connectome Mapper 3 (v3.1.0) pipeline (Tourbier et al., 2022). Anatomical T1-w images were first processed with Freesurfer (v7.1.1) for contrast normalization, tissue segmentation, and cortical surface reconstruction (Desikan et al., 2006). The processed images were parcellated into 1058 regions of interest (ROI) based on the Lausanne2018 atlas, encompassing 998 cortical and 60 subcortical regions (Cammoun et al., 2012; Tourbier et al.,

2022). The cerebellum was isolated and processed in parallel using the Cerebellums Segmentation (CERES) pipeline (Carass et al., 2018; Romero et al., 2017). It was segmented into thirteen distinct lobules and then integrated into the Lausanne2018 parcellation. This integration culminated in a whole-brain parcellation consisting of 1084 ROIs, referred to as the LC parcellation.

To facilitate investigations on the local and network levels, the 1084 parcellations were categorized into larger brain regions such as cortical lobes, thalamus, basal ganglia, brainstem, and cerebellum, following the Desikan-Killiany ROI mapping (Alexander et al., 2019). For network analysis, specific regions belonging to the BTC and CTC networks were identified and extracted based on the classification by Caligiore and Lewis respectively (Caligiore et al., 2016; Lewis et al., 2013). The BTC network comprised 167 ROIs within the basal ganglia (striatum, globus pallidus internus and externus, and subthalamic nucleus), the thalamus (the anterior ventral lateral nucleus), and the motor cortex (the primary and supplementary motor areas). The CTC network was characterized by 255 ROIs, including the cerebellum, the thalamus (the posterior ventral lateral nucleus), and the motor cortex (the premotor and somatosensory areas). Given that the resulting parcellation is anatomical and lacks certain functional mappings required for the analysis, automated anatomical labelling (AAL) parcellations were concurrently generated for every participant using the Connectome Mapper 3 pipeline. To integrate these two sets of parcellations for each individual, a custom-made algorithm was developed in MATLAB that used optimum probability mapping techniques for a precise bridging (The MathWorks, Inc., 2022). Details are provided in the Supplementary Materials and Supplementary Table S8.

The DWI image processing involved denoising via Mrtrix3 (Tournier et al., 2019), followed by bias field correction using FSL FAST. Corrections for motion artefacts and eddy currents were conducted using FSL MCFLIRT and Eddy, respectively (www.fMRIb.ox.ac.uk/fsl, FMRIB, Oxford). The pre-processed images were resampled to 1 x 1 x 1 mm voxels. DWI images were then registered to T1-w images using the ANTS toolbox (Avants et al., 2009). Reconstruction and tractography were conducted using the Mrtrix3 probabilistic modelling approach. As a result, individualized structural connectivity (SC) matrices were generated.

The pre-processing of fMRI images included discarding the initial five volumes, adjustment for slice timing and linear head motion using FSL, followed by removal of linear trends using the scipy library in Python (Van Rossum and Drake, 1995; Virtanen et al., 2020). Subsequently, motion-, cerebrospinal fluid (CSF), and white matter-induced nuisance signals were regressed out using the general linear model technique. Rs-fMRI images were then aligned to T1-w images using FSL. For each participant, ROI-averaged BOLD time series were extracted for the whole brain LC parcellation. Both DWI and fMRI analyses were conducted in native space.

5.2.4 Empirical Framework of Non-reversibility/Non-equilibrium

Quantifying entropy production directly in a high-dimensional context, such as our fine parcellation with over a thousand ROIs, presents significant challenges. To reach this goal while keeping the computational load at a feasible level, we adopted the INSIDEOUT framework, a thermodynamic-driven approach introduced by Jarzynski (Seif et al., 2021). As illustrated in Figure 4A-B, this is a technique to quantify empirical deviations from reversibility, referred to as non-reversibility, through pairwise

correlations of temporally-shifted series (Deco et al., 2022). Extracted time series from regions $x(t)$ and $y(t)$ are artificially reversed, resulting in $x^{(r)}(t)$ and $y^{(r)}(t)$, enabling a correlational analysis between forward and backward time series as depicted in [1] and [2] respectively.

$$c_{forward}(\Delta t) = < x(t)\ ,\ y(t + \Delta t) > \quad [1]$$

$$c_{reversed}(\Delta t) = < x^{(r)}(t)\ ,\ y^{(r)}(t + \Delta t) > \quad [2]$$

The c represents Pearson's correlation coefficient and Δt denotes the induced time shift. The absolute difference of the above correlations reveals the level of pairwise asymmetry or non-reversibility for the given time shift $\Delta t = T$ between nodes x and y, referred to as $I_{x,y}$, as per the following formula:

$$I_{x,y}(T) = |c_{forward}(T) - c_{reversed}(T)| \quad [3]$$

The level of non-reversibility/non-equilibrium can be generalized by extending the pairwise computations to all regions. Here, $x_i(t)$ represents the forward version of a multidimensional time series describing the system's dynamics, where i represents different dimensions. Similarly, $x_j(t)$ denotes the corresponding reversed backward time series. The forward and reversed time-shifted correlations can thus be expressed as functional causal dependency matrices or FS, as described in [4] and [5].

$$FS_{\text{forward},ij}(\Delta t) = -\frac{1}{2} log\ (1 - < x_i(t)\ , x_j(t + \Delta t)\ >^2) \quad [4]$$

$$FS_{\text{reversed},ij}(\Delta t) = -\frac{1}{2} log\ (1 - < x_i^{(r)}(t)\ , x_j^{(r)}(t + \Delta t)\ >^2) \quad [5]$$

For the given time shift $\Delta t = T$, the global measure of non-reversibility, or I, can be computed by the quadratic distance between the forward and reversed time-shifted matrices, as given by [6].

$$I = \left\| FS_{forward}(T) - FS_{reversed}(T) \right\|_2 \quad [6]$$

In our investigation, we selected a time shift of T = 1 s, determined by the autocorrelation function of the BOLD signals with our TR = 2.2 s ensuring a sufficiently decaying autocorrelation. For empirical non-reversibility computation, the extracted BOLD signals from the 1084 ROI parcellation were used after band-pass filtration between 0.008 and 0.08 Hz. Twenty-two hippocampal regions and eleven gyral subregions were excluded uniformly across participants due to insufficient quality of time series signals. Non-reversibility or non-equilibrium levels were computed for each participant across the remaining 1051 nodes. To estimate the global non-reversibility levels, the whole-brain values were averaged across all regions. For the node-level analysis, the value pertaining to each ROI within the 1051×1051 non-reversibility matrices was averaged within each cohort. On the network level, the focus was directed towards the regions within the BTC and CTC networks, with their corresponding data extracted as described in the MRI processing sections.

To compare the distribution broadness of empirical non-reversibility between PD and healthy cohorts on a node level, we employed the Brown-Forsythe test of variance, known for its robustness against deviations from normality assumptions (Brown and Forsythe, 1974).

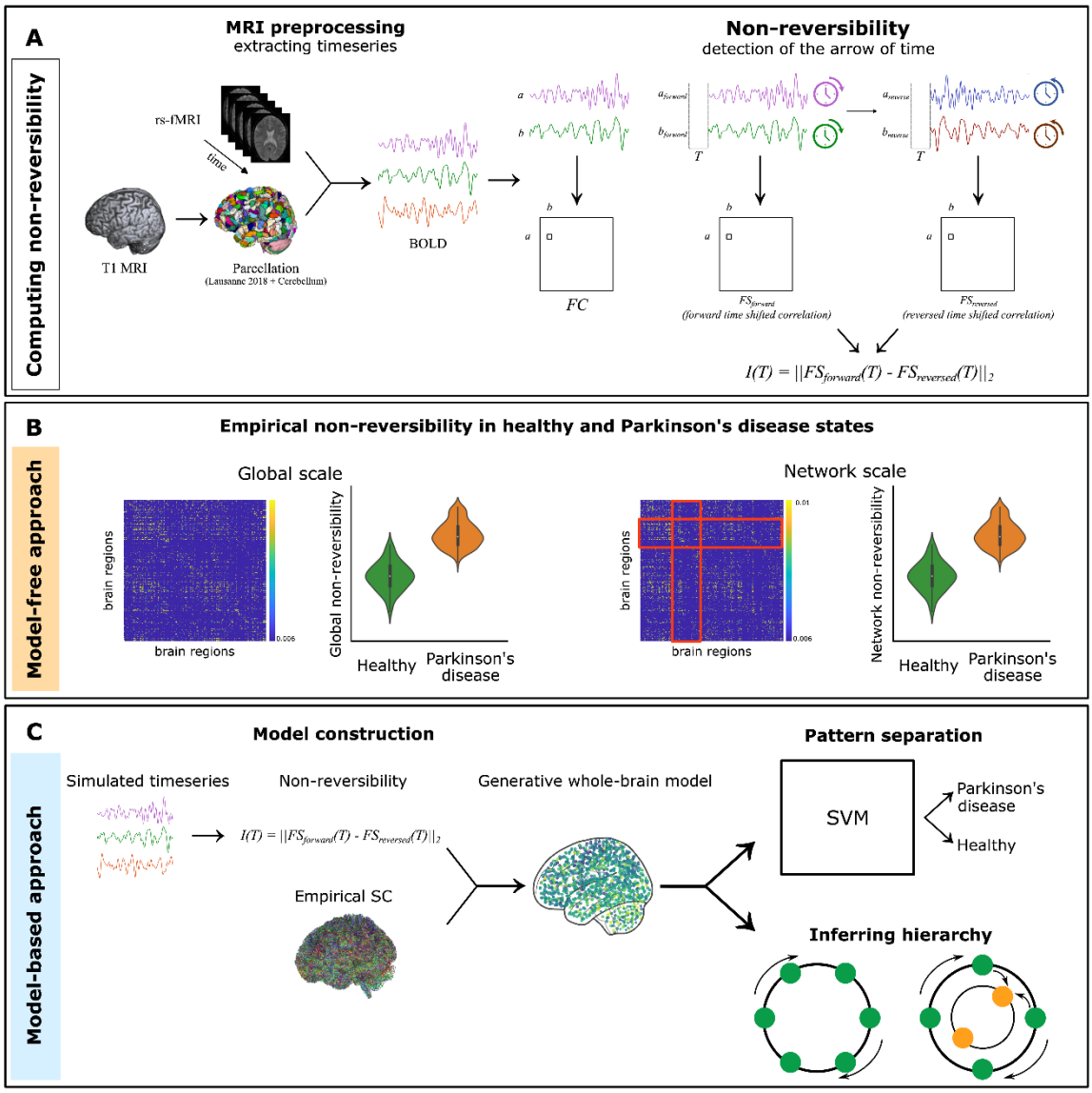

Figure 4. An overview of the methodological workflow to capture the arrow of time in PD. A) A step-by-step depiction of how non-reversibility (non-equilibrium) of the information flow is computed in the PD and healthy brain. The anatomical T1-w images are segmented and parcellated into a thousand regions of interest (ROI) in cortical, subcortical, and cerebellar regions. Resting-state fMRI (rs-fMRI) data are processed and BOLD signals are extracted from each ROI. Non-reversibility levels are computed by computing pair-wise correlations between time-shifted forward and artificially reversed time series. **B)** The model-free INSIDEOUT approach allows for quantification of non-reversibility measurement based on empirical data on multiple spatial scales. **C)** The model-based approach includes the construction of whole-brain computational models of generative effective connectivity (GEC), which are informed by empirical non-reversibility levels. The models can be used to perform pattern separation between PD and health and also to provide insight into hierarchical organization alterations between the two states.

5.2.5 Model-based Framework of Non-reversibility

5.2.5.1 The Hopf Model

We constructed whole-brain generative effective connectivity (GEC) models according to the methodology described by Kringelbach et al. (2023). According to this framework, the brain is represented as a network of coupled Hopf oscillators, with each node's local dynamics governed by the linearized form of a nonlinear supercritical Hopf bifurcation. The main computational elements are presented below, with the full description provided in the Supplementary Materials.

In the GEC model, the dynamics of node n are described as [7].

$$\frac{dz_j}{dt} = z_j\left(a_j + i\omega_j - \left|z_j^2\right|\right) + \sum_{k=1}^{N} C_{jk}\left(z_k - z_j\right) + \eta_j \quad [7]$$

Where

$$z_j = \rho_j e^{i\theta_j} = x_j + iy_j \quad [8]$$

The state variable z_j for the j-th oscillator is represented as a complex number with components x_j and y_j corresponding to the real and imaginary parts, respectively. The natural frequency of the oscillator is denoted by ω_j, and C_{jk} is the element of the coupling matrix that indicates the connection strength between the j-th and k-th oscillators. The system also includes additive Gaussian noise η_j (SD = 0.02). The system undergoes a bifurcation when $a_j = 0$. For $a_j < 0$, a stable fixed point is observed at $z_j = 0$; and for $a_j > 0$ the system's dynamics exhibit limit cycle oscillations at a frequency of $\frac{\omega_j}{2\pi}$ Hz. A fixed value of $a_j = -0.02$ was used, and the intrinsic frequency of each node, ω_j, was derived from the average peak frequency of the empirical time series pertaining to that node.

Given the large-sized 1051-region parcellations, training individual nonlinear Hopf models for each subject proved computationally impractical. As an alternative, we adopted a linear approximation method, which assumes minor nonlinearities and negligible noise, to estimate system statistics efficiently (Deco et al., 2023). As described in the Supplementary Materials, this method streamlines the computation process by directly deriving the system's statistics, thus eliminating the need for stimulating BOLD time series. Using FC which is based on the Pearson correlation matrix of time series, the activity between pairs of brain regions, and the time-lagged covariance matrix $CS_v(T)$ for a given time shift $\Delta t = T$, we performed local optimization of C for each node, as given in [9].

$$C_{i,j} = C_{i,j} + \epsilon\left(FC_{i,j}^{empirical} - FC_{i,j}^{model}\right) + \epsilon'\left(CS_v(\mathrm{T})_{i,j}^{empirical} - CS_v(\mathrm{T})_{i,j}^{model}\right) \quad [9]$$

Where ϵ = 0.0004 and ϵ'= 0.0001. To expedite the training process, a mean C is first trained from each group's averaged empirical FC and $CS_v(T)$, followed by initializing individual C values with the relative group averages and further optimizing until convergence. The results yield models informed by non-reversibility measures, otherwise known as directed GEC graphs. To account for the unique anatomical

features of each brain in the analysis, the optimization procedure was specifically tailored to nodes that exhibited a connecting fibre density above zero, as indicated by the associated SC matrix. The SC matrix has been normalized by dividing each of its elements by the matrix's maximum value. This normalization adjusts the SC matrix values to fall within a range of 0 to 0.2, effectively calibrating the influence of each connection to better reflect the dynamics of the brain network.

To compare the GEC patterns between PD and healthy states while addressing the issue of multiple comparisons, a linear kernel support vector machine (SVM) was trained to distinguish effective connectivity patterns between the two cohorts. The robustness of the model was ensured through cross-validation, maintaining an 85% to 15% training-to-test split over 1000 iterations. To confirm the reliability of SVM outcomes, the pattern separation technique was also applied to SC and FC. The network analyses focused on the BTC and CTC regions. As a control measure for the network analysis, the same trained SVM was applied to models with regions outside of these specific networks. A concise visual summary of the model-based approach is illustrated in Figure 4C.

5.2.6 Inferring the Brain's Hierarchical Organization

Whole-brain GEC measures provide insights into the hierarchical organization of the brain. Adopting the approach described by Mackay and colleagues (Mackay et al., 2020), a trophic hierarchy level can be computed for every node in the directed GEC network. This mathematical method relies on the asymmetry of in- and out-flows from each node, also reflecting the network's functional properties such as coherence.

In our whole-brain model, which consists of a set N of nodes and a set E of directed edges, each edge from the node m to node n is denoted as $m \to n$ and carries a positive weight represented by $\omega_{mn} > 0$, and all weights compiled into a matrix W. $\omega_{mn} = 0$ signifies the absence of an edge from m to n. This matrix is referred to as the adjacency matrix A when all edge weights are standardized to 1. We aggregate multiple edges between m and m by summing their weights, and self-edges $m \to m$ are allowed. The in-weight and out-weight (also known as in-strength and out-strength, respectively) for each node n are defined as follows.

$$\omega_n^{in} = \sum_{m \in N} \omega_{mn} \quad \text{and} \quad \omega_n^{out} = \sum_{m \in N} \omega_{nm} \qquad [10]$$

The total weight of the node n is defined by u_n as given by [11].

$$u_n = \sum_{m \in N} \omega_{mn} + \sum_{m \in N} \omega_{nm} \qquad [11]$$

For a given node, the imbalance between the in- and out-flow of the node is given by v_n**,** which indicates the difference between the in- and out-flow of the node n as below.

$$v_n = \omega_n^{in} - \omega_n^{out} \qquad [12]$$

The weighted graph-Laplacian operator Λ on vectors h is given in [13]

$(\Lambda h)_m = u_m h_m - \sum_{n \in N}(\omega_{mn} + \omega_{nm})h_n$ [13]

This can also be described in the matrix form as in [14].

$\Lambda = diag(u) - W - W^T$ [14]

The trophic level is defined as the solution of h by computed by solving the linear equation in [15].

$\Lambda h = v$ [15]

Moreover, the trophic incoherence denoting the directionality of the network can also be determined using the hierarchy level h, as per [16].

$F_0 = \frac{\sum_{mn} \omega_{mn} (h_n - h_m - 1)^2}{\sum_{mn} \omega_{mn}}$ [16]

Where coherence is defined as $1 - F_0$. A network is maximally coherent if F_0= 0 and incoherent if F_0= 1. Using the constructed GEC models, we computed trophic coherence and hierarchical levels for the 1051-region parcellation in PD and healthy states. Global measures were derived by averaging values across nodes. Subsequently, for node-level analysis, hierarchy index values were flattened into one dimension. Matrix flattening is a process used to transform a multi-dimensional array into a one-dimensional array. This simplification allows for easier data manipulation and analysis by converting the structured layering of data into a single, linear sequence. After flattening, we then employed linear mixed models to compare these measures between states, allowing us to account for individual variability across subjects. This method ensured a thorough examination of differences at both the global and node-specific levels. For the local scale, hierarchical levels were averaged within large regions, including cortical lobes, the thalamus, the basal ganglia, the brainstem, and the cerebellum. To further evaluate the influential role of the cerebellum in PD and healthy state, PageRank centrality measures were computed in the whole-brain directed GEC graph. The most central nodes (top 1%) were extracted and their roles in brain information flow were assessed by their corresponding trophic hierarchy levels.

After organizing the hierarchical levels locally, we evaluated the structure's flatness using a quadratic model and compared the curvature in both healthy and PD cohorts. We chose the quadratic model because it statistically outperformed a linear model, as indicated by an F-statistic of 14.842 and a p-value of 0.008. This significant difference led us to apply quadratic polynomial models to the average hierarchical levels across nine major brain regions for both the healthy control and PD groups, employing the *fitlm* function in MATLAB.

5.2.7 Statistical Analysis

To account for demographic differences, continuous variables like age were analysed using 2-tailed, 2-sample t-tests, involving 29 patients and 19 healthy individuals.

For categorical variables, such as sex, we utilized the Kruskal-Wallis test, maintaining consistent sample sizes across analyses. To compare global and network non-reversibility, as well as global trophic coherence and hierarchical levels between PD and healthy states, we employed Wilcoxon rank sum tests. This approach provides robustness against deviations from normal distribution and heterogeneous variances. Additionally, in the node-level analyses of non-reversibility and trophic hierarchy levels, we accounted for potential variability among subjects by using linear mixed models. These models treated cohort as the primary variable and included gender and age as covariates, with subject ID as a random effect to manage intra-subject correlations. All statistical analyses were performed in MATLAB, with significance based on an alpha level of 0.05. The resulting p-values were corrected for multiple comparisons via the FDR method (Benjamini and Hochberg, 1995).

5.3 Results

5.3.1 Empirical Non-reversibility/Non-equilibrium

At the global level, we analysed non-reversibility matrices of size 1051×1051, which, when averaged across nodes, demonstrated significantly higher levels in cases of PD (Figure 5A; $p = 0.006$). Furthermore, when examining the data at the node level across the entire brain, we found a marked increase in the average non-reversibility within the brains affected by the disease (Figure 5B; $p < 0.001$). The analysis extended to two pathologically affected PD tremor, namely BTC and CTC. Our findings revealed elevated non-reversibility levels in both networks due to PD (Figure 5C-D; BTC: $p = 0.007$; CTC: $p = 0.008$). To validate our results, we conducted the same analysis using FC matrices across all levels. While significantly higher FC values were observed in PD on the node level ($p < 0.001$), no significant differences were observed on the global ($p = 0.150$) or network level (BTC: $p = 0.396$; CTC: $p = 0.148$).

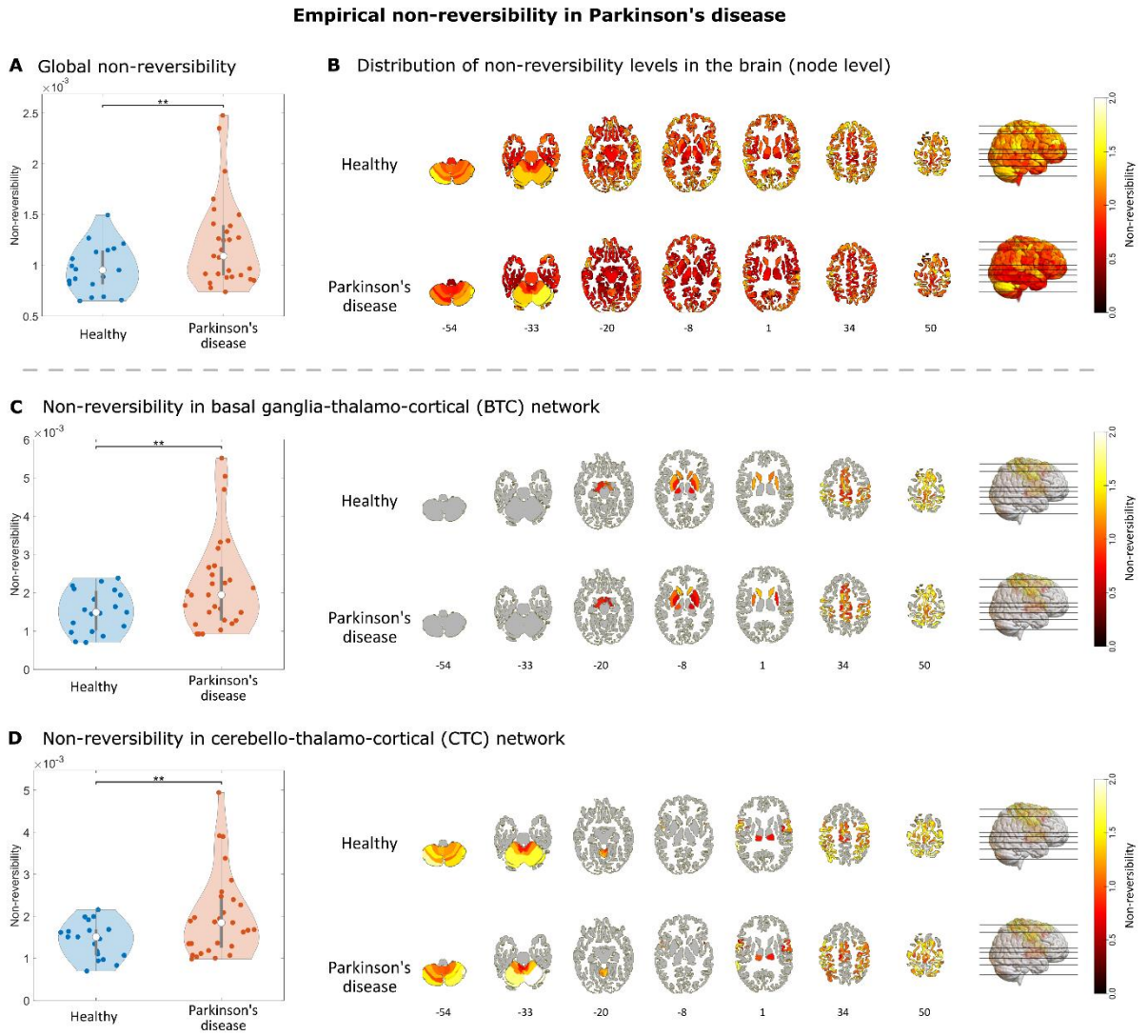

Figure 5. Empirical non-reversibility levels are higher in PD across multiple scales. A) The global non-reversibility levels averaged across 1051 parcellated regions, are significantly elevated in PD (p = 0.006), suggesting a deviation from equilibrium. **B)** At the node level, PD exhibits a significant increase in non-reversibility (p < 0.001), highlighting the localized impact of the disease. **C)** Distribution of non-reversibility levels across the brain, comparing the differences between healthy and diseased states by calculating the absolute difference $|NR_{PD} - NR_{Healthy}|$. This is depicted through seven axial brain slices, arranged in rows, alongside a 3D-rendered visualization of the brain on the right, providing a detailed spatial understanding of non-reversibility variations. **D-E)** Left: Focusing on the basal ganglia-thalamo-cortical (BTC) and cortico-thalamo-cortical (CTC) networks, increased non-reversibility values are observed in Parkinson's disease (p = 0.007, p = 0.008); right: visualization of the non-reversibility distribution and differences in both networks respectively. 3D mapping was carried out using MATLAB and MRIcroGL (Rorden and Brett, 2000).

5.3.2 Model-based Framework of Non-reversibility

5.3.2.1 GEC Patterns in PD and Healthy State

To assess the efficacy of the arrow of time methodology for distinguishing effective connectivity patterns between PD and healthy states, we employed an SVM to execute pattern separation between disease and healthy conditions. Notably, the whole brain GEC model yielded a 100% accuracy rate in separating the two states. To verify this precision, we used the same trained SVM on alternative measures including SC and FC matrices, which resulted in remarkably reduced accuracies of 52.3% and 63.5%,

respectively. To further test the SVM's robustness, we deliberately altered 25% of data labels for PD and healthy subjects, which resulted in a notable decrease in accuracy by 23.0%. At the network level, the SVM performed with high accuracies of 98.3% and 100% for the BTC and CTC network models, respectively. In a test of validity, the SVM was used with no-network models, which included all brain regions outside the BTC or CTC networks. The results revealed a precision drop to 78.4%. SVM performances across all scenarios are detailed in Figure 6.

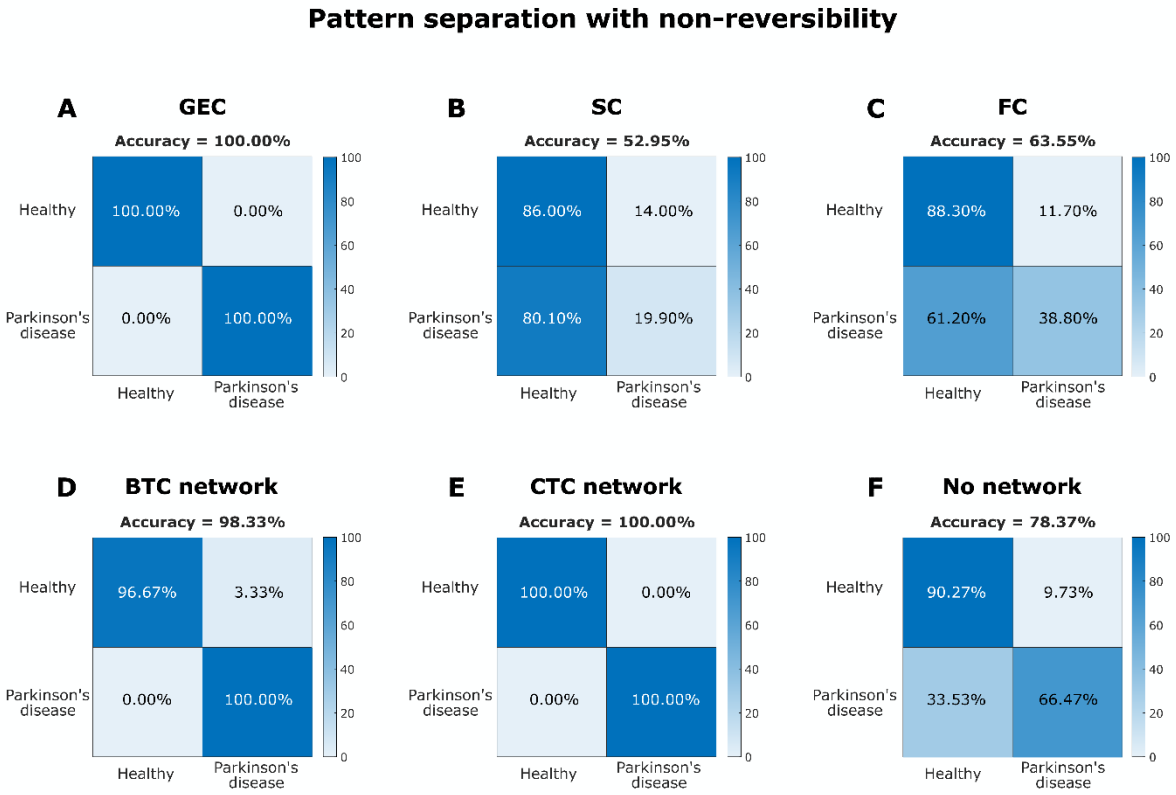

Figure 6. Generative effective connectivity (GEC) patterns are distinct in PD. A) SVM can separate whole-brain GEC patterns between Parkinson's disease (PD) and healthy states with 100% accuracy. **B-C)** Pattern separation using alternative measures of structural connectivity (SC) and functional connectivity (FC) results in a drop in precision, emphasizing the informative quality of non-reversibility measures. **D-E)** Pattern separation based on BTC and CTC network models achieved high accuracy rates of 98% and 100%, respectively. **F)** Testing a third no-network model resulted in an accuracy decline of 78%, suggesting that while BTC and CTC networks are not exclusive drivers of the results, they are relatively informative in investigating PD. The SVM was employed for pattern separation rather than classification, given the limited sample size, which precludes generalizable classification outcomes.

5.3.2.2 Hierarchical Organization in PD

Our investigation of trophic coherence and hierarchical organization in PD spanned multiple spatial scales. Globally, the coherence levels in PD showed a non-significant decline (Figure 7A; $p = 0.25$). At the node level, no significant differences were observed between the hierarchical indices of the two cohorts, determined by the linear mixed models (estimate = 0.002, standard error [SE] = 0.003, $t = 0.813$, $p = 0.415$).

The variability of hierarchical indices across the brain was further investigated by comparing fano factor distributions (Supplementary Figure S1). At the local scale, PD is associated with a reduction in hierarchical indices across all regions, although not statistically significant (Fig. 3c). The flatness

analysis of hierarchical organizations at the local level, using a quadratic model (y ~ 1 + x1 + x1^2), showed non-linear declines in hierarchical structure across regions for both groups. The PD group displayed a flatter hierarchy than the healthy group, indicated by less pronounced curvature. Specifically, the quadratic coefficients, which measure the change in slope of hierarchical levels, were higher in PD patients (0.001311) compared to healthy controls (0.000943). This suggests a more gradual decrease in hierarchical levels in PD, with both groups experiencing an initial levelling off followed by a gentler decline in PD due to their larger coefficients.

Furthermore, Pairwise comparisons revealed significant differences in hierarchical relationships, particularly with the cerebellum raking significantly higher in PD. Of note, the cerebellum also exhibited a relatively high PageRank centrality measure in the whole-brain directed GEC graph (Supplementary Figure S2), pointing to its elevated influence on the disease state. Moreover, the difference in hierarchical levels between the thalamus and cingulate cortex was significant in the PD state (p-values presented in Figure 7C).

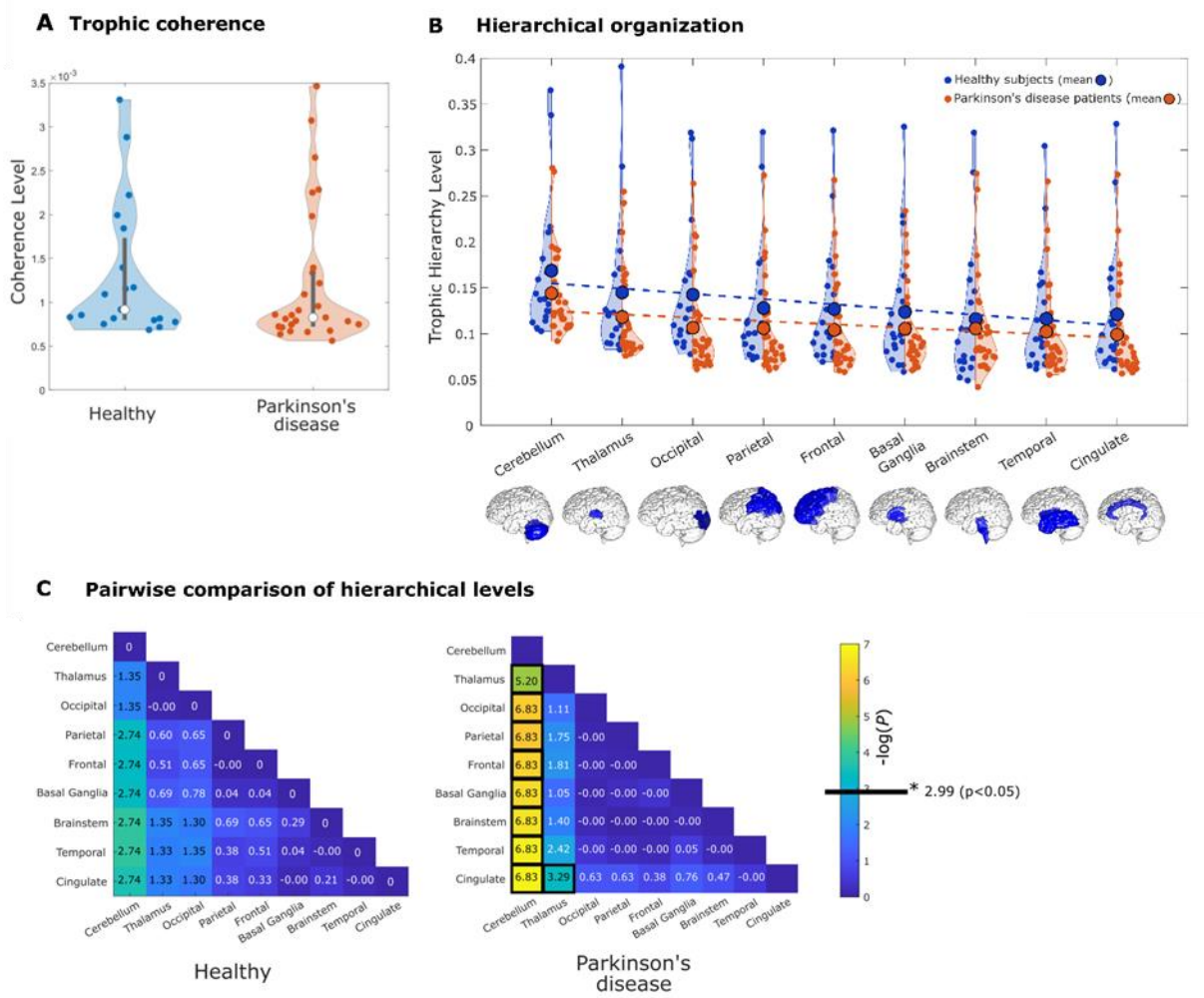

Figure 7. Trophic hierarchical organization is altered in PD. Trophic coherence and hierarchical levels are computed as the symmetry of information in- and out-flow in the bidirectional graph of whole-brain GEC models. **A)** The comparison of global network coherence reveals a slight decrease in PD, though not reaching statistical significance. **B)** Trophic hierarchical organization across major brain regions revealed lower hierarchical indices in PD, with a visible relative flatness, as evidenced by the slopes of fitted lines. **C)** Statistical results identify the cerebellum and thalamus as having notably higher hierarchical positions in PD, with significance expressed through -log(*P*) values. The bold black line delineates a significant threshold, reflected by P-values < 0.05, and in the matrices, the significant values are outlined by black boxes.

5.4 Discussion

We found deviations from equilibrium in the PD state as evidenced by elevated levels of non-reversibility across multiple spatial levels. Moreover, we found PD to be associated with unique non-reversibility patterns distinct from the disease state. Furthermore, we noted alterations in the disease's hierarchical organization, marked by a more flattened hierarchy and significant shifts in how the cerebellum and thalamus interact with other brain regions.

The lowered equilibrium level and time reversibility observed in PD suggest substantial disruptions in the brain's normal temporal evolution, or brain dynamics, even in relatively early stages of the disease (average disease duration in our study = 3.69 years). While previous findings on PD dynamics have yet to reach a consensus on methodology and findings (Darbin et al., 2013), the observed imbalance aligns with reports of structural and functional impairments due to PD across multiple scales, which can result in disruptions of the fine-tuned coordination of motor- and non-motor processes in a healthy flexible brain. Previous studies investigating localized and motor-network-oriented brain dynamics in PD have reported alterations in the normal spatiotemporal synchronisation patterns in the brain, which disrupt the normal coding of movement (Sharott et al., 2018; West et al., 2018). Additionally, using alternative measures such as electroencephalographic brain activity, Zanin et al., (2020) have demonstrated an increased level of non-reversibility in PD. This heightened global chaos in information processing in the PD brain serves as a potential marker for pathologically affected dynamics, as suggested by graph theory and alternative resting-state functional MRI research (Ghasemi and Mahloojifar, 2013; Kim et al., 2017).

The observed global increase in information processing entropy in PD serves as a potential marker for pathologically affected dynamics, a finding that aligns with reports from graph theory and alternative rs-fMRI investigations (Ghasemi and Mahloojifar, 2013; Kim et al., 2017). By analysing non-reversibility levels in individual nodes, we uncover a broad distribution in PD, indicating shifts in the dynamic equilibrium in PD. In particular, the BTC and CTC networks, which are central to tremor pathophysiology as discussed in Chapter 1 (Caligiore et al., 2016; Dirkx and Bologna, 2022; Duval et al., 2016), both exhibit elevated significant non-reversibility levels. This increase suggests distortions in either regional disruptions, issues in network synchronisation during resting state, or a combination of both. These observations follow the existing knowledge on abnormal sensorimotor integration in PD leading to a broader sense of disconnectedness across the brain (Göttlich et al., 2013; Helmich et al., 2010).

We constructed individualized computational models based on rs-fMRI data while integrating information from SC, and FC, and non-reversibility, resulting in whole-brain directed GEC graphs, to enhance our understanding of pathological brain dynamics in PD. Despite the lack of extensive knowledge on underlying mechanisms of PD and tremor (Miller and O'Callaghan, 2015), the application of MRI imaging techniques, particularly when augmented with computational modelling methods, has shown promise in uncovering underlying pathologies and enhancing diagnostic processes (Breakspear, 2017; Deco and Kringelbach, 2014; Makarious et al., 2022; Poewe et al., 2017).

To confirm the effectiveness of our computational models, we employed an SVM to perform pattern separation between PD and healthy states based on resulting effective connectivity graphs reflecting non-reversibility measures. It is important to note that our primary focus was not on classification per se,

especially considering the limitations imposed by our small sample size and the challenges in achieving broad generalizability. Our objective was primarily to test the uniqueness of non-reversibility models in PD. The high levels of accuracy observed across various scales highlight the informativeness of these models. Interestingly, alternative attempts with FC or SC resulted in significant drops in precision, indicating the robustness of the arrow of time methods in capturing the distinctive dynamics of PD.

By incorporating temporal asymmetry as in our study, we were able to capture the distinct patterns of spatiotemporal organization across the brain across in healthy and disease states. The results revealed alterations in hierarchical organization in PD, highlighting how brain dynamics can be orchestrated differently due to this disease. System-level disorders such as PD disrupt this precise organization, leading to deviations in information processing. These disruptions are believed to stem from pathological alterations in beta oscillations, particularly within the BTC network, which are associated with dopamine depletion in PD (Cagnan et al., 2019; Moran et al., 2011; Reis et al., 2019). Elevated beta activity has been linked to disruptions in the hierarchical organization, which in turn may compromise the equilibrium of the brain's entire hierarchy (West et al., 2018).

Notably, our findings reveal a distinctive flattening of the trophic hierarchy in PD, marking a deviation from earlier studies that associated flatness of hierarchy with reduced non-reversibility in specific brain conditions (Deco et al., 2022; Kringelbach et al., 2023). By analysing trophic hierarchy through the lens of information flow in the effective connectivity graph, we offer a novel perspective. Specifically, in the case of PD, the observed combination of a flattened hierarchy combined with increased non-reversibility points to a less dynamic repertoire in the brain. This reduced flexibility is associated with impaired functional organization, decreased causal interactions, and compromised information flow, all contributing to the severity of PD symptoms such as tremor (Ghasemi and Mahloojifar, 2013; Kim et al., 2017; Sorrentino et al., 2021).

Our findings indicate that the cerebellum holds a high trophic hierarchy level in both healthy and PD states, challenging recent theories that prioritize the prefrontal cortex and highlighting the overlooked significance of the cerebellum in computational models (Deco et al., 2023; Kringelbach et al., 2023). The prominence of the cerebellum could be due to its rich functional architecture and extensive brain connections (Stoodley et al., 2021). In the PD state, the cerebellum's elevated position in the hierarchical organization potentially indicates a compensatory function besides its direct pathological involvement (Caligiore et al., 2017; Wu and Hallett, 2013). This shift is similar to observed alterations in cerebellar reserve and the adaptive role of this region in conditions affecting motor functions such as stroke (Mitoma et al., 2020; Sadeghihassanabadi et al., 2022a; Wu and Hallett, 2013). Additionally, an increased hierarchical ranking of the thalamus points to disruptions in the CTC network (Dirkx and Bologna, 2022; Obeso et al., 2008; Toni et al., 2012). While intriguing, definitive conclusions about hierarchy require further symptom- and task-specific investigations. It's important to clarify that the notion of hierarchy in this context arises from the brain's inherent self-organizational characteristics, rather than from a rigid top-down framework. This viewpoint, as articulated by Buzsáki, suggests the existence of multiple dynamic structures that interact within a specific hierarchical organization to facilitate rapid temporal solutions, with the goal of efficient collective computation (Buzsáki, 2009). We further acknowledge the limitation of having a small sample size, which potentially impacts the

robustness of machine learning (SVM) results. Furthermore, basing the SVM's input—individual effective connectivity patterns—on an averaged SC matrix for each group introduces another layer of complexity. To address these concerns, we expanded our SVM analysis to include alternative inputs such as SC, FC, and the use of no-network models.

A novelty aspect of this study lies in employing a detailed parcellation, incorporating subcortical regions and the cerebellum, which allowed for investigating their roles in the whole brain dynamics of PD. Yet, large parcellations introduce certain statistical challenges, particularly arising from multiple comparisons. To minimize the risk of false positives, we selected distinct spatial scales for analysis and incorporated *a priori* assumptions on pathological networks in PD. Future studies are encouraged to include larger sample sizes to enhance statistical power and look into the association between non-reversibility measures and motor- and cognitive symptomology of PD.

Research has demonstrated that targeted interventions like DBS can facilitate a transition from a PD state to a healthier neurological state (Saenger et al., 2017; West et al., 2022). This study's findings highlight the cerebellum's prominent role in the brain's hierarchical organization and its increased influence in the PD state, therefore suggesting that stimulating the cerebellum could alter the equilibrium measures of the CTC network and potentially impact the entire brain state. In other words, by applying correct cerebellar stimulation, there is potential to shift brain dynamics towards healthier functioning.

In conclusion, our findings indicate that PD disrupts the brain's equilibrium across multiple spatial scales. With our computational models providing novel insights into the disease's dynamical implications, this study supports the usage of computational approaches rooted in empirical imaging techniques to study the underlying pathology of PD and its symptoms. The observed flatness in hierarchical organization suggests diminished flexibility in the brain's dynamic repertoire due to PD. The crucial role of the BTC and CTC networks in distorted brain dynamics highlights their involvement in PD pathology. Notably, the cerebellum's influence in the hierarchical organization is increased in the PD state. The results of this study indicate that cerebellar stimulation could be a potent method for restoring equilibrium to the CTC network, and subsequently, the overall brain dynamics, steering them towards healthier functional states. This highlights a promising avenue for interventions focused on the cerebellum in managing PD symptoms.

Chapter 6 : Non-invasive Stimulation of the Cerebellum

Part One: Optimizing the Electrode Montage for Cerebellar Stimulation

The first part of the chapter presents the optimized paradigm for non-invasive stimulation of the cerebellum aimed at suppressing PD tremor, based on the published study titled '**Optimizing the montage for cerebellar transcranial alternating current stimulation (tACS): a combined computational and experimental study**' by Sadeghi et al. (2022b). In this study, my contributions included conceptualization and design of the study, data collection and analysis, and manuscript writing.

6.1 Introduction

As the scope of cerebellar tACS expands, there's an increasing focus on the potential adverse effects stemming from peripheral side effects, which may influence or even negate the intended transcranial outcomes of the simulation (Asamoah et al., 2019; Lorenz et al., 2019). Among the most commonly reported side effects are skin sensations (Fertonani et al., 2015; Hsu et al., 2021; Turi et al., 2013). In particular, the application of strong tACS which induces a relatively high electric field on the skin's surface, exceeding 4-7 V/m, can directly stimulate the cutaneous nerves and cause unpleasant sensations including itching, pricking, warmth, and pain (Bland and Sale, 2019; Hsu et al., 2021). Additionally, an intriguing side effect encountered during cerebellar tACS is the occurrence of phosphenes, perceived as flickering lights or flashes within the visual field (Antal and Paulus, 2013; Wessel et al., 2022). Initially thought to be a byproduct of stimulation of the visual cortex (Kanai et al., 2008), further research has clarified that phosphenes primarily originate from the retina (Kar and Krekelberg, 2012; Laakso and Hirata, 2013; Schutter and Hortensius, 2010). Notably, the manifestation of these side effects is contingent upon the specific montage and frequency of the tACS application (Asamoah et al., 2019; Evans et al., 2019; Hsu et al., 2021; Lorenz et al., 2019), highlighting the complexity of achieving desired effects while managing peripheral stimulation outcomes. A critical aspect influencing the severity and perception of these side effects is the strategic placement of the tACS electrodes (Evans et al., 2019; Mehta et al., 2015). This placement not only determines the intensity and distribution of the electric field across the cerebellum but also significantly affects the likelihood and intensity of experiencing these side effects, highlighting a delicate balance between therapeutic efficacy and patient comfort (Klaus and Schutter, 2021).

To date, a holistic exploration of the skin-related effects and the phenomenon of phosphenes during cerebellar tACS, with an emphasis on the influence of electrode montage and stimulation frequency, remains absent (Bland and Sale, 2019). An experimental investigation to identify optimal stimulation parameters that promise clinical utility would require conducting repetitive tACS sessions with human participants, while systematically varying stimulation conditions. Such a strict experimental approach would be challenging in terms of safety and ethical concerns, methodological complexities, and importantly accurate quantification and interpretation of the effects observed (Brunoni et al., 2012). In contrast, in-silico or computational modelling studies emerge as a potent alternative, circumventing these limitations and offering the advantage of detailed insight into the stimulation's impact on brain

tissues. Such studies typically involve simulating multiple tACS sessions under a range of conditions, thereafter computing the current distribution within the targeted brain region. This is achieved by solving the current continuity equation, taking into account the necessary boundary conditions and the varying conductive properties of different tissues, such as the skull and brain (Priori et al., 2014). This methodological approach not only ensures a safer and ethically sound investigation pathway but also enhances the precision with which the effects of stimulation on brain tissue are understood.

Addressing the critical gap in the field, this study is dedicated to identifying the optimal cerebellar tACS montage that maximizes efficacy while minimizing unpleasant side effects. Despite the promising potential of cerebellar tACS, its application, particularly in clinical settings, is significantly hindered by the presence of undesirable side effects and the absence of universally accepted stimulation protocols. Our approach to overcoming these challenges combines computational modelling and experimental application. Through computational modelling, we were able to assess the effects of various electrode montages on current density in the cerebellum and identify potential induction in other brain areas that might contribute to stimulation side effects. Following this, we conducted *in vivo* experiments with selected montages on healthy individuals in a controlled setting, focusing on evaluating the side effects associated with skin sensations and phosphenes. This comprehensive strategy not only facilitates the practical application of cerebellar tACS but also lays the groundwork for establishing standardized protocols, enhancing the technique's usability and effectiveness in both research and clinical environments.

6.2 Methods

6.2.1 Computational Methods

6.2.1.1 Main Electrode Position

Simulations were conducted using a boundary element model (BEM) framework, incorporating a realistic three-shell head model that delineates the skin, bone, and brain compartments (Nolte and Dassios, 2005). The head model was constructed using the standard MNI152 template, augmented with an intricate cerebellar surface model derived from the Spatially Unbiased Infratentorial Template (SUIT) (Diedrichsen, 2006). The estimation of electric fields across the brain was achieved by calculating the sum of linear combinations of a leadfield $\vec{L}$ and the injected currents from all stimulation electrodes α_i at each intracranial location $\vec{x}$ as

$$\vec{E}(\vec{x}) = \sum_i \left(\vec{L}(\vec{x})\alpha_i\right) \qquad [17]$$

The leadfield was constructed through exact low-resolution electromagnetic tomography (eLORETA) (Pascual-Marqui et al., 2011). To simulate the patch electrodes, commonly sized at 5x5 cm, we adopted a nine-point array approximation. These points were strategically placed at distances of 0, 1, 2, and 3 cm from the inion. The inion's location was precisely identified using MNI coordinates [0, -120, -21] (Tsuzuki et al., 2016). To analyse the electric current distribution across the cerebellum's surface, we

employed two-sided signed rank tests, with a Bonferroni correction applied to adjust for the risk of type I errors due to multiple comparisons, ensuring the reliability of our findings.

6.2.1.2 Return Electrode Position

To determine the most effective return electrode position, or montage, comprehensive simulations of full tACS sessions were conducted using SimNIBS software (version 3.2.4, (Thielscher et al., 2015)). These simulations employed the standard MNI152 head model, with tissue conductivities assigned in line with the specifications provided by Wagner et al. (2004). The design included rectangular electrodes in two dimensions, 5x5 cm and 5x7 cm, mirroring the characteristics of neuroConn silicone rubber electrodes. These were specified with a conductivity of 29.4 S/m and a thickness of 1 mm, complemented by a sponge covering featuring a conductivity of 1 S/m and a thickness of 2.5 mm, as per recommendations by the SimNIBS Developers SimNIBS Developers (2019). For these simulations, the central point of the main (5x5 cm) electrode was consistently positioned 2 cm lateral to the inion, a placement optimized through the previous simulation outcomes. The larger return electrode (5x7 cm) was then variably placed at the central coordinates corresponding to the four most commonly cited montages in the existing literature: the forehead, the ipsilateral buccinator muscle, the lower jaw, and the lower neck. To mirror the actual peak-to-peak amplitude typically used in tACS applications, the amplitude was set at ±2mA, following the guidelines proposed by Saturnino et al. (2017).

To determine the current distributions induced by the tACS stimulation in SimNIBS, first, the Laplace equation is solved as [18].

$$\nabla \cdot (\sigma \nabla \emptyset) = 0 \qquad [18]$$

Where σ represents the electrical conductivity of a specific tissue type, and $\emptyset$ denotes the induced electrical potential. The process is modelled by setting precise boundary conditions. By solving for these conditions, we obtain a detailed solution that facilitates the calculation of both electrical (E) and current (J) distributions as they flow between the main and return electrodes as given in [19] and [20].

$$E = -\nabla \emptyset \qquad [19]$$

$$J = \sigma E \qquad [20]$$

Finally, adjustments and linear scaling are applied to ensure that the current flow through the electrodes aligns with the predetermined values, a crucial step for accurate simulation results (Parazzini et al., 2014; Saturnino et al., 2018). To assess the effects of the stimulation, an ROI analysis was conducted. This involved the extraction and calculation of lobule-specific current densities using SUIT tools within MATLAB. These calculations informed the creation of cerebellum flatmaps, providing a visual representation of the stimulation's impact across different regions of the cerebellum. Moreover, the potential co-stimulation of the eyeballs—a factor indicative of the likelihood of inducing phosphenes, as noted by (Laakso and Hirata, 2013) —alongside the brainstem was scrutinized. For this purpose,

specific ROI masks were developed in MRIcroGL (Rorden and Brett, 2000), which were then applied to the outputs generated by the SimNIBS 3D head model.

6.2.1.3 Focal 4x1 Electrode Arrangement

An additional simulation of cerebellar tACS with a high-definition 4x1 ring electrode montage was conducted to compare the electric field distribution and density of cerebellar stimulation with the previously discussed rectangular electrodes. Following the guidance of (Saturnino et al., 2015), the simulation incorporated five circular electrodes, each with a diameter of 1.2 cm. These were arranged in a ring, with the central electrode placed 2 cm lateral to the inion, and the four peripheral electrodes evenly spaced at a radius of 3.5 cm from the center. Consistent with earlier simulations, the same silicone rubber material was selected for the electrodes, and the conductivities assigned to both the electrodes and the various tissues remained unchanged. For this specific arrangement, the current was set at +2 mA for the central electrode, with each of the surrounding four electrodes adjusted to -0.5 mA to create a balanced field. The analysis, including the extraction of current density within the cerebellum and lobular ROI assessments using the SUIT toolbox, mirrored the methodologies applied in the previous simulations.

6.2.2 Experimental Methods

6.2.2.1 Participants

In this study, seven healthy right-handed individuals (3 female, mean age 33 years, SD = 7) were recruited after giving informed written consent. All participants were free from neurological or psychiatric disorders or tACS contraindications. The procedure has been approved by the local ethics committee of Hamburg and was conducted in accordance with the Declaration of Helsinki.

The experimental setup involved seating participants in a comfortable chair within a dimly lit room, positioned two meters from a 55-inch monitor (Sony Group, Tokyo, Japan). The monitor displayed a black background with a white cross at its centre, serving to maintain a consistent visual focus for the participants throughout the experiment. The study design included four stimulation blocks corresponding to each electrode montage, executed consecutively for every participant in a pseudo-randomized sequence with approximately 60-second intervals between blocks. Each block comprised three distinct stimulation frequencies (5, 10, and 30 Hz) and a sham condition, presented in a randomized order, with each condition lasting three minutes. Participants had their eyes closed for the latter half of each stimulation period and were unaware of the specific stimulation conditions.

To assess participants' sensory experiences, they were queried about perceived skin sensations (itching, warmth, pricking, and pain) and the intensity and spatial extent of phosphenes within their visual field, both with eyes open and closed. The intensity levels were rated using a discrete ordinal scale of 1:absent, 2:light, 3:moderate, 4:clear, and 5:strong sensation. Phosphene coverage was visually represented by participants through cross-hatching or drawing on a blank rectangular template simulating the monitor screen, later quantified as the ratio of marked area to the total area of the rectangle. Additionally, the presence of breathing difficulties or autonomic dysfunctions was monitored as potential indicators of unintended brainstem co-stimulation (Vandermeeren et al., 2010).

6.2.2.2 Stimulation

tACS stimulation was carried out using a battery-powered DC Stimulator Plus (neuroConn, Ilmenau, Germany), with standard rubber electrodes wrapped in saline-moistened sponges (0.9% NaCl), secured by medical elastic bandages (MaiMed GmbH, Germany). Throughout all stimulation sessions, impedance was carefully maintained at ≤10 kΩ. The primary electrode (5 x 5 cm²) was positioned 2 cm lateral to the inion, with the return electrode (5 x 7 cm²) placed at the four predetermined positions, namely the forehead, the ipsilateral buccinator muscle, the lower jaw, and the lower neck. Stimulation frequencies of 5, 10, and 30 Hz were applied at a peak-to-peak amplitude of 2 mA, apart from the sham condition, which included a 30-second ramp-up and ramp-down period.

6.2.2.3 Statistical Analysis

Statistical analyses were executed utilizing Python 3 (Python Software Foundation, http://www.python.org) and MATLAB (The MathWorks, Inc., 2021). Data derived from the main tACS electrode did not fulfil normal distribution assumptions and therefore were analysed using the Wilcoxon signed-rank tests with Bonferroni correction to adjust multiple comparisons. The influence of electrode montage on the distribution of current density was explored using a one-way analysis of variance (ANOVA). To assess the combined effects of montage and frequency on participants' reported skin sensations and the intensity of phosphenes, the Scheirer-Ray-Hare (SRH) test was employed. Additionally, a two-way ANOVA was utilized to assess these variables' impact on the areas covered by phosphenes. Subsequent analyses, where applicable, involved post-hoc Tukey tests, with adjustments of p-values for multiple comparisons conducted through the FDR method (Benjamini and Hochberg, 1995).

6.3 Results

6.3.1 Computational Results

6.3.1.1 Optimal Position of the Main Electrode

Shifting the main electrode to a more lateral position on the scalp progressively reduced the stimulation of the contralateral side, achieving the lowest levels of co-stimulation when positioned 3 cm lateral to the inion, as depicted in Figure 8 (all statistical comparisons were highly significant with $p < 0.001$). In terms of electric current effects within the ipsilateral hemisphere of the cerebellum, the intensities were found to be similar when the electrode was positioned at 0 and 1 cm from the inion. The intensity peaked for the electrode placement at 2 cm, and was at its lowest with the electrode at 3 cm from the inion (0/1: $p = 0.101$, 0/2: $p = 0.333$, 0/3: $p < 0.001$, 1/2: $p < 0.001$, 1/3: $p < 0.001$, 2/3: $p < 0.001$). Analysis of the simulated current density distributions across the cerebellar surfaces further confirmed that situating the main electrode 2 cm lateral to the inion provided optimal targeting of the right cerebellar hemisphere while minimizing unintended stimulation of the contralateral hemisphere.

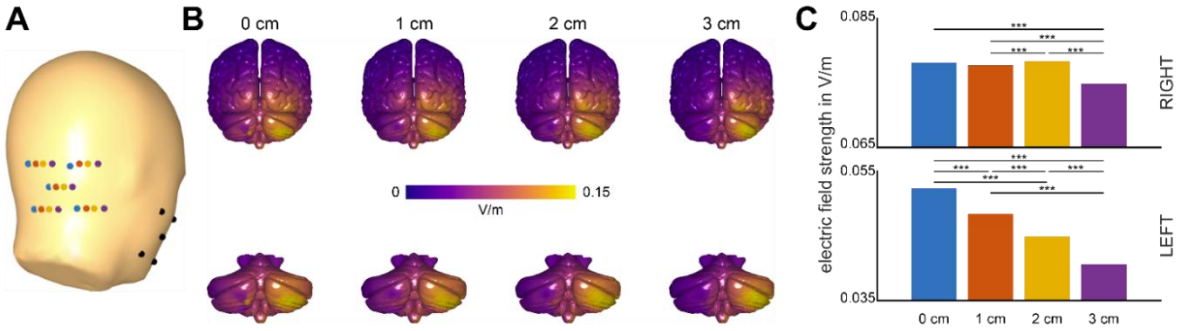

Figure 8. Placement and effects of main tACS electrode across four locations. **A)** Configuration of electrode patches represented by five designated points. Positioned starting from the inion (the upper leftmost blue dot), the patches are sequentially displaced rightward by 0, 1, 2, or 3 cm. The corresponding return electrode placed on the buccinator muscle remains unchanged. **B)** Depiction of the electric fields generated by each electrode setup, illustrated for both the entire brain (top row) and the cerebellum in isolation (bottom row). **C)** Comparison of median electric field intensity within the cerebellum's right hemisphere (ipsilateral, top graph) and left hemisphere (contralateral, bottom graph), with significant differences highlighted (*** denotes $p < 0.001$).

6.3.1.2 Effect of Montage on the Stimulation Strength in the Cerebellum

Figure 9 illustrates the placement and effects of the main tACS electrode across four distinct locations. The one-way ANOVA analysis revealed a significant influence of electrode montage on the mean current density within the right hemisphere of the cerebellum, with $F(3,48) = 3.59$ ($p = 0.02$). Further exploration through post-hoc pairwise comparisons using the Tukey test identified a significant difference between the forehead and neck montages ($p = 0.02$). However, comparisons between the forehead and jaw ($p = 0.05$), forehead and buccinator ($p = 0.11$), buccinator and jaw ($p = 0.98$), buccinator and neck ($p = 0.86$), and jaw and neck ($p = 0.98$) montages did not reveal significant differences. For a comprehensive breakdown of activations within individual cerebellar lobules, refer to the Supplementary Materials.

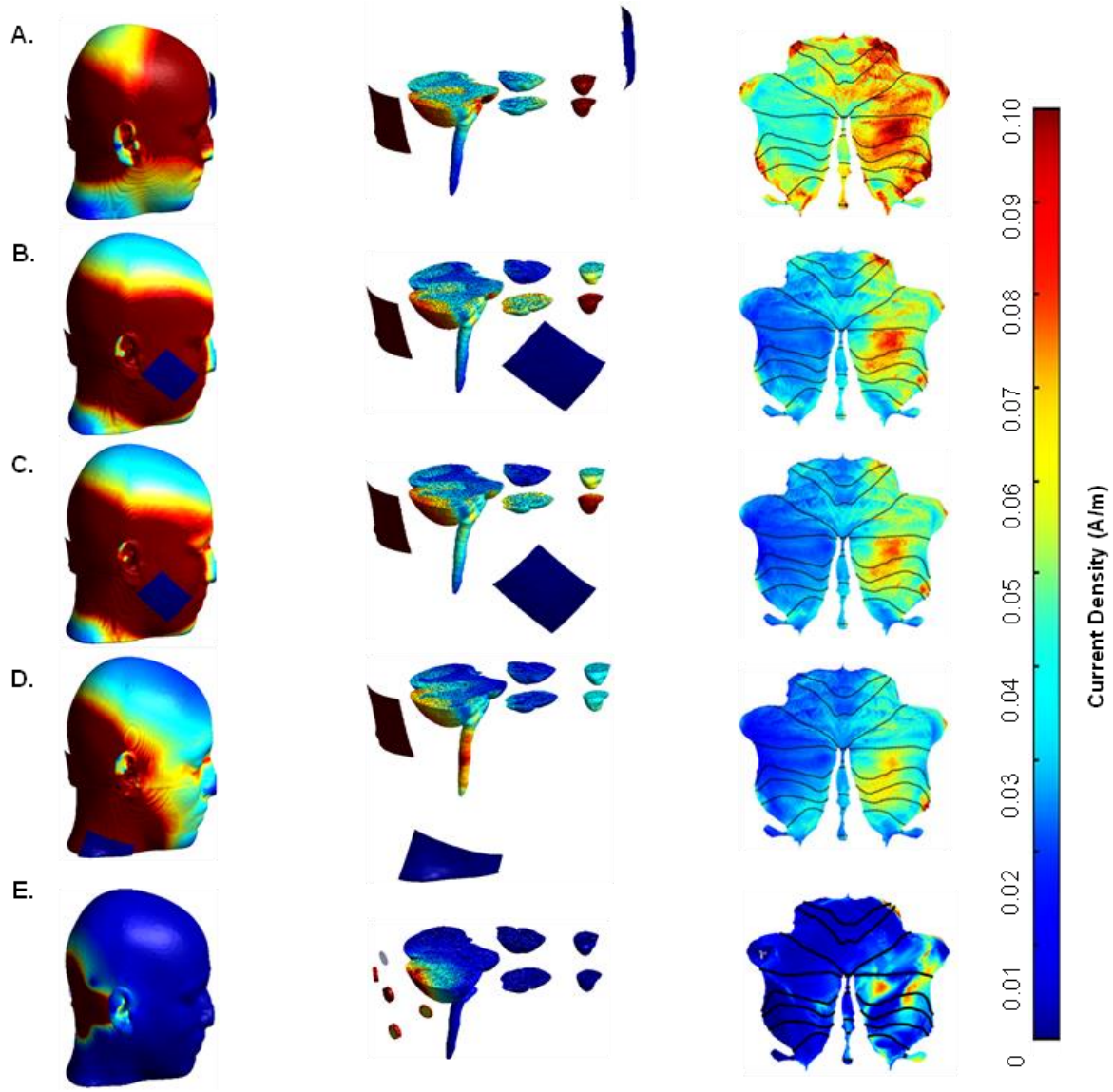

Figure 9. Simulations of various tACS montages and corresponding stimulation intensities. The effects of different tACS stimulations are observable on the skin, cerebellum, and eyeballs across various configurations: **A)** with the return electrode positioned on the forehead, **B)** on the buccinator muscle, **C)** on the jaw, **D)** on the neck, and **E)** utilizing a 4x1 ring electrode setup. The images are organized to show: on the left, a complete view of the scalp; in the middle, a cross-sectional view highlighting the cerebellum and eyeballs; and on the right, detailed cerebellum flatmaps that map the distribution of current density.

6.3.1.3 Effect of Montage on Co-stimulation of the Eyeballs and the Brainstem

ROI analysis of both eyeballs and the brainstem was performed using SimNIBS and MRIcroGL. Supplementary Table S9 presents descriptive statistics for current density measurements in both regions. To examine the impact of different tACS montages on current density distributions within these ROIs, a one-way ANOVA was conducted. The findings indicated a significant effect of stimulation montage on current density both in the eyeballs ($F(3, 44380) = 133304$, $p < 0.0001$) and in the brainstem ($F(3, 95164) = 15530$, $p < 0.0001$). Subsequent post-hoc analysis using the Tukey test revealed significant differences in mean current density between all montage pairings (forehead-buccinator, forehead-jaw, forehead-neck, buccinator-jaw, buccinator-neck, jaw-neck), as detailed in Figure 10.

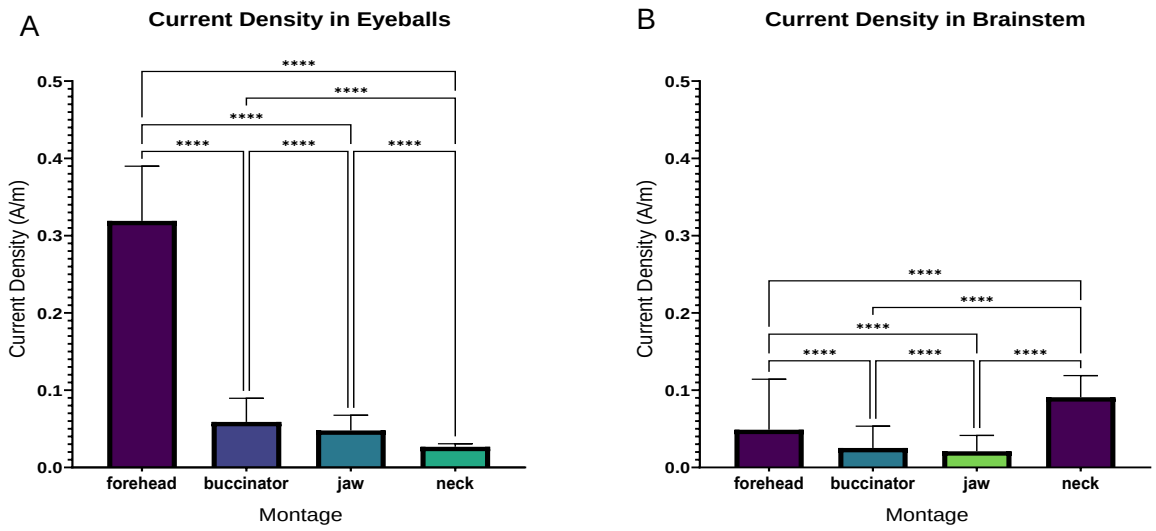

Figure 10. Mean current density analysis across four tACS montages. This figure presents a comparative analysis of mean current density within **A)** the eyeballs and **B)** the brainstem for the four tACS electrode placements: forehead, buccinator muscle, jaw, and neck. The statistical analysis confirms that all observed differences in mean current densities are significant.

6.3.1.4 Comparing Classical and 4x1 Ring Montage

The comparison of mean current density within cerebellar lobules across the four classical electrode montages and the 4x1 ring electrode setup was conducted using one-way ANOVA. The analysis revealed that the current distribution induced by the ring montage was significantly lower when compared to each of the four classical montages. The current distribution induced by ring montage was significantly lower than all four montages (compared to forehead: $F(1, 24) = 100$, buccinator: $F(1, 24) = 41$, jaw: $F(1, 24) = 33$, neck: $F(1, 24) = 49$, with $p < 0.0001$ for all comparisons).

6.3.2 Experimental Results

6.3.2.1 Effect of Montage and Frequency on Skin Sensations

All participants concluded the experiment without experiencing any pain, discomfort, or other serious adverse effects, such as breathing difficulties or palpitations, as illustrated in Figure 11A-B and detailed in Supplementary Table S10**Table S10**. An analysis utilizing the two-way SRH test revealed that neither the montage nor the frequency, nor their interaction, had any significant impact on the intensities of the four skin sensations (refer to Supplementary Table S11 for detailed statistics).

6.3.2.2 Effect of Montage and Frequency on Phosphene Intensity

In conditions where participants had their eyes open, the intensity of perceived phosphenes was influenced by the montage (Figure 11C, $H(3,72) = 8.15$, $p = 0.04$). However, the frequency of stimulation (Figure 11D, $H(2,72) = 0.93$, $p = 0.62$) and the interaction between montage and frequency ($H(6,72) = 0.83$, $p = 0.99$) did not show significant effects. Despite the overall effect of montage, post-hoc Tukey tests revealed no significant differences between any pairs of montages under these conditions. Conversely, with eyes closed, phosphene intensity significantly varied across montages ($H(3,72) = 52.65$, $p < 0.001$), while the frequency of stimulation ($H(2,72) = 3.39$, $p = 0.18$) and the interaction

between montage and frequency (H(6,72) = 2.74, p = 0.83) did not yield significant differences. Post-hoc analysis demonstrated significant differences between all montage pairs. The sequence of montage effectiveness in inducing phosphenes, from highest to lowest, was the forehead, followed by the buccinator, jaw, and neck, as illustrated in Figure 11C.

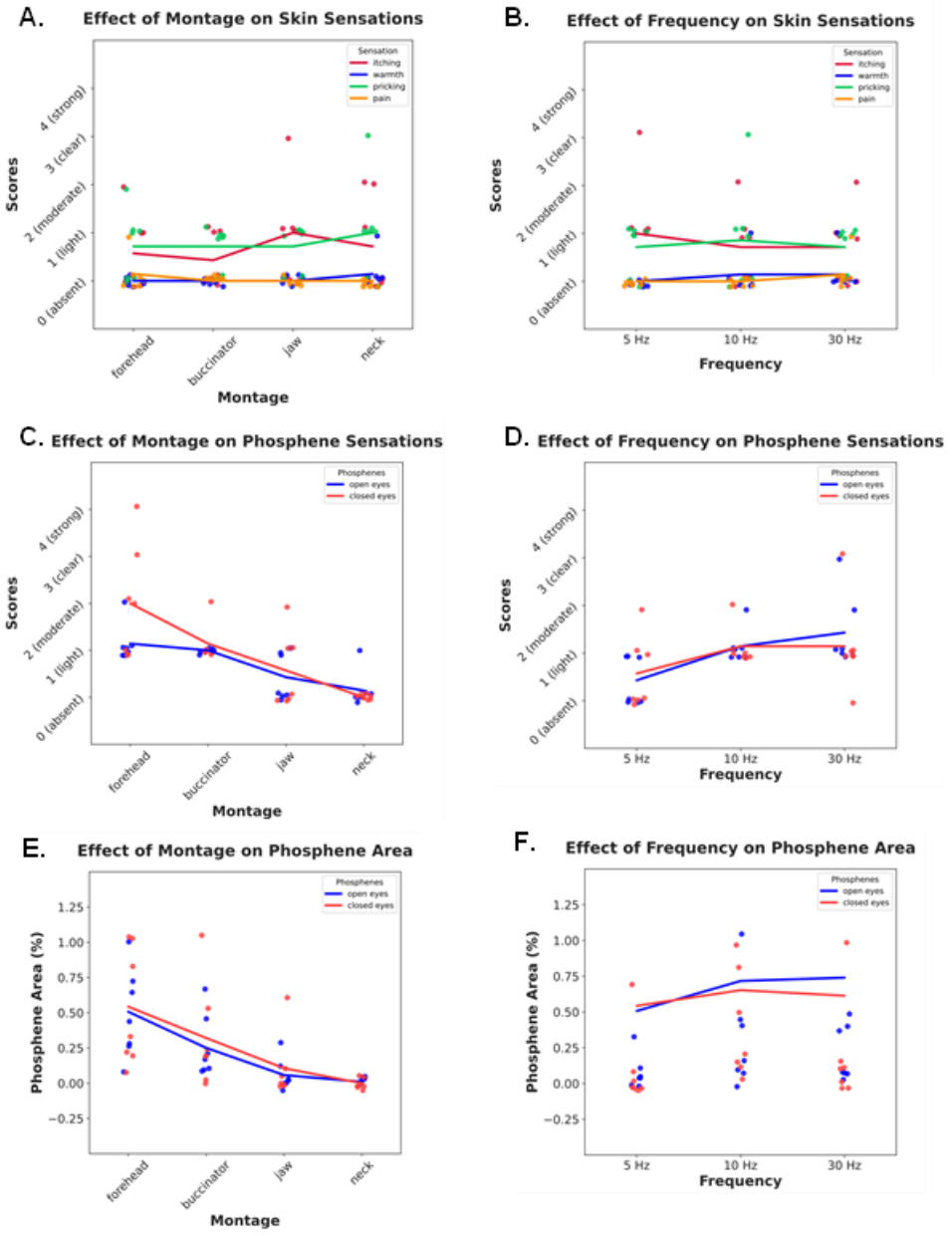

Figure 11. Impact of montage and frequency on sensory responses and phosphene perception. A-D) the influence of montage placement (forehead, buccinator, jaw, neck) and stimulation frequency (5, 10, 30 Hz) on reported skin sensations and phosphene intensity. These effects are shown through scattered plots of individual participant scores and aggregate line graphs summarizing average scores, incorporating results from ANOVA. **E-F)** the montage and frequency impact on the phosphene coverage area, quantified for each participant by comparing the sketched phosphene area to the total monitor screen area, alongside average coverage areas and their statistical analysis through ANOVA.

6.3.2.3 Effect of Montage and Frequency on Phosphene Areas

The spatial extent of phosphenes perceived in the visual field was significantly influenced by both the montage and frequency of stimulation, as determined by a two-way ANOVA. The analysis revealed that montage had a substantial effect ($F(3,72) = 19.89$, $p < 0.001$), as did frequency ($F(2,72) = 4.75$, $p = 0.01$), though their interaction did not produce a significant influence ($F(6,72) = 0.50$, $p = 0.79$). Post-hoc analysis elucidated these effects further, indicating significant differences in phosphene area between the forehead montage and all other montages tested (buccinator: $p = 0.01$, jaw: $p < 0.001$, neck: $p < 0.001$), and between buccinator and neck montages ($p < 0.001$). However, the comparison between jaw and neck montages did not reveal a significant difference ($p = 0.35$). Regarding the impact of frequency, there was a significant distinction between 5Hz and 10Hz ($p = 0.01$), while the comparisons between 5Hz and 30Hz ($p = 0.05$), and between 10Hz and 30Hz ($p = 0.82$), did not show significant differences, as shown in Figure 11E-F.

Employing Spearman's rank correlation test revealed a significant correlation between the intensity of perceived phosphenes and the area of the phosphenes within the visual field. This relationship held true for both conditions of the experiment—when participants had their eyes open ($r_s = 0.84$, $p < 0.001$) and when they had their eyes closed ($r_s = 0.82$, $p < 0.001$).

6.4 Discussion

The findings of this study confirm the importance of electrode placement in determining the resulting electric field and, by extension, the current density within the cerebellum. The alignment between simulation outcomes and experimental data indicates the influence of montage on both the efficacy of cerebellar tACS and its associated side effects. These results confirm earlier findings in emphasizing the significance of electrode placement for stimulation effectiveness (Gomez-Tames et al., 2019; Mehta et al., 2015; Priori et al., 2014; Wessel et al., 2022) and side effects (Evans et al., 2019; Kanai et al., 2008; Turi et al., 2013).

Among the montages we tested, the forehead montage emerged as the most effective in stimulating the ipsilateral hemisphere of the cerebellum. The pronounced stimulation effect observed with the forehead montage can likely be attributed to the direction of the current flow vectors passing directly through the cerebellum, from the inion towards the forehead. This direct path facilitates the induction of higher current densities compared to montages that direct the current away from the cerebellum, such as the neck montage. This principle aligns with the findings of Klaus and Schutter (2021), who discussed the variability in induced field direction due to electrode positioning in transcranial direct current stimulations. Our findings indicate that the ring electrode montage is less effective compared to traditional sponge electrode protocols, consistent with recent studies that suggest high-definition ring electrodes produce suboptimal current distribution within the cerebellum (Klaus and Schutter, 2021).

Moreover, the forehead montage is associated with the most significant phosphene effect, which supports our simulation results revealing the highest current density induction in the eyeballs with this montage. This increased current density in the eyeballs accounts for the stronger phosphene sensations, given the retinal origin of phosphenes (Schutter and Hortensius, 2010). As the return electrode is positioned lower down, towards the neck, there is a corresponding decrease in cerebellar

current density and phosphene intensity, highlighting the intricate relationship between electrode placement, stimulation efficacy, and side effects in cerebellar tACS.

Throughout all tACS sessions, participants reported low skin sensations, a phenomenon seemingly independent of the montage selection. This could be attributed to the maintenance of low impedance levels facilitated by the use of elastic bandages, which ensured optimal electrode-skin contact, as emphasized by Woods et al. (2016). Furthermore, the employment of classical large sponge electrodes likely contributed to minimizing skin sensations. This contrasts with the use of smaller, multiple-ring electrodes, which have been associated with more pronounced cutaneous sensations (Herrmann et al., 2013).

The impact of frequency alteration on skin sensation intensities also did not present a consistent pattern across our study. While some previous findings confirm that frequency does not significantly influence skin sensations (Fertonani et al., 2015), other studies suggest otherwise (Hsu et al., 2021; Turi et al., 2013). The question of whether the cutaneous effects of tACS are dependent on stimulation frequency however remains a subject of debate. Hsu et al. (2021) have provided a comprehensive analysis suggesting a reduction in skin sensations at higher frequencies, a phenomenon not observed in our study. Given that both our study and that of Hsu et al. (2021) reported overall low levels of cutaneous sensations, the disparity in findings might stem from a floor effect, limiting the observable impact of frequency on skin sensations. Additionally, divergences in findings regarding frequency-dependent effects could be ascribed to methodological differences across studies, such as variations in applied montages, electrode types, and stimulation frequencies. Such variability underscores the complexity of accurately gauging the impact of frequency on tACS-induced sensations and emphasizes the need for standardization or more detailed reporting in experimental setups to better understand these effects (Brittain et al., 2015; Manto et al., 2021; Naro et al., 2016; Wessel et al., 2022).

In this study, the perception of phosphenes was not influenced by stimulation frequency, a result that diverges from findings in prior research (Lorenz et al., 2019; Turi et al., 2013). This discrepancy may be due to the considerable inter-individual variability in phosphene reports even within our small sample size, possibly obscuring subtle effects that might exist. However, we did observe a significant impact of montage on phosphene perception, with a preference for neck and jaw montages. This aligns with the strategy in some earlier studies suggesting positioning the return electrode on the neck or shoulder to avoid phosphene occurrence (Brittain and Cagnan, 2018; Mehta et al., 2014; Woods et al., 2016).

On that note, our findings reveal that positioning the return electrode at the neck (or lower) effectively diverts current away from the cerebellum, thus significantly reducing current density in the target area. Importantly, our simulations also indicated that these montages result in undesirable co-stimulation of the brainstem.

This study uniquely emphasizes the distinction between buccinator and jaw positions, which differ mainly in their proximity to the eyes—a nuance often overlooked in existing literature. Instances, where the jaw montage has been utilized, are sometimes reported under the term buccinator in the literature (Rezaee and Dutta, 2019), likely due to the latter's prevalence in simulation studies. Upon comparing these two specific montages, our findings advocate for the use of the jaw montage. It not only facilitates a more uniform distribution of current density within the cerebellum but also minimizes co-stimulation of both

the brainstem and retina. This detailed examination highlights the critical importance of precise electrode placement in optimizing tACS outcomes and minimizing unintended effects.

The inclusion of seven participants in the experimental component of our study introduces limitations concerning the extrapolation of our findings to broader cerebellar tACS research. This sample size, while modest, is not atypical for investigations involving cerebellar stimulation, as seen in prior studies (Brittain and Cagnan, 2018; Schreglmann et al., 2021; Shah et al., 2013). However, the potential for broader generalizations remains constrained. Furthermore, inherent limitations associated with the computational modelling aspect of our study warrant consideration. These include the use of a boundary element model, the simplification of the complex anatomy of participants' heads to a single averaged model (MNI152), and the assignment of fixed conductivity values to different tissues. These simplifications are necessary for computational feasibility but may not fully capture the nuances of individual anatomical variability. Future studies are therefore encouraged to control for interindividual variability by employing subject-specific head models derived from individual MRI data. Additionally, future research should aim to investigate the interactions between montage and frequency during cerebellar tACS in a more exhaustive manner and across larger participant cohorts.

In conclusion, by combining computational simulations with experimental findings, we present converging evidence for qualitative and quantitative distinctions among prevalent montages used in cerebellar stimulation. Taken together, our findings suggest the jaw montage as a superior choice for cerebellar tACS, offering an effective balance between minimizing side effects and achieving efficient ipsilateral cerebellar stimulation. Given the observed frequency invariance, this protocol shows promise for application across a diverse array of experimental scenarios. Establishing a standard and reproducible protocol that incorporates pre-stimulation modelling could significantly enhance the control, safety, and efficacy of cerebellar tACS experiments. Having established an optimal cerebellar tACS montage, the next chapter will focus on the practical aspects of performing an effective cerebellar tACS. It will cover the design of the experiment, the stimulation protocol, and crucially, the development of the device necessary to modulate CTC activity and suppress PD tremor.

Part Two: Development of a Closed-loop tACS Device for PD Tremor Suppression via Cerebellar Stimulation

The second part of the chapter is dedicated to the outcomes of a collaborative project between University Medical Center Hamburg-Eppendorf and neuroConn GmbH, Germany, focusing on the development of an innovative recording/stimulation device with the capability of suppressing PD hand tremor through a closed-loop, phase-adjusted cerebellar tACS paradigm. In this collaborative work, my contributions were as follows: Conceptualization and design of the closed-loop stimulation experiment; design of process flow diagram while contributing to the LOOP-IT development; test data collection, analysis, and feedback to neuroConn hardware developer at every stage; conducting pilot tests, data collection, analysis and interpretation.

6.5 Introduction

As discussed in the first part of the chapter, it is crucial to select the appropriate electrode placements and stimulation parameters to ensure both the efficacy and safety of cerebellar tACS sessions (Mehta et al., 2015; Sadeghihassanabadi et al., 2022b). Upon ensuring that the montage is accurately configured and the tACS-induced electric field (E-field) possesses sufficient strength to influence the cerebellum, the next important concern is the stimulation's characteristics and effects (Brittain and Cagnan, 2018).

The principles of tACS and entrainment have been reviewed in the general introduction. In practice, achieving entrainment requires delivering the stimulation at the right frequency, and if the intrinsic oscillator is non-stationary, continuously matching the frequency and phase of the stimulation with the intrinsic oscillator in real-time. For this reason, the application of standard open-loop tACS sine waves is suboptimal for addressing a multifaceted oscillatory challenge like PD tremor (Cagnan et al., 2014). Achieving continuous entrainment can be facilitated through closed-loop stimulation protocols, where the device acquires real-time data on the phase or frequency of the intrinsic oscillator and adjusts the stimulation signal accordingly in brief intervals throughout the stimulation session (Cagnan et al., 2017). In the context of PD and ET tremor management—the latter also possessing similar characteristics as PD tremor and being associated with a cerebellar oscillatory component—recent studies have shown successful entrainment and selective tremor suppression through closed-loop adaptive stimulation, via both invasive approaches such as DBS (Brittain and Cagnan, 2018; Cagnan et al., 2014) and NIBS methods, such as stimulating M1 or the cerebellum by closed-loop and phase-adjusted tACS paradigms (Brittain et al., 2015, 2013; Schreglmann et al., 2021).

Despite the instances of success highlighted, the outcomes of these interventions have been described as highly individualistic and generally infrequent. Specifically, in the context of PD tremor, closed-loop and adaptive cerebellar stimulation has been successful in achieving selective entrainment in one study however without leading to significant tremor suppression (Brittain et al., 2015). This limitation might be attributed to the challenges in rapidly detecting and matching the external with intrinsic oscillations. Current devices often require an external analyser, such as a computer equipped with signal analysis software, to enable real-time computations within the closed loop. The method of recording and detecting the brain's oscillatory signal also plays a crucial role. Ideally, signals would be directly captured

from the brain via electroencephalography (EEG) or magnetoencephalography (MEG). However, present-day technologies struggle with the practical details of integrating simultaneous EEG/MEG and tACS, particularly the issue of eliminating tACS-induced artefacts on EEG/MEG recordings.

Consequently, for NIBS strategies addressing PD tremor, the input signal may require acquisition from alternative sources outside of the brain such as the tremulous hand. This approach facilitates the integration with tACS; however, it introduces a time delay in phase adjustments which complicates the achievement of neural entrainment. To address this challenge, we set out to develop a device capable of executing the entire process autonomously: from tremor recording, through phase detection and analysis, to the generation and adjustment of tACS signals. This device aims to operate in real-time and independently to achieve faster and more precise performance than conventional stimulation devices or even combined systems.

6.6 Methods

6.6.1 Experiment Design

Performing closed-loop cerebellar tACS effectively to suppress PD tremor requires careful experimental design. Key considerations include handling the inherently unstable nature of PD tremor, as highlighted by Di Biase et al. (2017). Due to this instability, recording and stimulation blocks should be brief to capture periods when the tremor is visible and pronounced. This ensures that the device can accurately detect and record strong tremor, extract signal characteristics in real-time, and initiate closed-loop stimulation. Additionally, multiple runs are necessary to achieve reliable results, while also keeping the total duration of the sessions from being too long, considering the older age of typical PD patients, usually over 60 years.

Participants will be individuals diagnosed with PD according to the UK Brain Bank criteria (Postuma et al., 2015), who also exhibit noticeable hand tremor, and have no history of head trauma, other neurological disorders, psychiatric conditions, or substance misuse. Patients will be required to partake in two experimental sessions. At the onset of the first session, an assessment of motor symptom severities will be conducted via MDS-UPDRS Part III which will be repeated upon completion of the second session to serve as a clinical benchmark. Both sessions include repeated tACS interventions, framed by 5-minute periods of baseline tremor recordings preceding and succeeding the intervention to facilitate the assessment of the stimulation's impact. The protocol for each tACS intervention spans 36 seconds, initiating with a 10-second phase for tremor recording to determine the peak frequency and phase profile. This will be followed by a 10-second stimulation period, plus a 3-second ramp-up and a 3-second ramp-down phase. A subsequent 10-second tremor recording phase concludes the intervention.

The first session is designed with a focus on the characterization of tremor, with the primary objective being the identification of the optimal phase lag or '$\Delta\varphi_{sup}^{*}$' between the recorded tremor and the tACS signal. This optimal phase lag is associated with the maximal therapeutic effect, namely, the maximal suppression of tremor. In particular, the time-series data of the tremor is first converted from the time domain to the frequency domain by Fast Fourier Transform (FFT). This transformation allows for analysis of the frequency components of the signal, focusing on the tremor frequency band of interest,

such as 4-6 Hz. Following this, time-frequency plots will be generated to visualize how the power within this frequency band changes over time before, during and after stimulation. The effect of stimulation will then be assessed by using linear mixed models, which allows for addressing both fixed and random effects (tremor suppression vs. individual subject variability). To enhance the robustness of the results, multiple stimulation runs will be conducted across a spectrum of phase alignments within a session, testing various phase delays within the stimulation cycle in accordance with protocols previously established by Schreglmann et al. (2021).

In addition to the active stimulation phases, the experimental design incorporates control conditions, specifically 'Uncoupled' and 'Sham', to accurately differentiate the effects of the intervention from potential placebo effects. The 'Uncoupled' condition refers to a scenario where the stimulation phase and frequency are not synchronised with the tremor dynamics. Conversely, the 'Sham' condition mimics the active condition in terms of the ramp-up and ramp-down phases but omits the actual delivery of the stimulation current.

During the second session, the investigation progresses by employing the optimal phase lag ($\Delta\varphi_{sup}^{*}$) identified from the first session. Particularly, $\Delta\varphi_{sup}^{*}$ is used as the basis of the dynamic phase adjustments between the recorded tremor and ongoing tACS. This real-time, adaptive methodology permits the stimulation parameters to be continuously refined to match the phase of the tremor, thereby enhancing the precision and effectiveness of the intervention. The stimulation initiates at the tremor's frequency, and through real-time phase matching, it adapts to accommodate any fluctuations in tremor frequency.

6.6.2 Closed-loop Framework and Device

Based on the experimental design, we outlined the workflow and drafted a process flow diagram as presented in Figure 12. The process begins with the acquisition of hand tremor signals through a triaxial accelerometer, capturing movement across the x, y, and z axes, followed by the application of the fast Fourier transform (FFT) algorithm for spectral analysis on the Euclidean norm of the tremor data from 3 axes (Cooley and Tukey, 1965). Subsequently, the stimulation process initiates as described previously, simultaneously recording signals and immediately detecting phase and frequency, integrating the identified signal characteristics plus a rapid online detection algorithm to generate phase- and frequency-matched tACS signals within this closed loop with 2 ms adjustment intervals. To ensure comprehensive monitoring of the process, the device is designed to produce and transmit high-quality outputs in real-time, including the raw tremor data, the analysed signal, detected phase and frequency, and the generated tACS signal through separate channels, utilizing the LabStreamingLayer (LSL) platform (A. Kothe, 2022). LSL is a multi-platform C++ shared library for data streaming with C bindings and wrappers for various programming languages such as MATLAB or Python. This setup not only facilitates online monitoring of the process but also enables the recording of all data for subsequent offline analysis.

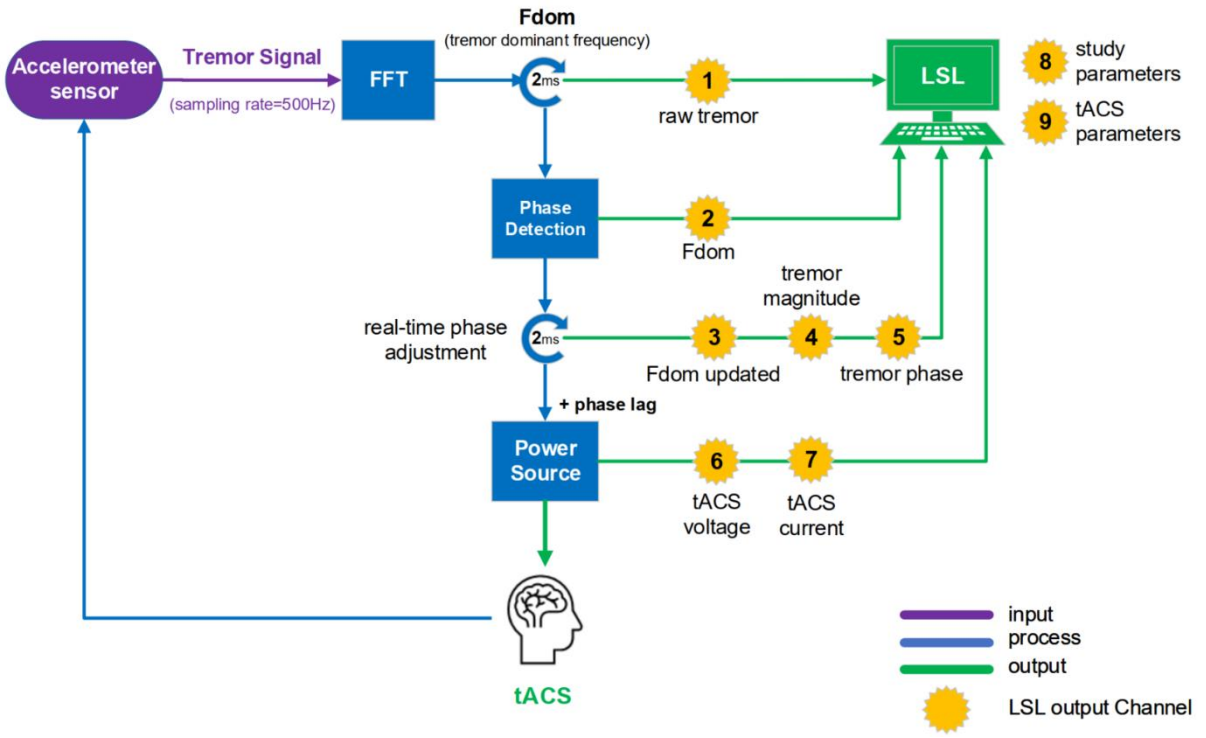

Figure 12. Process flow diagram of the closed-loop stimulation system to entrain and suppress PD tremor. This diagram outlines the sequential steps from initial hand tremor signal acquisition via an accelerometer, through spectral analysis using FFT, to the real-time generation and adjustment of phase- and frequency-matched tACS signals. The process is designed in a way to ensure accurate signal detection, analysis, and effective stimulation adjustment within a 2 ms interval.

6.6.3 Hardware and Software Development

The process framework was next implemented on the newly developed closed-loop stimulation device by neuroConn, known as LOOP-IT (neuroConn Technologies, 2022). The modular architecture of LOOP-IT facilitates flexibility in accommodating a wide array of analogue and digital input/output (I/O) modules, as illustrated in Figure 13, which allows for virtually limitless configuration combinations to suit specific experimental needs. Among the device's capabilities is the support for a variety of electrically independent modules, each offering distinct functionalities. These include the acquisition of various signals like EEG, Electrocardiography (ECG), and Electromyography (EMG) at sampling rates up to 16-kilo samples per second (ksps); transcranial electric stimulation (tES), transcranial magnetic stimulation (TMS), current sources characterized by low noise levels, multichannel digital I/O; and interfaces for evoked potential and display, ideal for feedback-driven applications (neuroConn Technologies, 2022). For the purpose of this study, a specific LOOP-IT device was developed and hardware-programmed using C/C++ and a Linux-based operating system. This custom programming and hardware adjustment were aimed at enabling the device to independently entrain and suppress PD tremor using the previously described algorithm and workflow.

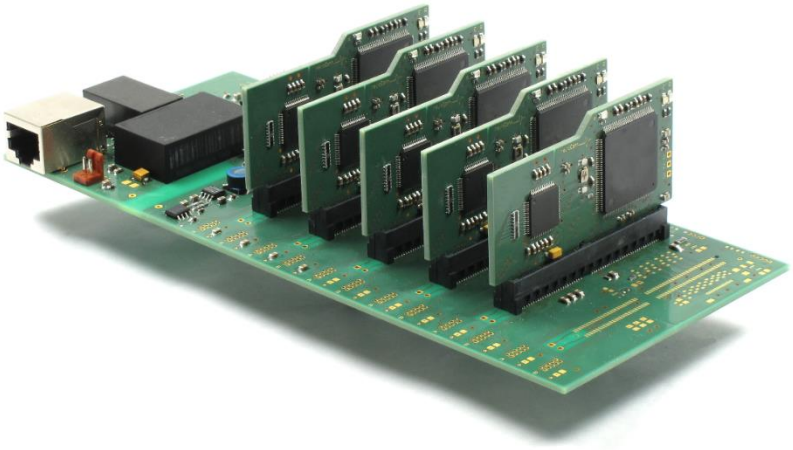

Figure 13. The modular structure of the LOOP-IT closed-loop stimulation device. This illustration showcases the versatile modular design of the LOOP-IT system, developed by neuroConn, highlighting its capacity to integrate a broad spectrum of electrically isolated analogue and digital I/O modules. The system can be customized to support a diverse range of functionalities, enabling LOOP-IT to be specifically configured for complex neuroscientific research and therapeutic applications, such as the suppression of PD tremor using tailored algorithms.

The device, as can be seen in Figure 14, operates on batteries, ensuring independence from the city's electrical grid to guarantee both low voltage levels and full operational control. Furthermore, using batteries detaches LOOP-IT from the 50Hz line noise and enhances signal quality. The battery pack utilizes batteries capable of being charged in three phases with a constant initial current of ~2A. The data input i.e. hand tremor signal, is through the triaxial accelerometer, while the output interfaces through bi-channel electrode sockets compatible with standard tACS electrodes. These sockets can connect to conventional sponge electrodes from neuroConn, facilitating optimal electrode placement as identified by Sadeghi et al. (2022b). In addition to the stimulation output cables, a LAN cable links the device to a computer with MATLAB, on which LSL-related libraries are installed and through the function '*vis_stream'* the incoming data streaming is visible and recordable in high quality. This connection serves solely as a one-directional information and data transfer path from the device to the researcher, without offering any means to alter or influence the device's function remotely.

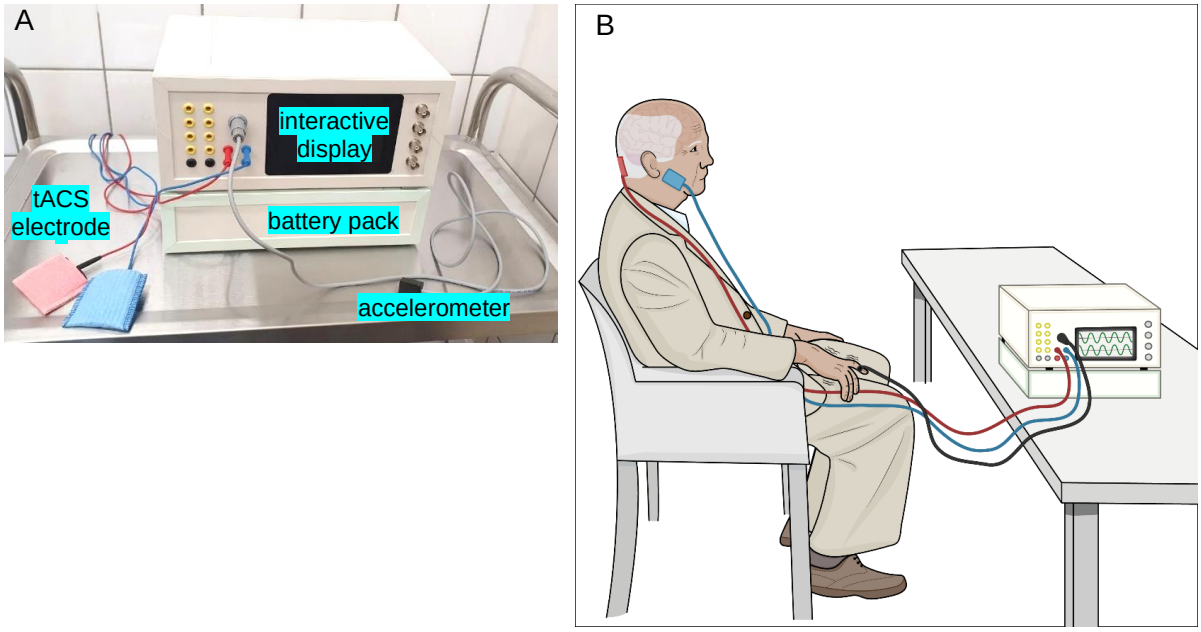

Figure 14. LOOP-IT device. A) the completed LOOP-IT device, showcasing its main components: the main device, the battery pack, ensuring that the device operates independently of external power sources, a triaxial accelerometer for accurate motion and tremor detection; and tACS electrodes for delivering the stimulation. **B)** schematic representation of the experimental setup using LOOP-IT to record and deliver phased-adjusted tACS to entrain and suppress the tremor of a PD patient. Illustration by Maria Carlos Oliveira (2023).

The device is equipped with a compact computing unit and an integrated touch display, enabling users to conveniently input experiment-specific parameters at the start of each session. These parameters include a numerical subject identification code for anonymity, session and run identifiers, stimulation duration in seconds, and a restricted stimulation amplitude range of 2-4 mA peak to peak. Additionally, it allows for the adjustment of phase lag settings by the user and provides straightforward start and stop controls for seamless device operation management. Given that the device's analysis, along with the subsequent delivery and modulation of the tACS signal, relies heavily on the characteristics of the incoming tremor signal, significant attention has been devoted to the precision and safety of the tremor recording sensor. Therefore, a standard and commercially available triaxial accelerometer was used and further equipped with an embedded hardware frequency filter tailored for PD tremor to ensure rapid, high-fidelity tremor signal capture and transmission at an adequate sampling rate, within the specified frequency range, and free of noise interference.

Upon commencing a session, once the accelerometer and tACS electrodes are connected, the device autonomously verifies safety criteria, detects the tremor signal, and prepares to operate in one of two modes: either exclusively recording for tremor characteristic analysis or executing closed-loop stimulation through concurrent recording and phase-adjusted tACS at 2 ms intervals. The device outputs data is streamed through 9 separate LSL channels as planned, including raw tremor signal, computed dominant frequency, adjusted dominant frequency (average), tremor magnitude, tremor phase, tACS current (mA), tACS voltage (µV), study information (patient ID, run, session), and tACS information (phase lag, sham, uncoupled).

6.6.4 Device Safety

Safety was paramount throughout the development and implementation of this closed-loop device, given its autonomous capabilities to detect tremor, analyse the signal, and then generate and apply a tACS signal based on these analyses. From the initial design phase to the final stages of development and testing, meticulous attention was devoted to ensuring maximal safety and minimal risk associated with its use.

Key to this approach was securing ethical approval for the entire experimental process including tremor recording, analysis, and closed-loop stimulation with a 2-4mA peak-to-peak tACS. To establish a reliable voltage control system and minimize electrical risks, the device operates on battery power alone, disconnected from the municipal power supply. Electrical isolation was implemented in the device to ensure that patients with attached electrodes were safely isolated from the device's power source. Additionally, the hardware developers at neuroConn incorporated voltage control measures into the device's circuitry.

Safety measures further involved the implementation of hardware-level bandpass filters directly in the accelerometer sensor, confining signal recording to the tremor frequency range of 4-6 Hz to prevent the generation of tACS signals outside this spectrum. During the stimulation phase, controlling the impedance level at the electrode-skin interface is critical. Therefore, an algorithm was embedded to continuously measure impedance levels throughout stimulation, to automatically discontinue stimulation if impedance exceeds 10KΩ, and to visually indicate impedance levels via a colour-coded light button on LOOP-IT display screen (green for 0-5KΩ, yellow for 5-10KΩ, and red for ≥10KΩ). Additionally, to ensure the tACS signal remains relatively stationary no matter the conditions, an algorithm constantly controls the generated signal's magnitude, ceasing stimulation if unusual activity is detected (with a ramp-down to avoid sudden changes in output voltage), such as excessive currents beyond the set range of 2-4mA or a sudden drop to near zero amplitude.

6.6.5 Device Performance

During the hardware programming phase, each function was rigorously tested across multiple stages. After completing the hardware development and programming, we conducted comprehensive testing using a variety of inputs. This included tremor simulations with a custom tremor machine and tests involving two participants who mimicked hand movements replicating actual tremor patterns recorded from a PD patient with severe hand tremor. These tests also explored different stimulation parameters to assess the device's overall performance and the accuracy and quality of each specific output in MATLAB. For instance, the tremor's dominant frequency was measured offline using FFT by plotting the power spectrum and identifying the peak within the PD tremor frequency range. This measurement was then compared to the device's calculations.

A critical aspect of testing focused on the accuracy of phase adjustment, namely, the device's ability to align its tACS signal with the real-time tremor signal. This involved offline analysis of both the raw tremor and the generated tACS signals. First, a 4th-degree bandpass Butterworth filter was applied within the PD tremor frequency band (4-6 Hz), followed by conducting a Hilbert transform and extracting the instantaneous phase and frequency profiles of both signals. The synchronisation quality between the

tACS and tremor signals was evaluated by computing the Phase Locking Value (PLV), (Hülsemann et al., 2019; Lachaux et al., 1999) as given by [21].

$$PLV = \left| \frac{\sum_{t=1}^{n} e^{i(\theta_{tremor,t} - \theta_{tACS,t})}}{n} \right| \qquad [21]$$

Where θ_{tremor} represents the tremor signal, θ_{tACS} the LOOP-IT tACS signal, n denotes the total number of data points, t represents a specific data point, and $e^{i(\theta_{tremor,t} - \theta_{tACS,t})}$ is the complex exponential of the phase difference between the tremor and tACS signals at each data point, providing a measure of their phase synchronisation. In the final analysis, one-sample t-tests were conducted to assess if the observed phase differences fell within an acceptable deviation from the predetermined phase lag. The resulting p-values were compared against a significance threshold of 0.05 to determine statistical significance.

6.7 Results

Figure 15 showcases LOOP-IT performance in aligning the participant's detected hand tremor signal and the generated and adjusted tACS signal. Polar histograms are plotted for two distinct conditions: the phase lag set at 0° and 120°. Across each scenario, five repeated runs were conducted and assessed. In both configurations, a success rate above 80% (4 out of 5 runs) is observable, with notably high PLV values (mean = 96.96%, SD = 0.45% for 0° phase lag, and mean = 80.08%, SD = 33.31% for 120° phase lag). T-test outcomes further demonstrate significant compliance with the predetermined phase lag, revealing that the phase of the generated tACS does not significantly deviate from the tremor phase (p = 0.99 for 0° phase lag, p = 0.25 for 120° phase lag).

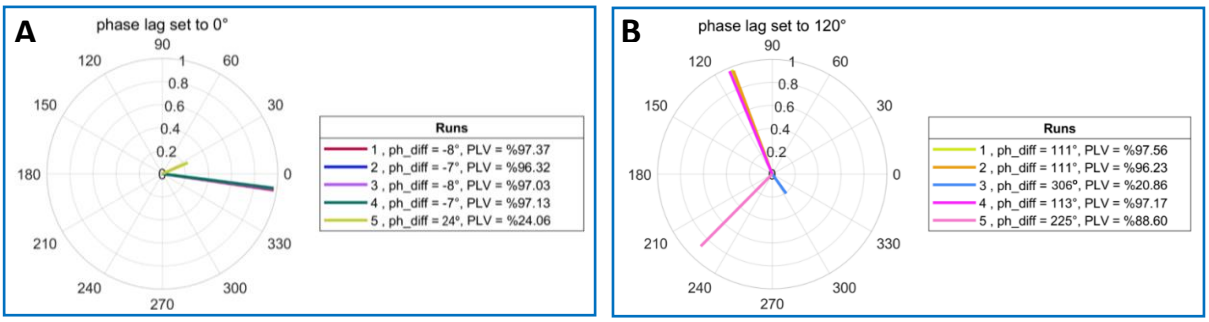

Figure 15. Performance of the developed LOOP-IT device in terms of phase adjustment and synchronisation. Polar plots of two conditions where the device was used to entrain and suppress simulated PD tremor with set phase lags of 0° and 120° (panels A and B respectively). For each condition, 5 repetitive runs were conducted. The orientation of each line within the plot corresponds to the phase difference observed in each run (relative to the intended phase lag of 0° or 120°), while the length of the line indicates the magnitude of the corresponding PLV, reflecting the synchronisation strength between the simulated tremor and the tACS signal. The results indicate the device's capability to adjust and synchronise with the simulated tremor, as evidenced by the distribution and length of lines within each polar histogram.

6.8 Discussion

The design and operational strategy of LOOP-IT, which includes real-time phase matching closed-loop tACS and possesses the ability to suppress PD tremor, presents a contribution to personalized therapies in neurological disorders. The significance of such a device lies not only in its technical innovation but also in its adaptation to intermittent uncommon behaviours of PD tremor among PD patients or even within the same patient over time (Di Biase et al., 2017). By providing a means to dynamically adjust to the tremor's characteristics, the development of this device offers a more effective and patient-specific therapeutic option compared to the conventional open-loop tACS paradigms.

Quality and safety were considered a high priority during the development process of LOOP-IT. Findings from rigorous testing procedures revealed that the device meets all necessary standards for systematic performance and safety. As a result of the development and testing phase, LOOP-IT is now ready for pilot testing on patients, a vital step for assessing the practical impact of the device on tremor suppression in real-world settings. However, the pilot testing phase and its outcomes fall outside the scope of this thesis. The deployment of LOOP-IT in clinical settings heralds a promising advance in PD tremor management, highlighting the importance of innovation and patient-centred design in addressing the intricate challenges of neurological conditions.

Chapter 7 : Conclusion and Outlook

In this thesis, findings from a multimodal investigation of PD tremor are reported, through a series of interconnected studies that span structural analyses, network dynamics, and the development of therapeutic interventions.

First, we focused on the structural changes in the cerebellum associated with PD tremor. Our findings indicate that there is a significant correlation between the severity of PD tremor and the volume of lobule VIIb, a sub-region of the cerebellum involved in hand movement. This suggests a potential cerebellar biomarker in PD tremor, enhancing our understanding of the cerebellar morphological mapping of tremor-associated regions and networks.

On the functional and dynamical levels, we observed that PD disrupts the brain's equilibrium across multiple spatial scales. The dynamics of the CTC network are notably affected, and the cerebellum's influence within the brain's hierarchical organization increases in the disease state. These findings clarify more how the cerebellum and CTC are involved in the pathology of PD.

Building on the insights from structural and dynamical analyses, we explored non-invasive cerebellar stimulation paradigms to reduce tremor amplitude. First, we optimized cerebellar tACS strategies to ensure effective and safe modulation of cerebellar activity. Next, to fully use the potential of tACS to entrain and modulate intrinsic brain oscillations, in a collaborative effort, we designed and developed a device capable of performing closed-loop, phase-adjusted cerebellar tACS. This innovative device is specifically engineered to entrain and reduce PD tremor by responding dynamically to ongoing tremor oscillations.

To address each research question with high validity and reproducibility, the two critical aspects of translational neuroscience, the methodology used in this thesis was carefully selected. We employed a combination of MRI and computational modelling based on their established reliability and effectiveness. The MRI-based techniques, including anatomical, tractography, and functional assessments were chosen because they provide comprehensive insights into brain structure and function, essential for understanding PD tremor. Additionally, we defined the MRI sequences and scanning parameters in a way to be feasible in most clinical settings today, enhancing the translatability and applicability of our findings. Computational modelling was integrated directly with the MRI data, an approach that significantly enhances the accuracy of simulations. This method allows us to create detailed and predictive models of brain dynamics, offering a powerful tool for exploring underlying pathological mechanisms and hypothesizing the effects of potential interventions on PD tremor. By combining these advanced methodologies, we ensured that the research was not only grounded in empirical findings but also poised for practical application and replication in clinical contexts.

The limitations of the works associated with this thesis primarily stem from the limited sample sizes of PD patients specifically exhibiting tremor, a common challenge in clinical settings. This restriction reduces the generalizability of the findings and also hinders our ability to perform classification analyses between healthy/PD or PD with/without tremor using results from the computational models. Additionally, the absence of a longitudinal investigation to track these findings over time further limits our understanding of their long-term implications and stability.

The sequential exploration from structural analyses to the development of a therapeutic device contributes to both understanding and treating PD tremor. The structural alterations in the cerebellum provide a clear target for intervention, while the altered dynamics of the CTC network underscore the complexity of PD's impact on brain function. The development of a targeted stimulation device based on these findings represents a significant advancement in personalized, technology-driven therapies to manage PD tremor.

Future research should focus on recruiting larger sample sizes to enhance the generalizability of findings across various types of tremor, not just those associated with PD, especially over the long term. Investigating the impact of dopamine or dopamine responsiveness on tremor dynamics would also be insightful. Finally, conducting clinical trials using the developed closed-loop device on PD patients with significant tremor could validate its effectiveness and confirm its potential as a non-invasive therapeutic alternative to reduce PD tremor in clinical settings.

Annexe

Supplementary Materials to Chapter 4: Alterations of the Cerebellar Structure in PD Tremor

Descriptive Information on Cerebellar Volumes

In our study examining the relationship between cerebellar volumes and tremor severity in PD, we extended our analyses to include detailed assessments of individual cerebellar regions. Table S1 presents comprehensive descriptive statistics for the volumes of various cerebellar lobules, namely lobules I through X, Crus I, and Crus II, which were extracted using the CERES pipeline.

Table S1. descriptive statistics of cerebellar volumes

Cerebellar region	Mean volume (cm^3)	SD	Median [Min, Max] (cm^3)
Cerebellum	136.82	15.59	135.85 [107.63, 185.46]
Lobule I-II	0.10	0.04	0.09 [0.04, 0.28]
Lobule III	1.43	0.29	1.40 [0.88, 2.28]
Lobule IV	4.54	0.71	4.50 [2.50, 6.34]
Lobule V	7.86	1.12	7.68 [6.13, 11.34]
Lobule VI	17.89	3.38	17.89 [1.60, 26.61]
Crus I	28.41	5.22	27.40 [19.33, 42.83]
Crus II	17.58	2.99	17.24 [12.04, 24.40]
Lobule VIIb	9.21	1.32	9.04 [6.86, 12.48]
Lobule VIIIa	13.54	1.95	13.62 [9.88, 16.95]
Lobule VIIIb	9.60	1.77	9.47 [6.31, 14.43]
Lobule IX	7.86	1.50	7.74 [4.47, 11.71]
Lobule X	1.58	0.28	1.55 [1.08, 2.36]

***SD**: standard deviation*

Association of Cerebellar Volumes with BR and PIGD Scores

Apart from the tremor severity, we also investigated the associations between cerebellar volumes and bradykinesia-rigidity (BR) and postural instability and gait disorders (PIGD) using linear regression models. The results are presented in Table S2 and Table S3. Although our findings did not reveal any statistically significant correlations (all p-values > 0.05), the table provides the beta coefficients along with 95% confidence intervals (CI) for each cerebellar region studied.

Table S2. Association between cerebellar volumes and BR scores in PD

Cerebellar Region	Beta coefficient (95% CI)	P-value
Cerebellum	0.07	0.526
Lobule I-II	-16.37	0.520
Lobule III	2.75	0.499
Lobule IV	1.34	0.443
Lobule V	-0.81	0.454
Lobule VI	-0.17	0.660
Crus I	0.38	0.167
Crus II	0.31	0.459
Lobule VIIb	0.04	0.967
Lobule VIIIa	0.29	0.656
Lobule VIIIb	0.52	0.514
Lobule IX	-0.50	0.573
Lobule X	1.21	0.789

* *p-value significant after LOOA analysis as well as FDR correction.* BR score has been extracted from MDS-UPDRS part III (items 3.3, 3.4, 3.5, 3.6, 3.7, and 3.8). Results of multiple linear regression models are presented and the primary outcome is demonstrated using the beta coefficient. The confidence interval is considered 95%. No significant association was found between cerebellar lobule volumes and BR score. Results are adjusted for age, sex, disease duration, and ICV. **BR:** bradykinesia-rigidity; **ICV:** intracranial volume; **LOOA:** leave-one-out analysis; **MDS-UPDRS:** Movement Disorder Society-Sponsored Revision of the Unified Parkinson's Disease Rating Scale

Table S3. Association between cerebellar volumes and PIGD scores in PD

Cerebellar Region	Beta coefficient (95% CI)	P-value
Cerebellum	0.01	0.862
Lobule I-II	-4.36	0.738
Lobule III	1.72	0.410
Lobule IV	0.63	0.478
Lobule V	-0.66	0.231
Lobule VI	-0.28	0.146
Crus I	0.11	0.434
Crus II	0.24	0.274
Lobule VIIb	0.46	0.325
Lobule VIIIa	-0.29	0.388
Lobule VIIIb	-0.09	0.823
Lobule IX	-0.48	0.295
Lobule X	3.50	0.127

* *p-value significant after LOOA analysis as well as FDR correction.* PIGD score has been extracted from MDS-UPDRS parts II and III (items 2.12, 2.13, 3.10, 3.11, 3.12). Results of multiple linear regression models are presented and the primary outcome is demonstrated using the beta coefficient. The confidence interval is considered 95%. No significant association was found between cerebellar lobule volumes and PIGD score. Results are adjusted for age, sex, disease duration, and ICV. **PIGD:** postural instability and gait disorders; **LOOA**: leave-one-out analysis**; FDR:** false discovery rate**; ICV:** intracranial volume; **MDS-UPDRS:** Movement Disorder Society-Sponsored Revision of the Unified Parkinson's Disease Rating Scale

Association of Cerebellar Volumes with Distinct Tremor Types

We investigated the associations between various types of tremors and cerebellar volumes by conducting post-hoc regression analyses separately for postural, kinetic, and rest tremor severities. Table S4, Table S5**Table S5**, and Table S6 represent the results respectively. The only significant finding from our analyses was a negative correlation between the severity of kinetic tremor and the volume of cerebellar lobule VIIb (Table S5, p = 0.002). Other types of tremors, including postural and rest tremors, did not demonstrate significant associations with cerebellar volumes.

Table S4. Association between cerebellar volumes and postural tremor scores

Cerebellar Region	Beta coefficient (95% CI)	P-value
Cerebellum	-0.01	0.158
Lobule I-II	-1.73	0.038
Lobule III	-0.25	0.063
Lobule IV	0.00	0.981
Lobule V	-0.02	0.526
Lobule VI	0.01	0.637
Crus I	0.00	0.591
Crus II	-0.03	0.015
Lobule VIIb	-0.08	0.005
Lobule VIIIa	-0.02	0.275
Lobule VIIIb	-0.02	0.437
Lobule IX	-0.04	0.128
Lobule X	-0.27	0.067

** p-value significant after LOOA analysis as well as FDR correction.* Postural tremor scores have been extracted from MDS-UPDRS part III item 3.15. The outcome of the linear regression models is reported as the beta coefficient. The confidence interval is considered 95%. Results are adjusted for age, sex, and ICV. **LOOA:** leave-one-out analysis**; FDR:** false discovery rate**; ICV:** intracranial volume; **MDS-UPDRS:** Movement Disorder Society-Sponsored Revision of the Unified Parkinson's Disease Rating Scale

Table S5. Association between cerebellar volumes and kinetic tremor scores

Cerebellar Region	Beta coefficient (95% CI)	P-value
Cerebellum	-0.01	0.006
Lobule I-II	0.06	0.941
Lobule III	-0.12	0.369
Lobule IV	-0.09	0.095
Lobule V	-0.05	0.148
Lobule VI	-0.02	0.188
Crus I	-0.01	0.363
Crus II	-0.04	0.005
Lobule VIIb	**-0.09**	**0.002**
Lobule VIIIa	-0.04	0.090
Lobule VIIIb	-0.02	0.421
Lobule IX	-0.02	0.418
Lobule X	-0.22	0.139

** p-value significant after LOOA analysis as well as FDR correction.* Kinetic tremor scores have been extracted from MDS-UPDRS part III item 3.16. The outcome of the linear regression models is reported as the beta coefficient. The confidence interval is considered 95%. Results are adjusted for age, sex, and ICV. **LOOA**: leave-one-out analysis; **FDR**: false discovery rate; **ICV**: intracranial volume; **MDS-UPDRS:** Movement Disorder Society-Sponsored Revision of the Unified Parkinson's Disease Rating Scale

Table S6. Association between cerebellar volumes and rest tremor scores

Cerebellar Region	Beta coefficient (95% CI)	P-value
Cerebellum	0.00	0.877
Lobule I-II	-3.10	0.006
Lobule III	-0.41	0.027
Lobule IV	0.13	0.103
Lobule V	0.01	0.857
Lobule VI	0.01	0.623
Crus I	0.01	0.460
Crus II	-0.01	0.789
Lobule VIIb	-0.06	0.145
Lobule VIIIa	0.01	0.800
Lobule VIIIb	0.01	0.722
Lobule IX	0.02	0.573
Lobule X	0.15	0.468

** p-value significant after LOOA analysis as well as FDR correction.* Rest tremor scores have been extracted from MDS-UPDRS part III items 3.17 plus 3.18. The outcome of the linear regression models is reported as the beta coefficient. The confidence interval is considered 95%. Results are adjusted for age, sex, and ICV. **LOOA:** leave-one-out analysis**; FDR:** false discovery rate**; ICV:** intracranial volume; **MDS-UPDRS:** Movement Disorder Society-Sponsored Revision of the Unified Parkinson's Disease Rating Scale

Association of Cerebellar Volumes with Tremor in Upper Extremities

According to MDS-UPDRS, 'tremor score' consists of not only tremor observed in the upper extremities (hands) which are reflected in test items 2.10, 3.15a-b, 3.16a-b, 3.17a-b, and 3.18, but also lower extremities (legs) reflected in test items 3.17c and 3.17d, as well as jaw/lips tremor including score 3.17e. Consequently, the total tremor score is calculated from all these parameters. To address this point, additional analyses have been performed using the hand tremor severity only, meaning that the UPDRS leg and jaw/lips tremor scores were subtracted from the total tremor scores of each participant with PD and similar multiple linear regression models were utilized. The main results as reported in the manuscript are unchanged and reveal a significant correlation between the volume of lobule VIIb and hand tremor severity (p = 0.005) as can be viewed in Table S7.

Table S7. Association between cerebellar volumes and tremor scores of upper extremities

Cerebellar Region	Beta coefficient (95% CI)	P-value
Cerebellum	-0.01	0.227
Lobule I-II	-2.75	0.021
Lobule III	-0.36	0.059
Lobule IV	0.06	0.448
Lobule V	-0.02	0.685
Lobule VI	<0.01	0.828
Crus I	0.01	0.550
Crus II	-0.03	0.113
Lobule VIIb	**-0.12**	**0.005***
Lobule VIIIa	-0.04	0.191
Lobule VIIIb	-0.03	0.450
Lobule IX	-0.04	0.301
Lobule X	-0.09	0.676

** p-value significant after LOOA analysis as well as FDR correction*. The outcome of the linear regression models is reported as the beta coefficient. The confidence interval is considered 95%. Results are adjusted for age, sex, and ICV. **LOOA:** leave-one-out analysis**; FDR:** false discovery rate**; ICV:** intracranial volume; **MDS-UPDRS:** Movement Disorder Society-Sponsored Revision of the Unified Parkinson's Disease Rating Scale

Supplementary Materials to Chapter 5: Distortions of the Whole Brain and CTC Equilibrium in PD

Bridging Parcellations

The MRI images were parcellated using the Lausanne 2018 atlas (Cammoun et al., 2012; Tourbier et al., 2022). In parallel, the cerebellum was segmented using the CERES pipeline (Carass et al., 2018; Romero et al., 2017) and added to the Lausanne parcellation, resulting in a combined parcellation denoted as LC. For the network-level analysis, the regions of interest listed in Table S8 were required to be marked and extracted from the LC parcellation. An issue however arises for the regions whose anatomical and functional delineations differ, and cannot be accurately extracted from the dominantly anatomical LC parcellation. including supplementary motor area, primary motor cortex, premotor Cortex, and primary somatosensory cortex. These regions of interest are defined in the automated anatomical labeling3 (AAL33) (Rolls et al., 2020) parcellation regime and have unique Brodmann codes (Brodmann, 1909). Therefore, the MRI images were in parallel parcellated with the AAL3/Brodmann atlas, then a custom-made MATLAB script (R2022b, The MathWorks, Inc.) was used to bridge the gap between the LC and AAL3/Brodmann parcellations. The algorithm loads parcellated and labelled volumes of one subject, then searches for specific AAL3/Brodmann labels in the LC parcellation and marks them. Having three sets of labels, in the analysis the most accurate label was chosen for each region of interest and used for masking and further network-based computations. Table S8 includes details of regions, which network they belong to, and their corresponding AAL3 and Brodmann labels.

Table S8. Regions of interest for network-level investigation of the arrow of time in Parkinson's disease

Region of Interest	Network	LC Label	AAL3 Label	Brodmann Label
Basal Ganglia				
Striatum	BTC	Caudate Putamen	Caudate nucleus Lenticular nucleus, Putamen	-
Globus pallidus externus (GPe)	BTC	Pallidum	Lenticular nucleus, Pallidum	-
Globus pallidus internus (GPi)	BTC			-
Subthalamic nucleus (STN)	BTC	Ventral Diencephalon(Neuromorphometrics, 2005)	-	-
Thalamus				
Ventral lateral anterior nucleus (VLa)	BTC	Ventro Latero Ventral	Ventral lateral	-
Ventral lateral posterior nucleus (VLp)	CTC	Ventro Latero Dorsal	Ventral posterolateral	-
Motor cortex				
Supplementary Motor Area (SMA)	BTC	Superiorfrontal gyrus	Supplementary motor area	BA6
Primary Motor Cortex (M1)	BTC	Precentral gyrus	Precentral gyrus	BA4
Premotor Cortex (PMC)	CTC	Superiorfrontal gyrus	Superior frontal gyrus	BA6
Primary Somatosensory Cortex (SMC)	CTC	Postcentral gyrus	Postcentral gyrus	BA1 BA2 BA3
Cerebellum	CTC	26 sub-regions (lobules, Crus, and Vermis)	26 sub-regions (lobules, Crus, and Vermis)	-

AAL: automated anatomical labelling; **BTC:** basal ganglia-thalamo-cortical network; **CTC**: cerebello-thalamo-cortical network

The Hopf Model

The Hopf model as described by Deco et al. (2017) represents the brain as a network of coupled oscillators. The local dynamics of each node are described by the normal form of a supercritical Hopf bifurcation. Each node j is described by [S1].

$$\frac{dz_j}{dt} = z\left(a_j + i\omega_j - \left|z_j^2\right|\right) + g\sum_{k=1}^{N} C_{jk}\left(z_k - z_j\right) + \eta_j \qquad [S1]$$

Where

$$z_j = \rho_j e^{i\theta_j} = x_j + iy_j \qquad [S2]$$

and η_j is additive Gaussian noise with a standard deviation of 0.02. The system has a bifurcation at $a_j = 0$, so that for $a_j < 0$ there is a stable fixed point at $z_j = 0$ and for $a_j > 0$ the dynamics exhibit limit cycle oscillations with a frequency of $\frac{\omega_j}{2\pi}$ Hz. We have used a fixed $a_j = -0.02$, and each node's intrinsic frequency ω_j is taken from the averaged peak frequency of the empirical time series of each brain region. Separating the real and imaginary parts of this equation yields:

$$\frac{\partial x_j}{\partial t} = \left[a_j - x_j^2 - y_j^2\right]x_j - \omega_j y_j + \sum_{k=1}^{N} C_{jk}\left(x_k - x_j\right) + \eta_j \qquad [S3]$$

$$\frac{\partial y_j}{\partial t} = \left[a_j - x_j^2 - y_j^2\right]y_j - \omega_j x_j + \sum_{k=1}^{N} C_{jk}\left(y_k - y_j\right) + \eta_j \qquad [S4]$$

The time series are modelled by the real variable x_j.

Linearization of the Hopf Model

Under the assumptions of small non-linearities and weak noise, the statistics of the whole system can be estimated using a linear approximation (Ponce-Alvarez and Deco, 2024). Let bold letters denote column vectors and matrices. The dynamical system can be rewritten in vector form as

$$\frac{d\boldsymbol{z}}{dt} = (\boldsymbol{a} - g\boldsymbol{S} + i\boldsymbol{\omega}) \odot \boldsymbol{z} - (\boldsymbol{z} \odot \bar{\boldsymbol{z}})\boldsymbol{z} + g\boldsymbol{C}\boldsymbol{z} + \boldsymbol{\eta} \qquad [S5]$$

where $\boldsymbol{z} = [z_1, \dots, z_N]$, $\bar{\boldsymbol{z}}$ is the complex conjugate of $\boldsymbol{z}$, $\boldsymbol{a} = [a_1, \dots, a_N]$, $\boldsymbol{\omega} = [\omega_1, \dots, \omega_N]$, $\boldsymbol{S} = [S_1, \dots, S_N]$ contains the "strength" of each node $S_i = \sum_j C_{ij}$, and $\boldsymbol{\eta} = [\eta_1, \dots, \eta_N]$ represents a vector of uncorrelated noise. The symbol $\odot$ denotes the Hadamard product.

Linear fluctuations $\delta\boldsymbol{z}$ are studied here around the fixed point $\boldsymbol{z} = \boldsymbol{0}$, which is the solution of $\frac{d\boldsymbol{z}}{dt} = 0$. We discard the higher-order terms $(\delta\boldsymbol{z} \odot \delta\bar{\boldsymbol{z}})\delta\boldsymbol{z}$ and keep only the first-order terms of $\delta\boldsymbol{z}$. Let $\delta\boldsymbol{u}$ be a 2N-dimensional vector:

$$\delta\boldsymbol{u} = (\delta\boldsymbol{x}, \delta\boldsymbol{y}) = (\delta x_1, \dots, \delta x_N, \delta y_1, \dots, \delta y_N) \qquad [S6]$$

Representing the evolution of the linear fluctuations. It follows the linear equation

$$\frac{d}{dt}\delta\boldsymbol{u} = \boldsymbol{A}\delta\boldsymbol{u} + \boldsymbol{\eta}, \qquad \text{[S7]}$$

where the $2N \times 2N$ matrix $\boldsymbol{A}$ is the Jacobian matrix of the system evaluated at the fixed point.

$$A_{jk} = \left.\frac{\partial F_j}{\partial u_k}\right|_{\mathbf{0}}, \qquad \text{[S8]}$$

where

$$F_j = \left(a_j - {x_j}^2 - {y_j}^2\right)x_j - \omega_j y_j + g\sum_{k=1}^{N} C_{jk}\left(x_k - x_j\right) \qquad \text{[S9]}$$

for $1 \le j \le N$, and

$$F_j = \left(a_j - {x_j}^2 - {y_j}^2\right)y_j + \omega_j x_j + g\sum_{k=1}^{N} C_{jk}\left(y_k - y_j\right) \qquad \text{[S10]}$$

for $N + 1 \le j \le 2N$.

The Jacobian matrix can be written as a block matrix by evaluating each of the partial derivatives:

$$\boldsymbol{A} = \begin{bmatrix} \boldsymbol{A_{xx}} & \boldsymbol{A_{xy}} \\ \boldsymbol{A_{yx}} & \boldsymbol{A_{yy}} \end{bmatrix} \qquad \text{[S11]}$$

Where $\boldsymbol{A_{xx}}$, $\boldsymbol{A_{xy}}$, $\boldsymbol{A_{yx}}$, $\boldsymbol{A_{yy}}$ are $N \times N$ matrices are given as: $\boldsymbol{A_{xx}} = \boldsymbol{A_{yy}}$ = diag$(\boldsymbol{a} - g\boldsymbol{S}) + g\boldsymbol{C}$ and $\boldsymbol{A_{xy}} = -\boldsymbol{A_{yx}}$ = diag$(\boldsymbol{\omega})$, which is a diagonal matrix whose diagonal is the vector $\boldsymbol{\omega}$.

The statistics of the linear system can be determined from the Jacobian matrix, which depends on all the parameters of the model. Given an initial condition $\delta\boldsymbol{u}(0)$ at $t = 0$, the general solution of a stochastic linear system such as equation [S6] is given by:

$$\delta\boldsymbol{u}(t) = \boldsymbol{e}^{t\boldsymbol{A}}\delta\boldsymbol{u}(0) + \int_0^t \boldsymbol{e}^{(t-s)\boldsymbol{A}} d\boldsymbol{W}(s) \qquad \text{[S12]}$$

where $d\boldsymbol{W}$ is a 2N-dimensional Wiener process, and $\boldsymbol{e}^{t\boldsymbol{A}}$ is the exponential matrix defined as:

$$\boldsymbol{e}^{t\boldsymbol{A}} = \sum_{k=0}^{\infty}\frac{1}{k!}(t\boldsymbol{A})^k = \boldsymbol{I} + t\boldsymbol{A} + \frac{1}{2!}(t\boldsymbol{A})^2 + \frac{1}{3!}(t\boldsymbol{A})^3 + \cdots, \qquad \text{[S13]}$$

where $\boldsymbol{I}$ is the identity matrix. The right-hand side of the equation is the sum of the deterministic behaviour plus a stochastic integral representing the diffusion due to noise.

The linearization is only valid if the origin $\boldsymbol{z} = \boldsymbol{0}$ is a stable solution of the system. The stability of the origin can be determined by checking that all eigenvalues of $\boldsymbol{A}$ have negative real parts. Let λ_j be the

eigenvalues of $\boldsymbol{A}$. Then, the origin is asymptotically stable if $\mathrm{Re}(\lambda_{\max}) < 0$, where $\lambda_{\max}$ is the eigenvalue with largest real part.

Network Statistics

In the following, we derive the network statistics of the linear system. The network mean activity (first-order statistic) is trivial since $\boldsymbol{z} = \boldsymbol{0}$. The first interesting statistic is the covariance of the fluctuations around the origin, i.e., $\boldsymbol{C_v} = \langle \delta \boldsymbol{u} \delta \boldsymbol{u}^{\boldsymbol{T}} \rangle$, where the superscript T denotes the transpose operator. For a stochastic linear system such as equation [S6], the motion equation of the covariance matrix $\boldsymbol{C_v}$ is given as:

$$\frac{d\boldsymbol{C_v}}{dt} = \boldsymbol{A}\boldsymbol{C_v} + \boldsymbol{C_v}\boldsymbol{A}^{\boldsymbol{T}} + \boldsymbol{Q_n}, \qquad \text{[S14]}$$

where $\boldsymbol{Q_n} = \langle \boldsymbol{\eta}\boldsymbol{\eta}^{\boldsymbol{T}} \rangle$ is the covariance matrix of the noise. For uncorrelated noise, $\boldsymbol{Q_n}$ is diagonal, i.e., $\boldsymbol{Q_n} = \sigma^2 \boldsymbol{I}$. The stationary covariance matrix can be obtained by solving $\frac{d\boldsymbol{C_v}}{dt} = 0$, which leads to the following algebraic equation:

$$\boldsymbol{A}\boldsymbol{C_v} + \boldsymbol{C_v}\boldsymbol{A}^{\boldsymbol{T}} + \boldsymbol{Q_n} = \boldsymbol{0}, \qquad \text{[S15]}$$

Equation [S15] is an algebraic Lyapunov equation that has a unique solution provided that $\boldsymbol{A}$ is asymptotically stable. The Lyapunov equation can be solved using the eigen-decomposition of the Jacobian matrix. Let $\boldsymbol{A} = \boldsymbol{V}\boldsymbol{D}\boldsymbol{V}^{-\boldsymbol{1}}$, where $\boldsymbol{D}$ is a diagonal matrix containing the eigenvalues of $\boldsymbol{A}$, denoted λ_i, and the columns of the matrix $\boldsymbol{V}$ are the eigenvectors of $\boldsymbol{A}$. Multiplying equation [S15] by $\boldsymbol{V}^{-\boldsymbol{1}}$ from the left and by the conjugate transpose of $\boldsymbol{V}^{-\boldsymbol{1}}$, noted $\boldsymbol{V}^{-\dagger}$, from the right we get:

$$\boldsymbol{C_v} = \boldsymbol{V}\boldsymbol{M}\boldsymbol{V}^{-\dagger}, \qquad \text{[S16]}$$

where the matrix $\boldsymbol{M}$ is given as: $M_{ij} = -\tilde{Q}_{ij}/(\lambda_i + \lambda_i^*)$ and $\widetilde{\boldsymbol{Q}} = \boldsymbol{V}^{-\boldsymbol{1}}\boldsymbol{Q_n}\boldsymbol{V}^{-\dagger}$. A fast, stable numerical solution of equation [S15] can be obtained using the MATLAB function *lyap.m* that uses the Bartels-Stewart method based on the Schur decomposition of the matrix $\boldsymbol{A}$ (Bartels and Stewart, 1972).

Moreover, knowledge of the Jacobian matrix and the stationary covariance gives the stationary lagged covariances of the state variables, defined as $\boldsymbol{C_v}(\tau) = \langle \delta \boldsymbol{u}(t+\tau) \delta \boldsymbol{u}(t)^{\boldsymbol{T}} \rangle$. Using the general solution of the system given by equation [S12], we get:

$$\boldsymbol{C_v}(\tau) = \boldsymbol{e}^{\tau \boldsymbol{A}} \langle \delta \boldsymbol{u}(t) \delta \boldsymbol{u}(t)^{\boldsymbol{T}} \rangle = \boldsymbol{e}^{\tau \boldsymbol{A}} \boldsymbol{C_v}(0), \qquad \text{[S17]}$$

Where $\boldsymbol{C_v}(0) = \boldsymbol{C_v}$ is the covariance matrix (i.e., zero-lag).

In summary, in the linear approximation, the stationary instantaneous and lagged covariance matrices of the model can be obtained through algebraic operations including the Jacobian matrix, also in the presence of time delays.

Variability in Trophic Hierarchy Levels

The fano factor distributions were computed and plotted to depict the variability of trophic hierarchy indices across different brain regions. First, the trophic hierarchy levels for each brain region were calculated as described in the methods. Subsequently, the fano factor, representing the variance of trophic hierarchy indices normalized by the corresponding mean, was computed separately for healthy controls and Parkinson's disease patients. These fano factors were plotted as line graphs with markers for both cohorts, providing a visual representation of the variability in trophic hierarchy indices across brain regions for each group. Additionally, a boxplot was added to illustrate the distribution of trophic hierarchy levels for different brain regions, refer to Figure S1.

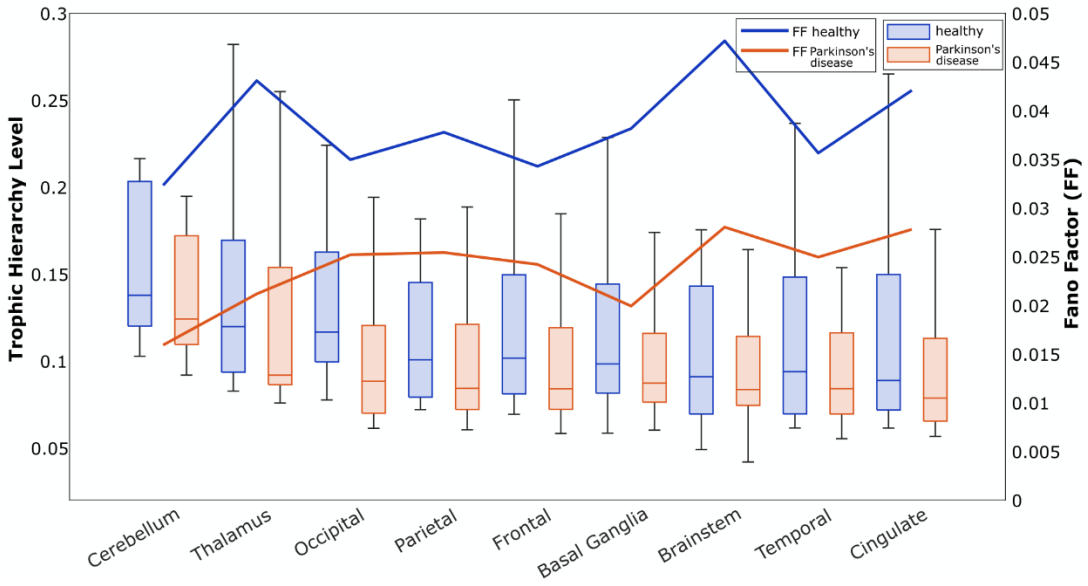

Figure S1. Boxplot and fano factor showing the variability of trophic hierarchy indices in each brain region. Fano factor was computed as the variance of hierarchy indices normalized by the corresponding mean. Higher variance and fano factors are visible in the healthy state. A complementary analysis of trophic hierarchy after the exclusion of outliers was performed and revealed the same results, thus confirming that the range of variance as demonstrated in this figure is within an acceptable criteria for the performed analyses.

Centrality Measures in the Effective Connectivity Graph

To study the importance of each parcellated region in the grand scheme of effective connectivity profiles, we followed the technique described by Mackay et al. (2020) and Ronen et al. (2014) to compute PageRank degrees of centrality for all nodes in the generative effective connectivity (GEC) directed graph and sorted the nodes based on trophic hierarchy levels as well as centrality results. In Figure S2 the whole brain GEC graph is plotted and the nodes with the highest degrees of centrality are marked, which also possess relatively high hierarchy levels. Certain cerebellar regions such as crus I, crus II, lobule VI, and lobule VIIIA possess relatively high levels in both the hierarchical organization PageRank centrality in both healthy and PD states. Several sparsely located cortical gyri also exhibit higher centrality including superior frontal and parietal gyri in PD, and the same with the inclusion of precuneus and precentral gyri in the healthy states.

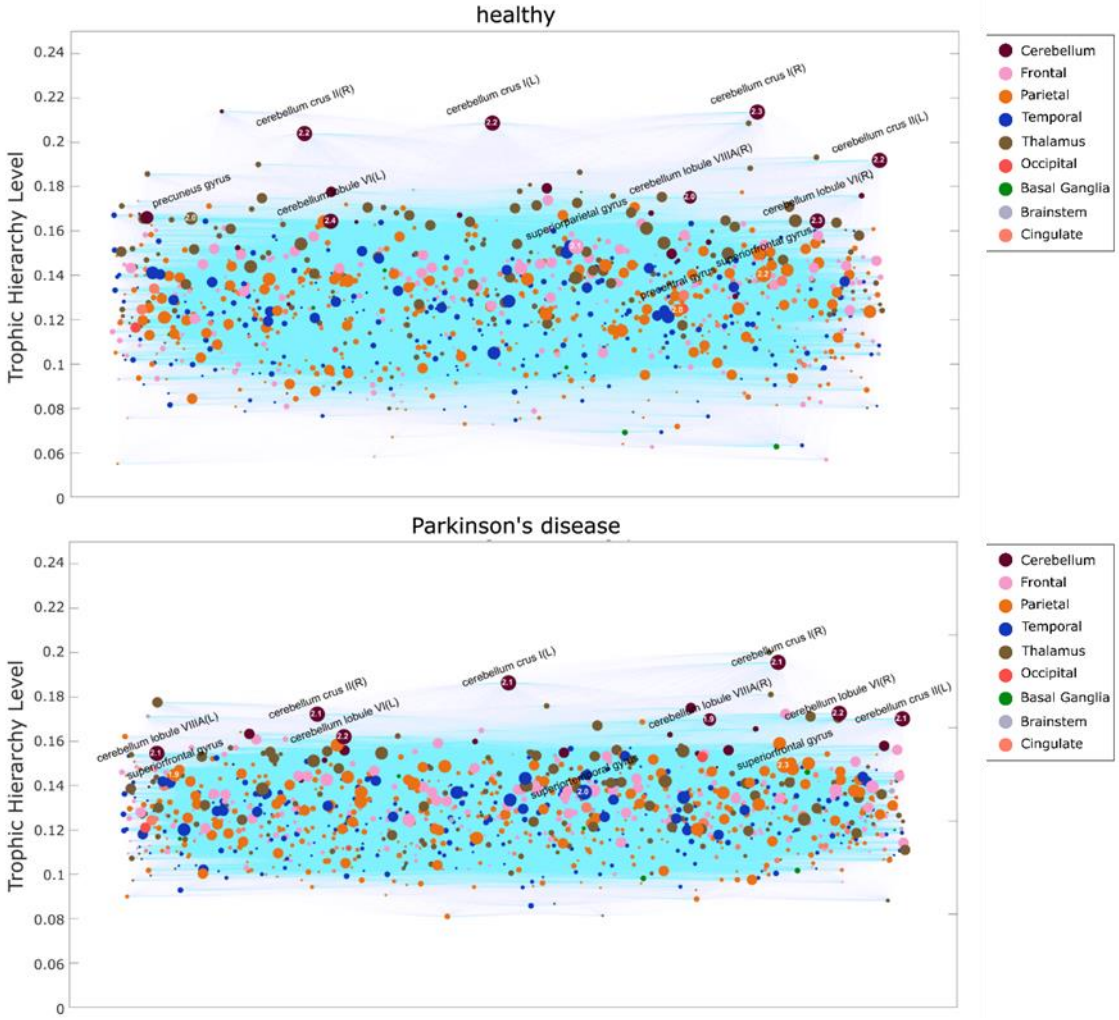

Figure S2. Hub Centrality Measures in Parkinson's disease (PD) and healthy states. PageRank centrality measures were computed in the whole-brain directed graph of generative effective connectivity (GEC) profiles with 1051 nodes representing cortical, subcortical, and cerebellar regions; in both healthy and PD states. The nodes with the top 1% with the highest centrality values were extracted and marked in the plot with their corresponding PageRank degree and region labels. Furthermore, trophic hierarchy levels have been computed and plotted on the y-axis. It can be seen that certain cerebellar regions such as crus I, crus II, lobule VI, and lobule VIIIA are relatively high in the hierarchical organization and possess higher degrees of centrality in both healthy and PD states. A number of sparsely located cortical gyri also exhibit higher influence including superior frontal and parietal gyri in PD, and the same with the inclusion of precuneus and precentral gyri in the healthy states. For the sake of visualization, the centrality measures were scaled and discretized into seven bins, and all node data points have been enlarged by a factor of 2 with the top 1% nodes further enlarged by a factor of 1.5.

Supplementary Materials to Chapter 6: Non-invasive Stimulation of the Cerebellum

Activated Cerebellar Lobules

To find out which cerebellar lobules were stimulated beyond the activation threshold (super-threshold), the mean current density (A/m) of each lobule was divided by grey matter conductivity of 0.26 S/m (Koessler et al., 2017) to get the voltage density and then compare it to the 140 V/m activation threshold as previously suggested (Neuling et al., 2012). Thresholding the flatmaps revealed activation of 7 lobules with forehead montage including Right VI, Right Crus I, Right Crus II, Right VIIb, Right VIIIa, Right VIIIb, and Right IX; 2 lobules with buccinator: Right Crus II and Right VIIb; 3 lobules with jaw: Right Crus II, Right VIIb, and Right VIIIb; and 3 lobules with neck: Right VIIb, Right VIIIa, and Right VIIIb.

Current Density in Eyeballs and Brainstem

Comprehensive descriptive statistics have been performed for current density values measured in the eyeballs and the brainstem across different stimulation montages: forehead, buccinator, jaw, and neck. For each montage, Table S9 includes the number of voxels analysed within the ROI, along with mean, standard deviation, and median values of current density expressed in amperes per meter (A/m).

Table S9. Descriptive statistics of current density (A/m) values in the eyeballs and the brainstem

	montage			
	forehead	buccinator	jaw	neck
Eyeballs				
N (number of voxels in ROI)	11096	11096	11096	11096
mean	0,32	0,06	0,05	0,03
Standard Deviation	0,07	0,03	0,02	0,00
median	0,32	0,06	0,03	0,05
Brainstem				
N (number of voxels in ROI)	23792	23792	23792	23792
mean	0,05	0,03	0,02	0,09
Standard Deviation	0,07	0,03	0,02	0,03
median	0,03	0,01	0,01	0,01

Effect of Montage and Frequency on Skin Sensations

Table S10 provides detailed statistics on the effects of different montages and frequencies on skin sensations during the tACS experiment via self-reports of the participants, as outlined in section 6.3.2.1 of the study.

Table S10. Sensation scores, phosphene scores, and phosphene areas for different montages based on participant's self-reports. Values are averaged across subjects.

Montage	**Forehead**				**Buccinator**				**Jaw**				**Neck**			
Frequency / Question	**5 Hz**	**10 Hz**	**30 Hz**	**Sham**	**5 Hz**	**10 Hz**	**30 Hz**	**Sham**	**5 Hz**	**10 Hz**	**30 Hz**	**Sham**	**5 Hz**	**10 Hz**	**30 Hz**	**Sham**
0 itching	1,57	1,57	1,29	1,14	1,43	1,57	2,29	1,00	2,00	1,71	1,71	1,00	1,71	1,86	1,57	1,00
1 warmth	1,00	1,00	1,00	1,00	1,00	1,00	1,14	1,00	1,00	1,14	1,14	1,00	1,14	1,29	1,14	1,00
2 pricking	1,71	1,86	1,43	1,00	1,71	1,57	2,00	1,00	1,71	1,86	1,71	1,00	2,00	1,86	1,57	1,00
3 pain	1,14	1,00	1,00	1,00	1,00	1,00	1,00	1,00	1,00	1,00	1,14	1,00	1,00	1,00	1,00	1,00
4 phosphene score (open)	2,14	3,57	3,57	1,00	2,00	2,57	2,86	1,00	1,43	2,14	2,43	1,00	1,14	1,43	1,14	1,00
5 phosphene score (closed)	3,00	3,86	3,43	1,00	2,14	3,00	2,14	1,00	1,57	2,14	2,14	1,00	1,00	1,00	1,14	1,00
6 phosphene area (open)	0,51	0,72	0,74	0,00	0,25	0,44	0,53	0,00	0,06	0,33	0,21	0,00	0,01	0,17	0,01	0,00
7 phosphene area (closed)	0,54	0,65	0,00	0,00	0,32	0,52	0,46	0,00	0,11	0,39	0,20	0,00	0,00	0,00	0,08	0,00

Table S11 presents the results of a two-way Scheirer Ray Hare (SRH) test, analysing the impact of montage and frequency on four specific skin sensations: itching, warmth, pricking, and pain. The table details the sum of squares (SS), degrees of freedom (df), mean squares (MS), H-statistic (H), and p-values for each factor (montage, frequency) and their interaction. The results confirm that neither the montage, the frequency of stimulation, nor the interaction between these factors, had any significant impact on the intensities of the skin sensations

Table S11. Two-way SRH test showing the effects of montage and frequency on skin sensations (itching, warmth, pricking, and pain) individually and in interaction.

	SS	***df***	***MS***	***H***	***p-value***	***sig***
Itching						
Montage	680,29	3,00		3,16	0,37	no
Frequency	3,02	1,00		0,01	0,91	no
Inter	577,20	3,00		2,68	0,44	no
Within	10576,50	48,00				
Total	11837,00	55,00	215,22			
Warmth						
Montage	280,00	3,00		3,67	0,30	no
Frequency	0,00	1,00		0,00	1,00	no
Inter	112,00	3,00		1,47	0,69	no
Within	3808,00	48,00				
Total	4200,00	55,00	76,36			
Pricking						
Montage	97,86	3,00		0,46	0,93	no
Frequency	14,00	1,00		0,07	0,80	no
Inter	731,71	3,00		3,47	0,33	no
Within	10763,93	48,00				
Total	11607,50	55,00	211,05			
Pain						
Montage	42,00	3,00		3,00	0,39	no
Frequency	14,00	1,00		1,00	0,32	no
Inter	42,00	3,00		3,00	0,39	no
Within	672,00	48,00				
Total	770,00	55,00	14,00			

Summary

Background: Parkinson's disease (PD) is characterised by motor symptoms, including tremor, which significantly impair patients' quality of life. Recent research has shifted focus to understanding the pathophysiology of tremor as a network phenomenon, specifically involving the basal ganglia-thalamo-cortical (BTC) and cerebello-thalamo-cortical (CTC) networks. It has been found that the CTC network, particularly the cerebellum, is involved in maintaining and increasing tremor amplitude.

Methods: This thesis employed a multimodal approach that integrated structural and functional magnetic resonance imaging (MRI), computational modelling, and non-invasive brain stimulation to analyse the dynamics of the cerebellum and CTC network in PD and tremor. Four sequential studies focused on morphological analyses, network dynamics, stimulation protocols, and device development.

Results: Significant changes were observed in the volume of cerebellar lobule VIIb, strongly correlating with the severity of PD tremor, suggesting its potential as a biomarker. Disruptions in brain equilibrium due to PD were noted throughout the brain and within the CTC network, accompanied by an increased influence of the cerebellum in the diseased state. These findings were complemented by optimizing the montage of cerebellar stimulation for efficiency and safety, recommending a 5x5 sponge electrode placed 2 cm lateral to the inion and a 5x7 counter electrode on the jaw. Based on these insights, a comprehensive experimental protocol for effective, closed-loop, phase-adaptive, non-invasive cerebellar transcranial alternating current stimulation (tACS) was developed. Concurrently, a novel device was designed and developed that integrates all necessary functions to achieve significant real-time alignment between tACS and tremor, ensuring both safety and efficacy.

Conclusion and Significance: The extensive multimodal study of the CTC network confirms its significant role in the tremor physiology of PD, both structurally and dynamically. The increased influence of the cerebellum on the hierarchical organization of the brain in PD underscores its suitability as a target for non-invasive brain stimulation to restore a healthy brain equilibrium. The optimized stimulation pattern and the designed closed-loop, phase-adaptive tACS device enable targeted modulation of cerebellar oscillatory activity. This thesis represents an endeavour to advance the existing knowledge on PD tremor pathophysiology and creates opportunities for personalized, non-invasive treatment strategies for this symptom.

Keywords: Parkinson's disease (PD), tremor, cerebello-thalamo-cortical (CTC) network, cerebellum, MRI-based analysis, computational modelling, non-invasive cerebellar stimulation, closed-loop and phase-adaptive tACS

Zusammenfassung

Hintergrund: Die Parkinsonerkrankung (PD) ist durch motorische Symptome gekennzeichnet, einschließlich Tremor, der die Lebensqualität der Patienten erheblich beeinträchtigt. Der Schwerpunkt der Forschung hat sich in letzter Zeit auf das Verständnis der Pathophysiologie des Tremors als Netzwerkphänomen verlagert, insbesondere im Zusammenhang mit den Basalganglien-Thalamo-Kortikalen (BTC) und Cerebello-Thalamo-Kortikalen (CTC) Netzwerken. Es wurde festgestellt, dass das CTC-Netzwerk eine entscheidende Rolle bei der Aufrechterhaltung und Verstärkung der Tremoramplitude spielt.

Methoden: In dieser Dissertation wurde ein multimodaler Ansatz verwendet, der strukturelle und funktionelle Magnetresonanztomographie (MRT), computergestützte Modellierung und nicht-invasive Hirnstimulation integriert, um die Rolle des Cerebellums und des CTC-Netzwerks bei PD und Tremor zu analysieren. Es wurden vier aufeinanderfolgende Studien durchgeführt, die sich auf morphologische Analysen, Netzwerkdynamik, Hirnstimulationsprotokolle und Geräteentwicklung konzentrierten.

Ergebnisse: Es wurden signifikante Veränderungen im Volumen des cerebellären Lobulus VIIb beobachtet, die stark mit der Schwere des PD-Tremors korrelieren und auf sein Potenzial als Biomarker hinweisen. Störungen im Gleichgewicht des Gehirns aufgrund von PD wurden im gesamten Gehirn und innerhalb des CTC-Netzwerks festgestellt, zusammen mit einem erhöhten Einfluss des Cerebellums im Krankheitszustand. Diese Ergebnisse wurden durch die Optimierung der Montage der cerebellären Hirnstimulation in Bezug auf Effizienz und Sicherheit ergänzt, indem eine 5x5 Schwammelektrode 2 cm seitlich des Inions und eine 5x7 Gegenelektrode am Kiefer platziert wurden. Basierend auf diesen Erkenntnissen wurde ein umfassendes experimentelles Protokoll für eine effektive, closed-loop, phasenadaptive, nicht-invasive cerebelläre phasenadaptive transkranielle elektrische Wechselstromstimulation (tACS) entwickelt. Parallel dazu wurde ein neuartiges Gerät entworfen und entwickelt, das alle notwendigen Funktionen integriert, um eine signifikante Echtzeit-Anpassung zwischen tACS und Tremor zu erreichen und sowohl Sicherheit als auch Effizienz zu gewährleisten.

Schlussfolgerung und Bedeutung: Die umfassende multimodale Untersuchung des CTC-Netzwerks bestätigt seine bedeutende Rolle in der Tremorphysiologie bei PD, sowohl strukturell als auch dynamisch. Der erhöhte Einfluss des Cerebellums auf die hierarchische Organisation des Gehirns bei PD unterstreicht seine Eignung als Ziel für nicht-invasive Hirnstimulation, um ein gesundes Hirngleichgewicht wiederherzustellen. Das optimierte Hirnstimulationsprotokoll und das entworfene closed-loop, phasenadaptive tACS-Gerät ermöglichen eine gezielte Modulation der cerebellären oszillatorischen Aktivität. Diese Arbeit trägt zum aktuellen Wissen über die Tremorphysiologie bei PD und zur Entwicklung neuer, personalisierter, nicht-invasiver Behandlungsstrategien für dieses Symptom bei.

Schlüsselwörter: Parkinsonerkrankung (PD), Tremor, cerebello-thalamo-kortikale (CTC)-Netzwerk, Cerebellum, MRT-basierte Analyse, computergestützte Modellierung, nicht-invasive cerebelläre Stimulation, closed-loop und phasenadaptive tACS

List of Abbreviations

AAL	Automated Anatomical Labeling
ANOVA	Analysis of Variance
BEM	Boundary Element Model
BOLD	Blood Oxygen Level Dependent
BR	Bradykinesia
BTC	Basal Ganglia-Thalamo-Cortical
CBI	cerebellum-motor cortex inhibition
CSF	Cerebrospinal Fluid
CTC	Cerebello-Thalamo-Cortical
DBS	Deep Brain Stimulation
DN	Dentate Nucleus
DTI	Diffusion Tensor Imaging
DWI	Diffusion-Weighted Imaging
ECG	Electrocardiography
EEG	Electroencephalography
E-field	Electric Field
EMG	Electromyography
eLORETA	Exact Low Resolution Brain Electromagnetic Tomography
EPI	Echo Planar Imaging
ET	Essential Tremor
FA	Fractional Anisotropy
FC	Functional Connectivity
FDR	False Discovery Rate
FDS	Finger-Dimmer-Switch
FFT	Fast Fourier Transform
FOV	Field of View
fMRI	Functional Magnetic Resonance Imaging
GEC	Generative Effective Connectivity
GPe	Globus Pallidus externus
GPi	Globus Pallidus internus
ICV	Intracranial Volume
ID	Indeterminate
I/O	Input/Output
IQR	Interquartile Range
LSL	LabStreamingLayer
LOOA	Leave One Out Analysis
M1	Primary Motor Cortex
MDS-UPDRS	Movement Disorder Society-Sponsored Revision of the Unified Parkinson's Disease Rating Scale
MEG	Magnetoencephalography
MRI	Magnetic Resonance Imaging
MPRAGE	Magnetization Prepared Rapid Gradient Echo
NIBS	Non-Invasive Brain Stimulation
PD	Parkinson's Disease
PIGD	Postural Instability and Gait Disorders
PLV	Phase Locking Value
QSM	Quantitative Susceptibility Mapping
RN	Red Nucleus
ROI	Region of Interest
rs-fMRI	Resting-state Functional MRI
SC	Structural Connectivity
SN	Substantia Nigra
SRH	Scheirer-Ray-Hare
STN	Subthalamic Nucleus
SUIT	Spatially Unbiased Infratentorial Template
SVM	Support Vector Machine
SWI	Susceptibility Weighted Imaging

tACS	Transcranial Alternating Current Stimulation
TD	Tremor Dominant
TE	Echo Time
TES	Transcranial Electrical Stimulation
TR	Repetition Time
TRN	Thalamic Reticular Nucleus
VLa	Ventrolateral Anterior
VLp	Ventrolateral Posterior
α-Syn	Alpha-Synuclein

Bibliography

1. A. Kothe, C., 2022. LabStreamingLayer Project [WWW Document]. GitHub. URL https://github.com/sccn/labstreaminglayer

2. Abdelgabar, A.R., Suttrup, J., Broersen, R., Bhandari, R., Picard, S., Keysers, C., De Zeeuw, C.I., Gazzola, V., 2019. Action perception recruits the cerebellum and is impaired in patients with spinocerebellar ataxia. Brain 142, 3791–3805. https://doi.org/10.1093/brain/awz337

3. Alexander, B., Loh, W.Y., Matthews, L.G., Murray, A.L., Adamson, C., Beare, R., Chen, J., Kelly, C.E., Anderson, P.J., Doyle, L.W., Spittle, A.J., Cheong, J.L.Y., Seal, M.L., Thompson, D.K., 2019. Desikan-Killiany-Tourville Atlas compatible version of m-CRIB neonatal parcellated whole brain atlas: The m-Crib 2.0. Front. Neurosci. 13, 34. https://doi.org/10.3389/fnins.2019.00034

4. Antal, A., Herrmann, C.S., 2016. Transcranial Alternating Current and Random Noise Stimulation: Possible Mechanisms. Neural Plast. 2016. https://doi.org/10.1155/2016/3616807

5. Antal, A., Paulus, W., 2013. Transcranial alternating current stimulation (tACS). Front. Hum. Neurosci. https://doi.org/10.3389/fnhum.2013.00317

6. Asamoah, B., Khatoun, A., Mc Laughlin, M., 2019. tACS motor system effects can be caused by transcutaneous stimulation of peripheral nerves. Nat. Commun. 10, 1–16. https://doi.org/10.1038/s41467-018-08183-w

7. Ashburner, J., Friston, K.J., 2005. Unified segmentation. NeuroImage 26, 839–851. https://doi.org/10.1016/j.neuroimage.2005.02.018

8. Avants, B., Tustison, N., Song, G., 2009. Advanced Normalization Tools (ANTS). Insight J. 1–35.

9. Barker, A.T., Jalinous, R., Freeston, I.L., 1985. Non-invasive magnetic stimulation of human motor cortex. The Lancet 325, 1106–1107. https://doi.org/10.1016/S0140-6736(85)92413-4

10. Bartels, R.H., Stewart, G.W., 1972. Algorithm 432 [C2]: Solution of the matrix equation AX + XB = C [F4]. Commun. ACM 15, 820–826. https://doi.org/10.1145/361573.361582

11. Benjamini, Y., Hochberg, Y., 1995. Controlling the False Discovery Rate : A Practical and Powerful Approach to Multiple Testing Yoav Benjamini ; Yosef Hochberg Controlling the False Discovery Rate : a Practical and Powerful Approach to Multiple Testing. Society 57, 289–300.

12. Benninger, D.H., Thees, S., Kollias, S.S., Bassetti, C.L., Waldvogel, D., 2009. Morphological differences in Parkinson's disease with and without rest tremor. J. Neurol. 256, 256–263. https://doi.org/10.1007/s00415-009-0092-2

13. Berg, D., Adler, C.H., Bloem, B.R., Chan, P., Gasser, T., Goetz, C.G., Halliday, G., Lang, A.E., Lewis, S., Li, Y., Liepelt-Scarfone, I., Litvan, I., Marek, K., Maetzler, C., Mi, T., Obeso, J., Oertel, W., Olanow, C.W., Poewe, W., Rios-Romenets, S., Schäffer, E., Seppi, K., Heim, B., Slow, E., Stern, M., Bledsoe, I.O., Deuschl, G., Postuma, R.B., 2018. Movement

disorder society criteria for clinically established early Parkinson's disease. Mov. Disord. 33, 1643–1646. https://doi.org/10.1002/mds.27431

14. Bharti, K., Suppa, A., Pietracupa, S., Upadhyay, N., Giannì, C., Leodori, G., Di Biasio, F., Modugno, N., Petsas, N., Grillea, G., Zampogna, A., Berardelli, A., Pantano, P., 2019. Abnormal Cerebellar Connectivity Patterns in Patients with Parkinson's Disease and Freezing of Gait. Cerebellum 18, 298–308. https://doi.org/10.1007/s12311-018-0988-4

15. Bhatia, K.P., Bain, P., Bajaj, N., Elble, R.J., Hallett, M., Louis, E.D., Raethjen, J., Stamelou, M., Testa, C.M., Deuschl, G., 2018. Consensus Statement on the classification of tremors. from the task force on tremor of the International Parkinson and Movement Disorder Society. Mov. Disord. 33, 75–87. https://doi.org/10.1002/mds.27121

16. Bidesi, N.S.R., Vang Andersen, I., Windhorst, A.D., Shalgunov, V., Herth, M.M., 2021. The role of neuroimaging in Parkinson's disease. J. Neurochem. 159, 660–689. https://doi.org/10.1111/jnc.15516

17. Bland, N.S., Sale, M.V., 2019. Current challenges: the ups and downs of tACS. Exp. Brain Res. 237, 3071–3088. https://doi.org/10.1007/s00221-019-05666-0

18. Bloem, B.R., Okun, M.S., Klein, C., 2021. Parkinson's disease. Lancet Lond. Engl. 397, 2284–2303. https://doi.org/10.1016/S0140-6736(21)00218-X

19. Bohnen, N.I., Kanel, P., Koeppe, R.A., Sanchez-Catasus, C.A., Frey, K.A., Scott, P., Constantine, G.M., Albin, R.L., Müller, M.L.T.M., 2021. Regional cerebral cholinergic nerve terminal integrity and cardinal motor features in Parkinson's disease. Brain Commun. 3. https://doi.org/10.1093/braincomms/fcab109

20. Boillat, Y., Bazin, P.L., van der Zwaag, W., 2020. Whole-body somatotopic maps in the cerebellum revealed with 7T fMRI. NeuroImage 211, 116624. https://doi.org/10.1016/j.neuroimage.2020.116624

21. Bolton, T.A.W., Van De Ville, D., Amico, E., Preti, M.G., Liégeois, R., 2023. The arrow-of-time in neuroimaging time series identifies causal triggers of brain function. Hum. Brain Mapp. 44, 4077–4087. https://doi.org/10.1002/hbm.26331

22. Bostan, A.C., Strick, P.L., 2010. The cerebellum and basal ganglia are interconnected. Neuropsychol. Rev. 20, 261–270. https://doi.org/10.1007/s11065-010-9143-9

23. Breakspear, M., 2017. Dynamic models of large-scale brain activity. Nat. Neurosci. 20, 340–352. https://doi.org/10.1038/nn.4497

24. Brittain, J.S., Cagnan, H., 2018. Recent Trends in the Use of Electrical Neuromodulation in Parkinson's Disease. Curr. Behav. Neurosci. Rep. 5, 170–178. https://doi.org/10.1007/s40473-018-0154-9

25. Brittain, J.S., Cagnan, H., Mehta, A.R., Saifee, T.A., Edwards, M.J., Brown, P., 2015. Distinguishing the central drive to tremor in Parkinson's disease and essential tremor. J. Neurosci. 35, 795–806. https://doi.org/10.1523/JNEUROSCI.3768-14.2015

26. Brittain, J.S., Probert-Smith, P., Aziz, T.Z., Brown, P., 2013. Tremor suppression by rhythmic transcranial current stimulation. Curr. Biol. 23, 436–440. https://doi.org/10.1016/j.cub.2013.01.068

27. Brodmann, K., 1909. Vergleichende Lokalisationslehre der Grosshirnrinde in ihren Prinzipien dargestellt auf Grund des Zellenbaues.

28. Broersma, M., Van Der Stouwe, A.M.M., Buijink, A.W.G., De Jong, B.M., Groot, P.F.C., Speelman, J.D., Tijssen, M.A.J., Van Rootselaar, A.F., Maurits, N.M., 2016. Bilateral cerebellar activation in unilaterally challenged essential tremor. NeuroImage Clin. 11, 1–9. https://doi.org/10.1016/j.nicl.2015.12.011

29. Brown, M.B., Forsythe, A.B., 1974. Robust Tests for the Equality of Variances. J. Am. Stat. Assoc. 69, 364–367. https://doi.org/10.1080/01621459.1974.10482955

30. Brunoni, A.R., Nitsche, M.A., Bolognini, N., Bikson, M., Wagner, T., Merabet, L., Edwards, D.J., Valero-Cabre, A., Rotenberg, A., Pascual-Leone, A., Ferrucci, R., Priori, A., Boggio, P.S., Fregni, F., 2012. Clinical research with transcranial direct current stimulation (tDCS): Challenges and future directions. Brain Stimulat. 5, 175–195. https://doi.org/10.1016/j.brs.2011.03.002

31. Buckner, R.L., Krienen, F.M., Castellanos, A., Diaz, J.C., Thomas Yeo, B.T., 2011. The organization of the human cerebellum estimated by intrinsic functional connectivity. J. Neurophysiol. 106, 2322–2345. https://doi.org/10.1152/jn.00339.2011

32. Button, K.S., Ioannidis, J.P.A., Mokrysz, C., Nosek, B.A., Flint, J., Robinson, E.S.J., Munafò, M.R., 2013. Power failure: Why small sample size undermines the reliability of neuroscience. Nat. Rev. Neurosci. 14, 365–376. https://doi.org/10.1038/nrn3475

33. Buzsáki, G., 2009. Rhythms of the Brain, Rhythms of the Brain. https://doi.org/10.1093/acprof:oso/9780195301069.001.0001

34. Cagnan, H., Little, S., Foltynie, T., Limousin, P., Zrinzo, L., Hariz, M., Cheeran, B., Fitzgerald, J., Green, A.L., Aziz, T., Brown, P., 2014. The nature of tremor circuits in parkinsonian and essential tremor. Brain 137, 3223–3234. https://doi.org/10.1093/brain/awu250

35. Cagnan, H., Mallet, N., Moll, C.K.E., Gulberti, A., Holt, A.B., Westphal, M., Gerloff, C., Engel, A.K., Hamel, W., Magill, P.J., Brown, P., Sharott, A., 2019. Temporal evolution of beta bursts in the parkinsonian cortical and basal ganglia network. Proc. Natl. Acad. Sci. U. S. A. 116, 16095–16104. https://doi.org/10.1073/pnas.1819975116

36. Cagnan, H., Pedrosa, D., Little, S., Pogosyan, A., Cheeran, B., Aziz, T., Green, A., Fitzgerald, J., Foltynie, T., Limousin, P., Zrinzo, L., Hariz, M., Friston, K.J., Denison, T., Brown, P., 2017. Stimulating at the right time: Phase-specific deep brain stimulation. Brain 140, 132–145. https://doi.org/10.1093/brain/aww286

37. Califf, R.M., 2018. Biomarker definitions and their applications. Exp. Biol. Med. 243, 213–221. https://doi.org/10.1177/1535370217750088

38. Caligiore, D., Helmich, R.C., Hallett, M., Moustafa, A.A., Timmermann, L., Toni, I., Baldassarre, G., 2016. Parkinson's disease as a system-level disorder. Npj Park. Dis. 2, 1–9. https://doi.org/10.1038/npjparkd.2016.25

39. Caligiore, D., Mannella, F., Baldassarre, G., 2019. Different Dopaminergic Dysfunctions Underlying Parkinsonian Akinesia and Tremor. Front. Neurosci. 13. https://doi.org/10.3389/fnins.2019.00550

40. Caligiore, D., Pezzulo, G., Baldassarre, G., Bostan, A.C., Strick, P.L., Doya, K., Helmich, R.C., Dirkx, M., Houk, J., Jörntell, H., Lago-Rodriguez, A., Galea, J.M., Miall, R.C., Popa, T., Kishore, A., Verschure, P.F.M.J., Zucca, R., Herreros, I., 2017. Consensus Paper: Towards a Systems-Level View of Cerebellar Function: the Interplay Between Cerebellum, Basal Ganglia, and Cortex. Cerebellum 16, 203–229. https://doi.org/10.1007/s12311-016-0763-3

41. Cammoun, L., Gigandet, X., Meskaldji, D., Thiran, J.P., Sporns, O., Do, K.Q., Maeder, P., Meuli, R., Hagmann, P., 2012. Mapping the human connectome at multiple scales with diffusion spectrum MRI. J. Neurosci. Methods 203, 386–397. https://doi.org/10.1016/j.jneumeth.2011.09.031

42. Carass, A., Cuzzocreo, J.L., Han, S., Hernandez-Castillo, C.R., Rasser, P.E., Ganz, M., Beliveau, V., Dolz, J., Ben Ayed, I., Desrosiers, C., Thyreau, B., Romero, J.E., Coupé, P., Manjón, J.V., Fonov, V.S., Collins, D.L., Ying, S.H., Onyike, C.U., Crocetti, D., Landman, B.A., Mostofsky, S.H., Thompson, P.M., Prince, J.L., 2018. Comparing fully automated state-of-the-art cerebellum parcellation from magnetic resonance images. NeuroImage 183, 150–172. https://doi.org/10.1016/j.neuroimage.2018.08.003

43. Carr, C.E., 1993. Processing of Temporal Information in the Brain. Annu. Rev. Inc 16, 223--43.

44. Chen, L., Daniels, S., Dvorak, R., Chu, H.-Y., 2023. Reduced Thalamic Excitation to Motor Cortical Pyramidal Tract Neurons in a Mouse Model of Parkinsonism. https://doi.org/10.1101/2022.09.24.509340

45. Choi, E.Y., Thomas Yeo, B.T., Buckner, R.L., 2012. The organization of the human striatum estimated by intrinsic functional connectivity. J. Neurophysiol. 108, 2242–2263. https://doi.org/10.1152/jn.00270.2012

46. Choong, C., Mochizuki, H., 2022. Neuropathology of α-synuclein in Parkinson's disease. Neuropathology 42, 93–103. https://doi.org/10.1111/neup.12812

47. Cilia, R., Cereda, E., Klersy, C., Canesi, M., Zecchinelli, A.L., Mariani, C.B., Tesei, S., Sacilotto, G., Meucci, N., Zini, M., Ruffmann, C., Isaias, I.U., Goldwurm, S., Pezzoli, G., 2015. Parkinson's disease beyond 20 years. J. Neurol. Neurosurg. Psychiatry 86, 849–855. https://doi.org/10.1136/jnnp-2014-308786

48. Cooley, J.W., Tukey, J.W., 1965. An Algorithm for the Machine Calculation of Complex Fourier Series. Math. Comput. 19, 297–301.

49. Cruzat, J., Herzog, R., Prado, P., Sanz-Perl, Y., Gonzalez-Gomez, R., Moguilner, S., Kringelbach, M.L., Deco, G., Tagliazucchi, E., Ibañez, A., 2023. Temporal Irreversibility of Large-Scale Brain Dynamics in Alzheimer's Disease. J. Neurosci. Off. J. Soc. Neurosci. 43, 1643–1656. https://doi.org/10.1523/JNEUROSCI.1312-22.2022

50. Darbin, O., Adams, E., Martino, A., Naritoku, L., Dees, D., Naritoku, D., 2013. Non-linear dynamics in parkinsonism. Front. Neurol. 4 DEC, 211. https://doi.org/10.3389/fneur.2013.00211

51. De, A., Bhatia, K.P., Volkmann, J., Peach, R., Schreglmann, S.R., 2023. Machine Learning in Tremor Analysis: Critique and Directions. Mov. Disord. 38, 717–731. https://doi.org/10.1002/mds.29376

52. de la Fuente, L.A., Zamberlan, F., Bocaccio, H., Kringelbach, M., Deco, G., Perl, Y.S., Pallavicini, C., Tagliazucchi, E., 2023. Temporal irreversibility of neural dynamics as a signature of consciousness. Cereb. Cortex 33, 1856–1865. https://doi.org/10.1093/cercor/bhac177

53. Deco, G., Kringelbach, M.L., 2014. Great expectations: Using whole-brain computational connectomics for understanding neuropsychiatric disorders. Neuron 84, 892–905. https://doi.org/10.1016/j.neuron.2014.08.034

54. Deco, G., Kringelbach, M.L., Jirsa, V.K., Ritter, P., 2017. The dynamics of resting fluctuations in the brain: Metastability and its dynamical cortical core. Sci. Rep. 7, 1–14. https://doi.org/10.1038/s41598-017-03073-5

55. Deco, G., Perl, Y.S., Sitt, J.D., Tagliazucchi, E., Kringelbach, M.L., 2021. Deep learning the arrow of time in brain activity: characterising brain-environment behavioural interactions in health and disease. bioRxiv 2021.07.02.450899.

56. Deco, G., Sanz Perl, Y., Bocaccio, H., Tagliazucchi, E., Kringelbach, M.L., 2022. The INSIDEOUT framework provides precise signatures of the balance of intrinsic and extrinsic dynamics in brain states. Commun. Biol. 5. https://doi.org/10.1038/s42003-022-03505-7

57. Deco, G., Sanz Perl, Y., Ponce-Alvarez, A., Tagliazucchi, E., Whybrow, P.C., Fuster, J., Kringelbach, M.L., 2023. One ring to rule them all: The unifying role of prefrontal cortex in steering task-related brain dynamics. Prog. Neurobiol. 227, 102468. https://doi.org/10.1016/j.pneurobio.2023.102468

58. Delaveau, P., Salgado-Pineda, P., Fossati, P., Witjas, T., Azulay, J.-P., Blin, O., 2010. Dopaminergic modulation of the default mode network in Parkinson's disease. Eur. Neuropsychopharmacol. 20, 784–792. https://doi.org/10.1016/j.euroneuro.2010.07.001

59. Desikan, R.S., Ségonne, F., Fischl, B., Quinn, B.T., Dickerson, B.C., Blacker, D., Buckner, R.L., Dale, A.M., Maguire, R.P., Hyman, B.T., Albert, M.S., Killiany, R.J., 2006. An automated labeling system for subdividing the human cerebral cortex on MRI scans into gyral based regions of interest. NeuroImage 31, 968–980. https://doi.org/10.1016/j.neuroimage.2006.01.021

60. Di Biase, L., Brittain, J.S., Shah, S.A., Pedrosa, D.J., Cagnan, H., Mathy, A., Chen, C.C., Martín-Rodríguez, J.F., Mir, P., Timmerman, L., Schwingenschuh, P., Bhatia, K., Di Lazzaro, V., Brown, P., 2017. Tremor stability index: A new tool for differential diagnosis in tremor syndromes. Brain 140, 1977–1986. https://doi.org/10.1093/brain/awx104

61. Diedrichsen, J., 2006. A spatially unbiased atlas template of the human cerebellum. NeuroImage 33, 127–138. https://doi.org/10.1016/j.neuroimage.2006.05.056

62. Diedrichsen, J., King, M., Hernandez-Castillo, C., Sereno, M., Ivry, R.B., 2019. Universal Transform or Multiple Functionality? Understanding the Contribution of the Human Cerebellum across Task Domains. Neuron 102, 918–928. https://doi.org/10.1016/j.neuron.2019.04.021

63. Dirkx, M.F., Bologna, M., 2022. The pathophysiology of Parkinson's disease tremor. J. Neurol. Sci. 435, 120196. https://doi.org/10.1016/j.jns.2022.120196

64. Dirkx, M.F., Den Ouden, H.E.M., Aarts, E., Timmer, M.H.M., Bloem, B.R., Toni, I., Helmich, R.C., 2017. Dopamine controls Parkinson's tremor by inhibiting the cerebellar thalamus. Brain 140, 721–734. https://doi.org/10.1093/brain/aww331

65. Dirkx, M.F., Zach, H., Van Nuland, A., Bloem, B.R., Toni, I., Helmich, R.C., 2019. Cerebral differences between dopamine-resistant and dopamine-responsive Parkinson's tremor. Brain 142, 3144–3157. https://doi.org/10.1093/brain/awz261

66. Duval, C., Daneault, J.F., Hutchison, W.D., Sadikot, A.F., 2016. A brain network model explaining tremor in Parkinson's disease. Neurobiol. Dis. 85, 49–59. https://doi.org/10.1016/j.nbd.2015.10.009

67. Dyke, J.P., Cameron, E., Hernandez, N., Dydak, U., Louis, E.D., 2017. Gray matter density loss in essential tremor: A lobule by lobule analysis of the cerebellum. Cerebellum Ataxias 4, 1–7. https://doi.org/10.1186/s40673-017-0069-3

68. Erro, R., Fasano, A., Barone, P., Bhatia, K.P., 2022. Milestones in Tremor Research: 10 Years Later. Mov. Disord. Clin. Pract. https://doi.org/10.1002/mdc3.13418

69. Evans, I.D., Palmisano, S., Loughran, S.P., Legros, A., Croft, R.J., 2019. Frequency-dependent and montage-based differences in phosphene perception thresholds via transcranial alternating current stimulation. Bioelectromagnetics 40, 365–374. https://doi.org/10.1002/bem.22209

70. Fertonani, A., Ferrari, C., Miniussi, C., 2015. What do you feel if I apply transcranial electric stimulation? Safety, sensations and secondary induced effects. Clin. Neurophysiol. 126, 2181–2188. https://doi.org/10.1016/j.clinph.2015.03.015

71. Fiene, M., Schwab, B.C., Misselhorn, J., Herrmann, C.S., Schneider, T.R., Engel, A.K., 2020. Phase-specific manipulation of rhythmic brain activity by transcranial alternating current stimulation. Brain Stimulat. 13, 1254–1262. https://doi.org/10.1016/j.brs.2020.06.008

72. Filippi, M., Sarasso, E., Agosta, F., 2019. Resting-state Functional MRI in Parkinsonian Syndromes. Mov. Disord. Clin. Pract. 6, 104–117. https://doi.org/10.1002/mdc3.12730

73. Fregni, F., 2005. Non-invasive brain stimulation for Parkinson's disease: a systematic review and meta-analysis of the literature. J. Neurol. Neurosurg. Psychiatry 76, 1614–1623. https://doi.org/10.1136/jnnp.2005.069849

74. Ganguly, J., Murgai, A., Sharma, S., Aur, D., Jog, M., 2020. Non-invasive Transcranial Electrical Stimulation in Movement Disorders. Front. Neurosci. 14. https://doi.org/10.3389/fnins.2020.00522

75. Gellersen, H.M., Guo, C.C., O'callaghan, C., Tan, R.H., Sami, S., Hornberger, M., 2017. Cerebellar atrophy in neurodegeneration - a meta-analysis. J. Neurol. Neurosurg. Psychiatry 88, 780–788. https://doi.org/10.1136/jnnp-2017-315607

76. G-guzmán, E., Perl, Y.S., Vohryzek, J., Escrichs, A., Manasova, D., Türker, B., Tagliazucchi, E., Kringelbach, M., Sitt, J.D., Deco, G., G-guzmán, E., 2023. The lack of temporal brain dynamics asymmetry as a signature of impaired consciousness states. Interface Focus 13. https://doi.org/10.1098/RSFS.2022.0086

77. Ghasemi, M., Mahloojifar, A., 2013. Disorganization of Equilibrium Directional Interactions in the Brain Motor Network of Parkinson′s disease: New Insight of Resting State Analysis Using Granger Causality and Graphical Approach. J. Med. Signals Sens. 3, 69–78. https://doi.org/10.4103/2228-7477.114377

78. Giraud, R., Ta, V.T., Papadakis, N., Manjón, J.V., Collins, D.L., Coupé, P., 2016. An Optimized PatchMatch for multi-scale and multi-feature label fusion. NeuroImage 124, 770–782. https://doi.org/10.1016/j.neuroimage.2015.07.076

79. Goetz, Christopher G, Martinez-martin, P., Stebbins, G.T., Stern, M.B., Tilley, B.C., Lang, A.E., 2008. MDS-UPDRS 1.

80. Goetz, Christopher G., Tilley, B.C., Shaftman, S.R., Stebbins, G.T., Fahn, S., Martinez-Martin, P., Poewe, W., Sampaio, C., Stern, M.B., Dodel, R., Dubois, B., Holloway, R., Jankovic, J., Kulisevsky, J., Lang, A.E., Lees, A., Leurgans, S., LeWitt, P.A., Nyenhuis, D., Olanow, C.W., Rascol, O., Schrag, A., Teresi, J.A., van Hilten, J.J., LaPelle, N., Agarwal, P., Athar, S., Bordelan, Y., Bronte-Stewart, H.M., Camicioli, R., Chou, K., Cole, W., Dalvi, A., Delgado, H., Diamond, A., Dick, J.P., Duda, J., Elble, R.J., Evans, C., Evidente, V.G., Fernandez, H.H., Fox, S., Friedman, J.H., Fross, R.D., Gallagher, D., Goetz, C.G., Hall, D., Hermanowicz, N., Hinson, V., Horn, S., Hurtig, H., Kang, U.J., Kleiner-Fisman, G., Klepitskaya, O., Kompoliti, K., Lai, E.C., Leehey, M.L., Leroi, I., Lyons, K.E., McClain, T., Metzer, S.W., Miyasaki, J., Morgan, J.C., Nance, M., Nemeth, J., Pahwa, R., Parashos, S.A., Schneider, J.S.J.S., Schrag, A., Sethi, K., Shulman, L.M., Siderowf, A., Silverdale, M., Simuni, T., Stacy, M., Stern, M.B., Stewart, R.M., Sullivan, K., Swope, D.M., Wadia, P.M., Walker, R.W., Walker, R., Weiner, W.J., Wiener, J., Wilkinson, J., Wojcieszek, J.M., Wolfrath, S., Wooten, F., Wu, A., Zesiewicz, T.A., Zweig, R.M., 2008. Movement Disorder Society-Sponsored Revision of the Unified Parkinson's Disease Rating Scale (MDS-UPDRS): Scale presentation and clinimetric testing results. Mov. Disord. 23, 2129–2170. https://doi.org/10.1002/mds.22340

81. Gomez-Tames, J., Asai, A., Mikkonen, M., Laakso, I., Tanaka, S., Uehara, S., Otaka, Y., Hirata, A., 2019. Group-level and functional-region analysis of electric-field shape during cerebellar transcranial direct current stimulation with different electrode montages. J. Neural Eng. 16, 036001. https://doi.org/10.1088/1741-2552/ab0ac5

82. Göttlich, M., Münte, T.F., Heldmann, M., Kasten, M., Hagenah, J., Krämer, U.M., 2013. Altered Resting State Brain Networks in Parkinson's Disease. PLoS ONE 8, e77336. https://doi.org/10.1371/journal.pone.0077336

83. Grover, V.P.B., Tognarelli, J.M., Crossey, M.M.E., Cox, I.J., Taylor-Robinson, S.D., McPhail, M.J.W., 2015. Magnetic Resonance Imaging: Principles and Techniques: Lessons for Clinicians. J. Clin. Exp. Hepatol. 5, 246–255. https://doi.org/10.1016/j.jceh.2015.08.001

84. Guerra, A., Colella, D., Giangrosso, M., Cannavacciuolo, A., Paparella, G., Fabbrini, G., Suppa, A., Berardelli, A., Bologna, M., 2022. Driving motor cortex oscillations modulates bradykinesia in Parkinson's disease. Brain 145, 224–236. https://doi.org/10.1093/brain/awab257

85. Gupta, D.K., Marano, M., Zweber, C., Boyd, J.T., Kuo, S.-H., 2020. Prevalence and Relationship of Rest Tremor and Action Tremor in Parkinson's Disease 10, 58. https://doi.org/10.5334/tohm.552

86. Hallett, M., 2012. Parkinson's disease tremor: Pathophysiology. Parkinsonism Relat. Disord. 18, S85–S86. https://doi.org/10.1016/s1353-8020(11)70027-x

87. He, N., Huang, P., Ling, H., Langley, J., Liu, C., Ding, B., Huang, J., Xu, H., Zhang, Y., Zhang, Z., Hu, X., Chen, S., Yan, F., 2017. Dentate nucleus iron deposition is a potential biomarker for tremor-dominant Parkinson's disease. NMR Biomed. 30, e3554. https://doi.org/10.1002/nbm.3554

88. Helfrich, R.F., Schneider, T.R., Rach, S., Trautmann-Lengsfeld, S.A., Engel, A.K., Herrmann, C.S., 2014. Entrainment of brain oscillations by transcranial alternating current stimulation. Curr. Biol. 24, 333–339. https://doi.org/10.1016/j.cub.2013.12.041

89. Helmich, R.C., 2018. The cerebral basis of Parkinsonian tremor: A network perspective. Mov. Disord. 33, 219–231. https://doi.org/10.1002/mds.27224

90. Helmich, R.C., Derikx, L.C., Bakker, M., Scheeringa, R., Bloem, B.R., Toni, I., 2010. Spatial remapping of cortico-striatal connectivity in parkinson's disease. Cereb. Cortex 20, 1175–1186. https://doi.org/10.1093/cercor/bhp178

91. Helmich, R.C., Toni, I., Deuschl, G., Bloem, B.R., 2013. The pathophysiology of essential tremor and parkinson's tremor. Curr. Neurol. Neurosci. Rep. https://doi.org/10.1007/s11910-013-0378-8

92. Helmich, R.C., Van den Berg, K.R.E., Panyakaew, P., Cho, H.J., Osterholt, T., McGurrin, P., Shamim, E.A., Popa, T., Haubenberger, D., Hallett, M., 2021. Cerebello-Cortical Control of Tremor Rhythm and Amplitude in Parkinson's Disease. Mov. Disord. 36, 1727–1729. https://doi.org/10.1002/mds.28603

93. Herrmann, C.S., Rach, S., Neuling, T., Strüber, D., 2013. Transcranial alternating current stimulation: A review of the underlying mechanisms and modulation of cognitive processes. Front. Hum. Neurosci. https://doi.org/10.3389/fnhum.2013.00279

94. Hoehn, M.M., Yahr, M.D., 1967. Parkinsonism: Onset, progression, and mortality. Neurology 17, 427–442. https://doi.org/10.1212/wnl.17.5.427

95. Hsu, G., Farahani, F., Parra, L.C., 2021. Cutaneous sensation of electrical stimulation waveforms. Brain Stimulat. 14, 693–702. https://doi.org/10.1016/j.brs.2021.04.008

96. Huguenard, J.R., McCormick, D.A., 2007. Thalamic synchrony and dynamic regulation of global forebrain oscillations. Trends Neurosci. 30, 350–356. https://doi.org/10.1016/j.tins.2007.05.007

97. Hülsemann, M.J., Naumann, E., Rasch, B., 2019. Quantification of phase-amplitude coupling in neuronal oscillations:comparison of phase-locking value, mean vector length, modulation index, and generalized-linear-modeling-cross-frequency-coupling. Front. Neurosci. 13, 573. https://doi.org/10.3389/fnins.2019.00573

98. Humphries, M.D., Obeso, J.A., Dreyer, J.K., 2018. Insights into Parkinson's disease from computational models of the basal ganglia. J. Neurol. Neurosurg. Psychiatry 89, 1181–1188. https://doi.org/10.1136/jnnp-2017-315922

99. Jernigan, T.L., Archibald, S.L., Fennema-Notestine, C., Gamst, A.C., Stout, J.C., Bonner, J., Hesselink, J.R., 2001. Effects of age on tissues and regions of the cerebrum and cerebellum. Neurobiol. Aging 22, 581–594. https://doi.org/10.1016/S0197-4580(01)00217-2

100. Kalia, L.V., Lang, A.E., 2015. Parkinson's disease. The Lancet 386, 896–912. https://doi.org/10.1016/S0140-6736(14)61393-3

101. Kanai, R., Chaieb, L., Antal, A., Walsh, V., Paulus, W., 2008. Frequency-Dependent Electrical Stimulation of the Visual Cortex. Curr. Biol. 18, 1839–1843. https://doi.org/10.1016/j.cub.2008.10.027

102. Kar, K., Krekelberg, B., 2012. Transcranial electrical stimulation over visual cortex evokes phosphenes with a retinal origin. J. Neurophysiol. 108, 2173–2178. https://doi.org/10.1152/jn.00505.2012

103. Kerestes, R., Laansma, M.A., Owens-Walton, C., Perry, A., van Heese, E.M., Al-Bachari, S., Anderson, T.J., Assogna, F., Aventurato, Í.K., van Balkom, T.D., Berendse, H.W., van den Berg, K.R.E., Betts, R., Brioschi, R., Carr, J., Cendes, F., Clark, L.R., Dalrymple-Alford, J.C., Dirkx, M.F., Druzgal, J., Durrant, H., Emsley, H.C.A., Garraux, G., Haroon, H.A., Helmich, R.C., van den Heuvel, O.A., João, R.B., Johansson, M.E., Khachatryan, S.G., Lochner, C., McMillan, C.T., Melzer, T.R., Mosley, P.E., Newman, B., Opriessnig, P., Parkes, L.M., Pellicano, C., Piras, F., Pitcher, T.L., Poston, K.L., Rango, M., Roos, A., Rummel, C., Schmidt, R., Schwingenschuh, P., Silva, L.S., Smith, V., Squarcina, L., Stein, D.J., Tavadyan, Z., Tsai, C.-C., Vecchio, D., Vriend, C., Wang, J.-J., Wiest, R., Yasuda, C.L., Young, C.B., Jahanshad, N., Thompson, P.M., van der Werf, Y.D., Harding, I.H., Study, the E.-P., 2023. Cerebellar Volume and Disease Staging in Parkinson's Disease: An ENIGMA-PD Study. Mov. Disord. 38, 2269–2281. https://doi.org/10.1002/mds.29611

104. Kim, J., Criaud, M., Cho, S.S., Díez-Cirarda, M., Mihaescu, A., Coakeley, S., Ghadery, C., Valli, M., Jacobs, M.F., Houle, S., Strafella, A.P., 2017. Abnormal intrinsic brain functional network dynamics in Parkinson's disease. Brain 140, 2955–2967. https://doi.org/10.1093/brain/awx233

105. Klaus, J., Schutter, D.J.L.G., 2021. Electrode montage-dependent intracranial variability in electric fields induced by cerebellar transcranial direct current stimulation. Sci. Rep. 11, 1–11. https://doi.org/10.1038/s41598-021-01755-9

106. Koessler, L., Colnat-Coulbois, S., Cecchin, T., Hofmanis, J., Dmochowski, J.P., Norcia, A.M., Maillard, L.G., 2017. In-vivo measurements of human brain tissue conductivity using focal electrical current injection through intracerebral multicontact electrodes. Hum. Brain Mapp. 38, 974–986. https://doi.org/10.1002/hbm.23431

107. Kovács, A., Kiss, M., Pintér, N., Szirmai, I., Kamondi, A., 2019. Characteristics of Tremor Induced by Lesions of the Cerebellum. Cerebellum 18, 705–720. https://doi.org/10.1007/s12311-019-01027-3

108. Krause, V., Wach, C., Suedmeyer, M., Ferrea, S., Schnitzler, A., Pollok, B., 2014. Cortico-muscular coupling and motor performance are modulated by 20 Hz transcranial alternating current stimulation (tACS) in Parkinson's disease. Front. Hum. Neurosci. 7. https://doi.org/10.3389/fnhum.2013.00928

109. Kringelbach, M.L., Perl, Y.S., Tagliazucchi, E., Deco, G., 2023. Toward naturalistic neuroscience: Mechanisms underlying the flattening of brain hierarchy in movie-watching compared to rest and task. Sci. Adv. 9, 1–15. https://doi.org/10.1126/sciadv.ade6049

110. Laakso, I., Hirata, A., 2013. Computational analysis shows why transcranial alternating current stimulation induces retinal phosphenes. J. Neural Eng. 10. https://doi.org/10.1088/1741-2560/10/4/046009

111. Lachaux, J.-P., Rodriguez, E., Martinerie, J., Varela, F.J., 1999. Measuring phase synchrony in brain signals. Hum. Brain Mapp. 8, 194–208. https://doi.org/10.1002/(SICI)1097-0193(1999)8:4<194::AID-HBM4>3.0.CO;2-C

112. Lewis, M.M., Galley, S., Johnson, S., Stevenson, J., Huang, X., McKeown, M.J., 2013. The role of the cerebellum in the pathophysiology of Parkinson's disease. Can. J. Neurol. Sci. J. Can. Sci. Neurol. 40, 299–306. https://doi.org/10.1017/S0317167100014232

113. Li, J. ying, Lu, Z. jiao, Suo, X. ling, Li, N. nan, Lei, D., Wang, L., Peng, J. xin, Duan, L. ren, Xi, J., Jiang, Y., Gong, Q. yong, Peng, R., 2020. Patterns of intrinsic brain activity in essential tremor with resting tremor and tremor-dominant Parkinson's disease. Brain Imaging Behav. 14, 2606–2617. https://doi.org/10.1007/s11682-019-00214-4

114. Liang, X.S., 2018. Causation and information flow with respect to relative entropy. Chaos Interdiscip. J. Nonlinear Sci. 28, 075311. https://doi.org/10.1063/1.5010253

115. Little, S., Bestmann, S., 2015. Computational neurostimulation for Parkinson's disease. Prog. Brain Res. 222, 163–190. https://doi.org/10.1016/BS.PBR.2015.09.002

116. Litvan, I., Bhatia, K.P., Burn, D.J., Goetz, C.G., Lang, A.E., McKeith, I., Quinn, N., Sethi, K.D., Shults, C., Wenning, G.K., 2003. SIC task force appraisal of clinical diagnostic criteria for parkinsonian disorders. Mov. Disord. 18, 467–486. https://doi.org/10.1002/mds.10459

117. Lopez, A.M., Trujillo, P., Hernandez, A.B., Lin, Y.C., Kang, H., Landman, B.A., Englot, D.J., Dawant, B.M., Konrad, P.E., Claassen, D.O., 2020. Structural Correlates of the Sensorimotor Cerebellum in Parkinson's Disease and Essential Tremor. Mov. Disord. 35, 1181–1188. https://doi.org/10.1002/mds.28044

118. Lorenz, R., Simmons, L.E., Monti, R.P., Arthur, J.L., Limal, S., Laakso, I., Leech, R., Violante, I.R., 2019. Efficiently searching through large tACS parameter spaces using closed-loop Bayesian optimization. Brain Stimulat. 12, 1484–1489. https://doi.org/10.1016/j.brs.2019.07.003

119. Lynn, C.W., Cornblath, E.J., Papadopoulos, L., Bertolero, M.A., Bassett, D.S., 2021. Broken detailed balance and entropy production in the human brain. Proc. Natl. Acad. Sci. 118, e2109889118. https://doi.org/10.1073/pnas.2109889118

120. Mackay, R.S., Johnson, S., Sansom, B., 2020. How directed is a directed network?: How directed is a directed network? R. Soc. Open Sci. 7. https://doi.org/10.1098/rsos.201138

121. Maclagan, L.C., Marras, C., Sewell, I.J., Wu, C.F., Butt, D.A., Tu, K., Bronskill, S.E., 2023. Trends in health service use among persons with Parkinson's disease by rurality: A population-based repeated cross-sectional study. PLOS ONE 18, e0285585. https://doi.org/10.1371/journal.pone.0285585

122. Madrid, J., Benninger, D.H., 2021. Non-invasive brain stimulation for Parkinson's disease: Clinical evidence, latest concepts and future goals: A systematic review. J. Neurosci. Methods 347, 108957. https://doi.org/10.1016/j.jneumeth.2020.108957

123. Makarious, M.B., Leonard, H.L., Vitale, D., Iwaki, H., Sargent, L., Dadu, A., Violich, I., Hutchins, E., Saffo, D., Bandres-Ciga, S., Kim, J.J., Song, Y., Maleknia, M., Bookman, M., Nojopranoto, W., Campbell, R.H., Hashemi, S.H., Botia, J.A., Carter, J.F., Craig, D.W., Van Keuren-Jensen, K., Morris, H.R., Hardy, J.A., Blauwendraat, C., Singleton, A.B., Faghri, F., Nalls, M.A., 2022. Multi-modality machine learning predicting Parkinson's disease. Npj Park. Dis. 8, 1–13. https://doi.org/10.1038/s41531-022-00288-w

124. Manjón, J., Eskildsen, S., Coupé, P., Romero, J., Collins, L., Manjón, J., Eskildsen, S., Coupé, P., Romero, J., Collins, L., Non-local, N., 2014. NICE : Non-local Intracranial Cavity

Extraction Montserrat Robles To cite this version : HAL Id : hal-01060348 NICE : Non-local Intracranial Cavity Extraction.

125. Manjón, J.V., Coupé, P., Martí-Bonmatí, L., Collins, D.L., Robles, M., 2010. Adaptive non-local means denoising of MR images with spatially varying noise levels. J. Magn. Reson. Imaging 31, 192–203. https://doi.org/10.1002/jmri.22003

126. Manto, M., Argyropoulos, G.P.D., Bocci, T., Celnik, P.A., Corben, L.A., Guidetti, M., Koch, G., Priori, A., Rothwell, J.C., Sadnicka, A., Spampinato, D., Ugawa, Y., Wessel, M.J., Ferrucci, R., 2021. Consensus Paper: Novel Directions and Next Steps of Non-invasive Brain Stimulation of the Cerebellum in Health and Disease. The Cerebellum. https://doi.org/10.1007/s12311-021-01344-6

127. Marras, C., Lang, A., 2013. Parkinson's disease subtypes: Lost in translation? J. Neurol. Neurosurg. Psychiatry 84, 409–415. https://doi.org/10.1136/jnnp-2012-303455

128. Martel, A.C., Galvan, A., 2022. Connectivity of the corticostriatal and thalamostriatal systems in normal and parkinsonian states: An update. Neurobiol. Dis. 174, 105878. https://doi.org/10.1016/j.nbd.2022.105878

129. Matthews, P.M., Jezzard, P., 2004. Functional magnetic resonance imaging. J. Neurol. Neurosurg. Psychiatry 75, 6–12.

130. Mcintyre, C.C., Foutz, T.J., 2013. Chapter 5 - Computational modeling of deep brain stimulation, in: Lozano, A.M., Hallett, M. (Eds.), Handbook of Clinical Neurology, Brain Stimulation. Elsevier, pp. 55–61. https://doi.org/10.1016/B978-0-444-53497-2.00005-X

131. Mehta, A.R., Brittain, J.S., Brown, P., 2014. The selective influence of rhythmic cortical versus cerebellar transcranial stimulation on human physiological tremor. J. Neurosci. 34, 7501–7508. https://doi.org/10.1523/JNEUROSCI.0510-14.2014

132. Mehta, A.R., Pogosyan, A., Brown, P., Brittain, J.S., 2015. Montage matters: The influence of transcranial alternating current stimulation on human physiological tremor. Brain Stimulat. 8, 260–268. https://doi.org/10.1016/j.brs.2014.11.003

133. Miall, R.C., 2022. Cerebellum: Anatomy and Function, in: Pfaff, D.W., Volkow, N.D., Rubenstein, J.L. (Eds.), Neuroscience in the 21st Century. Springer International Publishing, Cham, pp. 1563–1582. https://doi.org/10.1007/978-3-030-88832-9_38

134. Miller, D.B., O'Callaghan, J.P., 2015. Biomarkers of Parkinson's disease: Present and future. Metabolism. 64, S40–S46. https://doi.org/10.1016/j.metabol.2014.10.030

135. Miterko, L.N., Baker, K.B., Beckinghausen, J., Bradnam, L.V., Cheng, M.Y., Cooperrider, J., DeLong, M.R., Gornati, S.V., Hallett, M., Heck, D.H., Hoebeek, F.E., Kouzani, A.Z., Kuo, S.H., Louis, E.D., Machado, A., Manto, M., McCambridge, A.B., Nitsche, M.A., Taib, N.O.B., Popa, T., Tanaka, M., Timmann, D., Steinberg, G.K., Wang, E.H., Wichmann, T., Xie, T., Sillitoe, R.V., 2019. Consensus Paper: Experimental Neurostimulation of the Cerebellum. Cerebellum 18, 1064–1097. https://doi.org/10.1007/s12311-019-01041-5

136. Mitoma, H., Buffo, A., Gelfo, F., Guell, X., Fucà, E., Kakei, S., Lee, J., Manto, M., Petrosini, L., Shaikh, A.G., Schmahmann, J.D., 2020. Consensus Paper. Cerebellar Reserve: From Cerebellar Physiology to Cerebellar Disorders. Cerebellum 19, 131–153. https://doi.org/10.1007/s12311-019-01091-9

137. Moran, R.J., Mallet, N., Litvak, V., Dolan, R.J., Magill, P.J., Friston, K.J., Brown, P., 2011. Alterations in brain connectivity underlying beta oscillations in parkinsonism. PLoS Comput. Biol. 7, e1002124. https://doi.org/10.1371/journal.pcbi.1002124

138. Mure, H., Hirano, S., Tang, C.C., Isaias, I.U., Antonini, A., Ma, Y., Dhawan, V., Eidelberg, D., 2011. Parkinson's disease tremor-related metabolic network: Characterization, progression, and treatment effects. NeuroImage 54, 1244–1253. https://doi.org/10.1016/J.NEUROIMAGE.2010.09.028

139. Murphy, A.E., Eddington, A.S.S., 1928. The Nature of the Physical World, The Philosophical Review. The Macmillan company. https://doi.org/10.2307/2180099

140. Muthuraman, M., Raethjen, J., Koirala, N., Anwar, A.R., Mideksa, K.G., Elble, R., Groppa, S., Deuschl, G., 2018. Cerebello-cortical network fingerprints differ between essential, Parkinson's and mimicked tremors. Brain 141, 1770–1781. https://doi.org/10.1093/brain/awy098

141. Myers, P.S., McNeely, M.E., Koller, J.M., Earhart, G.M., Campbell, M.C., 2017. Cerebellar Volume and Executive Function in Parkinson Disease with and without Freezing of Gait. J. Park. Dis. 7, 149–157. https://doi.org/10.3233/JPD-161029

142. Naro, A., Leo, A., Russo, M., Cannavò, A., Milardi, D., Bramanti, P., Calabrò, R.S., 2016. Does Transcranial Alternating Current Stimulation Induce Cerebellum Plasticity? Feasibility, Safety and Efficacy of a Novel Electrophysiological Approach. Brain Stimulat. 9, 388–395. https://doi.org/10.1016/j.brs.2016.02.005

143. Neuling, T., Wagner, S., Wolters, C.H., Zaehle, T., Herrmann, C.S., 2012. Finite-element model predicts current density distribution for clinical applications of tDCS and tACS. Front. Psychiatry 3, 1–10. https://doi.org/10.3389/fpsyt.2012.00083

144. neuroConn Technologies, 2022. LOOP-IT [WWW Document]. LOOP-IT NeuroConn Technol. --One Solut. Sets New Stand. Neurosci. Lab Equip. URL https://www.neurocaregroup.com/de/technologie/loop-it

145. Neuromorphometrics, 2005. Segmentation: Ventral Diencephalon [WWW Document]. URL http://neuromorphometrics.com/Seg/html/segmentation/ventral diencephalon.html

146. Nolte, G., Dassios, G., 2005. Analytic expansion of the EEG lead field for realistic volume conductors. Phys. Med. Biol. 50, 3807–3823. https://doi.org/10.1088/0031-9155/50/16/010

147. Obeso, J.A., Rodríguez-Oroz, M.C., Benitez-Temino, B., Blesa, F.J., Guridi, J., Marin, C., Rodriguez, M., 2008. Functional organization of the basal ganglia: Therapeutic implications for Parkinson's disease. Mov. Disord. 23, S548–S559. https://doi.org/10.1002/MDS.22062

148. O'Callaghan, C., Hornberger, M., Balsters, J.H., Halliday, G.M., Lewis, S.J.G., Shine, J.M., 2016. Cerebellar atrophy in Parkinson's disease and its implication for network connectivity. Brain 139, 845–855. https://doi.org/10.1093/brain/awv399

149. Parazzini, M., Rossi, E., Ferrucci, R., Liorni, I., Priori, A., Ravazzani, P., 2014. Modelling the electric field and the current density generated by cerebellar transcranial DC stimulation in humans. Clin. Neurophysiol. 125, 577–584. https://doi.org/10.1016/j.clinph.2013.09.039

150. Paré, D., Curro'Dossi, R., Steriade, M., 1990. Neuronal basis of the parkinsonian resting tremor: A hypothesis and its implications for treatment. Neuroscience 35, 217–226. https://doi.org/10.1016/0306-4522(90)90077-H

151. Park, M.T.M., Pipitone, J., Baer, L.H., Winterburn, J.L., Shah, Y., Chavez, S., Schira, M.M., Lobaugh, N.J., Lerch, J.P., Voineskos, A.N., Chakravarty, M.M., 2014. Derivation of high-resolution MRI atlases of the human cerebellum at 3T and segmentation using multiple automatically generated templates. NeuroImage 95, 217–231. https://doi.org/10.1016/j.neuroimage.2014.03.037

152. Pascual-Marqui, R.D., Lehmann, D., Koukkou, M., Kochi, K., Anderer, P., Saletu, B., Tanaka, H., Hirata, K., John, E.R., Prichep, L., Biscay-Lirio, R., Kinoshita, T., 2011. Assessing interactions in the brain with exact low-resolution electromagnetic tomography. Philos. Trans. R. Soc. Math. Phys. Eng. Sci. 369, 3768–3784. https://doi.org/10.1098/rsta.2011.0081

153. Paulin, M.G., 2008. The Role of the Cerebellum in Motor Control and Perception. Brain. Behav. Evol. 41, 39–50. https://doi.org/10.1159/000113822

154. Pearl, J., 2009. Causality. Cambridge University Press.

155. Penny, W., Friston, K., Ashburner, J., Kiebel, S., Nichols, T., 2007. Statistical Parametric Mapping: The Analysis of Functional Brain Images, Statistical Parametric Mapping: The Analysis of Functional Brain Images. Elsevier Ltd. https://doi.org/10.1016/B978-0-12-372560-8.X5000-1

156. Piao, Y.S., Mori, F., Hayashi, S., Tanji, K., Yoshimoto, M., Kakita, A., Wakabayashi, K., Takahashi, H., 2003. α-Synuclein pathology affecting Bergmann glia of the cerebellum in patients with α-synucleinopathies. Acta Neuropathol. (Berl.) 105, 403–409. https://doi.org/10.1007/s00401-002-0655-0

157. Piccinin, C.C., Campos, L.S., Guimarães, R.P., Piovesana, L.G., dos Santos, M.C.A., Azevedo, P.C., Campos, B.M., de Rezende, T.J.R., Amato-Filho, A., Cendes, F., D'Abreu, A., 2017. Differential Pattern of Cerebellar Atrophy in Tremor-Predominant and Akinetic/Rigidity-Predominant Parkinson's Disease. Cerebellum 16, 623–628. https://doi.org/10.1007/s12311-016-0834-5

158. Plewes, D.B., Kucharczyk, W., 2012. Physics of MRI: A primer. J. Magn. Reson. Imaging 35, 1038–1054. https://doi.org/10.1002/jmri.23642

159. Poewe, W., Seppi, K., Tanner, C.M., Halliday, G.M., Brundin, P., Volkmann, J., Schrag, A.E., Lang, A.E., 2017. Parkinson disease. Nat. Rev. Dis. Primer 3, 1–21. https://doi.org/10.1038/nrdp.2017.13

160. Ponce-Alvarez, A., Deco, G., 2024. The Hopf whole-brain model and its linear approximation. Sci. Rep. 14, 2615. https://doi.org/10.1038/s41598-024-53105-0

161. Poston, K.L., Ua Cruadhlaoich, M.A.I., Santoso, L.F., Bernstein, J.D., Liu, T., Wang, Y., Rutt, B., Kerchner, G.A., Zeineh, M.M., 2020. Substantia Nigra Volume Dissociates Bradykinesia and Rigidity from Tremor in Parkinson's Disease: A 7 Tesla Imaging Study. J. Park. Dis. 10, 591–604. https://doi.org/10.3233/JPD-191890

162. Postuma, R.B., Berg, D., Stern, M., Poewe, W., Olanow, C.W., Oertel, W., Obeso, J., Marek, K., Litvan, I., Lang, A.E., Halliday, G., Goetz, C.G., Gasser, T., Dubois, B., Chan, P., Bloem, B.R., Adler, C.H., Deuschl, G., 2015. MDS clinical diagnostic criteria for

Parkinson's disease. Mov. Disord. Off. J. Mov. Disord. Soc. 30, 1591–1601. https://doi.org/10.1002/mds.26424

163. Pringsheim, T., Jette, N., Frolkis, A., Steeves, T.D.L., 2014. The prevalence of Parkinson's disease: A systematic review and meta-analysis. Mov. Disord. 29, 1583–1590. https://doi.org/10.1002/mds.25945

164. Priori, A., Ciocca, M., Parazzini, M., Vergari, M., Ferrucci, R., 2014. Transcranial cerebellar direct current stimulation and transcutaneous spinal cord direct current stimulation as innovative tools for neuroscientists. J. Physiol. 592, 3345–3369. https://doi.org/10.1113/jphysiol.2013.270280

165. Pyatigorskaya, N., Gallea, C., Garcia-Lorenzo, D., Vidailhet, M., Lehericy, S., 2014. A review of the use of magnetic resonance imaging in Parkinson's disease. Ther. Adv. Neurol. Disord. 7, 206–220. https://doi.org/10.1177/1756285613511507

166. Rahimi, S., Towhidkhah, F., Baghdadi, G., Forogh, B., Saadat, P., Soleimani, G., Habibi, S.A., 2023. Modeling of cerebellar transcranial electrical stimulation effects on hand tremor in Parkinson's disease. Front. Aging Neurosci. 15, 1187157. https://doi.org/10.3389/fnagi.2023.1187157

167. Reis, C., Sharott, A., Magill, P.J., van Wijk, B.C.M., Parr, T., Zeidman, P., Friston, K.J., Cagnan, H., 2019. Thalamocortical dynamics underlying spontaneous transitions in beta power in Parkinsonism. NeuroImage 193, 103–114. https://doi.org/10.1016/j.neuroimage.2019.03.009

168. Rezaee, Z., Dutta, A., 2019. Cerebellar lobules optimal stimulation (CLOS): A computational pipeline to optimize cerebellar lobule-specific electric field distribution. Front. Neurosci. 13. https://doi.org/10.3389/fnins.2019.00266

169. Rojas Albert, A., Backhaus, W., Graterol Pérez, J.A., Braaβ, H., Schön, G., Choe, C., Feldheim, J., Bönstrup, M., Cheng, B., Thomalla, G., Gerloff, C., Schulz, R., 2022. Cortical thickness of contralesional cortices positively relates to future outcome after severe stroke. Cereb. Cortex.

170. Rolls, E.T., Huang, C.C., Lin, C.P., Feng, J., Joliot, M., 2020. Automated anatomical labelling atlas 3. NeuroImage 206, 116189. https://doi.org/10.1016/j.neuroimage.2019.116189

171. Romero, J.E., Coupé, P., Giraud, R., Ta, V.-T.T., Fonov, V., Park, M.T.M., Chakravarty, M.M., Voineskos, A.N., Manjón, J.V., 2017. CERES: A new cerebellum lobule segmentation method. NeuroImage 147, 916–924. https://doi.org/10.1016/j.neuroimage.2016.11.003

172. Ronen, S., Gonçalves, B., Hu, K.Z., Vespignani, A., Pinker, S., Hidalgo, C.A., 2014. Links that speak: The global language network and its association with global fame. Proc. Natl. Acad. Sci. U. S. A. 111, E5616–E5622. https://doi.org/10.1073/pnas.1410931111

173. Rorden, C., Brett, M., 2000. Stereotaxic display of brain lesions. Behav. Neurol. 12, 191–200. https://doi.org/10.1155/2000/421719

174. Runge, J., 2015. Quantifying information transfer and mediation along causal pathways in complex systems. Phys. Rev. E 92, 062829. https://doi.org/10.1103/PhysRevE.92.062829

175. Rusholt, E.H.L., Salvesen, L., Brudek, T., Tesfay, B., Pakkenberg, B., Olesen, M.V., 2020. Pathological changes in the cerebellum of patients with multiple system atrophy and Parkinson's disease—a stereological study. Brain Pathol. 30, 576–588. https://doi.org/10.1111/bpa.12806

176. Ryman, S.G., Poston, K.L., 2020. MRI biomarkers of motor and non-motor symptoms in Parkinson's disease. Parkinsonism Relat. Disord. 73, 85–93. https://doi.org/10.1016/j.parkreldis.2019.10.002

177. Sadeghi, F., Banyeres, E. del A., Pizzuti, A., Okar, A., Grimm, K., Christian Gerloff, Morten L. Kringelbach, Rainer Goebel, Simone Zittel, Gustavo Deco, 2024. The Arrow of Time in Parkinson's Disease. Rev.

178. Sadeghi, F., Pötter-Nerger, M., Grimm, K., Gerloff, C., Schulz, R., Zittel, S., 2023. Smaller Cerebellar Lobule VIIb is Associated with Tremor Severity in Parkinson's Disease. Cerebellum 2023 1–8. https://doi.org/10.1007/S12311-023-01532-6

179. Sadeghihassanabadi, F., Frey, B.M., Backhaus, W., Choe, C. un, Zittel-Dirks, S., Schön, G., Bönstrup, M., Cheng, B., Thomalla, G., Gerloff, C., Schulz, R., 2022a. Structural cerebellar reserve positively influences outcome after severe stroke. Brain Commun. https://doi.org/10.1093/BRAINCOMMS/FCAC203

180. Sadeghihassanabadi, F., Misselhorn, J., Gerloff, C., Zittel, S., 2022b. Optimizing the montage for cerebellar transcranial alternating current stimulation (tACS): a combined computational and experimental study. J. Neural Eng. 19, 026060. https://doi.org/10.1088/1741-2552/ac676f

181. Saenger, V.M., Kahan, J., Foltynie, T., Friston, K., Aziz, T.Z., Green, A.L., Van Hartevelt, T.J., Cabral, J., Stevner, A.B.A., Fernandes, H.M., Mancini, L., Thornton, J., Yousry, T., Limousin, P., Zrinzo, L., Hariz, M., Marques, P., Sousa, N., Kringelbach, M.L., Deco, G., 2017. Uncovering the underlying mechanisms and whole-brain dynamics of deep brain stimulation for Parkinson's disease. Sci. Rep. 7, 1–14. https://doi.org/10.1038/s41598-017-10003-y

182. Sanz Perl, Y., Bocaccio, H., Pallavicini, C., Pérez-Ipiña, I., Laureys, S., Laufs, H., Kringelbach, M., Deco, G., Tagliazucchi, E., 2021. Nonequilibrium brain dynamics as a signature of consciousness. Phys. Rev. E 104, 1–6. https://doi.org/10.1103/PhysRevE.104.014411

183. Saturnino, G.B., Antunes, A., Thielscher, A., 2015. On the importance of electrode parameters for shaping electric field patterns generated by tDCS. NeuroImage 120, 25–35. https://doi.org/10.1016/J.NEUROIMAGE.2015.06.067

184. Saturnino, G.B., Madsen, K.H., Siebner, H.R., Thielscher, A., 2017. How to target inter-regional phase synchronization with dual-site Transcranial Alternating Current Stimulation. NeuroImage 163, 68–80. https://doi.org/10.1016/j.neuroimage.2017.09.024

185. Saturnino, G.B., Madsen, K.H., Thielscher, A., Guilherme B Saturnino, Kristoffer H Madsen, A.T., 2018. Electric field simulations for transcranial brain stimulation using FEM: an efficient implementation and error analysis. J. Neural Eng. 16, 0–13. https://doi.org/10.1088/1741-2552/ab41ba

186. Schiff, S.J., 2010. Towards model-based control of Parkinson's disease. Philos. Trans. R. Soc. Math. Phys. Eng. Sci. 368, 2269–2308. https://doi.org/10.1098/rsta.2010.0050

187. Schreglmann, S.R., Wang, D., Peach, R.L., Li, J., Zhang, X., Latorre, A., Rhodes, E., Panella, E., Cassara, A.M., Boyden, E.S., Barahona, M., Santaniello, S., Rothwell, J., Bhatia, K.P., Grossman, N., 2021. Non-invasive suppression of essential tremor via phase-locked disruption of its temporal coherence. Nat. Commun. 12, 1–15. https://doi.org/10.1038/s41467-020-20581-7

188. Schutter, D.J.L.G., Hortensius, R., 2010. Retinal origin of phosphenes to transcranial alternating current stimulation. Clin. Neurophysiol. 121, 1080–1084. https://doi.org/10.1016/j.clinph.2009.10.038

189. Schwarz, S.T., Rittman, T., Gontu, V., Morgan, P.S., Bajaj, N., Auer, D.P., 2011. T1-Weighted MRI shows stage-dependent substantia nigra signal loss in Parkinson's disease. Mov. Disord. 26, 1633–1638. https://doi.org/10.1002/mds.23722

190. Seif, A., Hafezi, M., Jarzynski, C., 2021. Machine learning the thermodynamic arrow of time. Nat. Phys. 17, 105–113. https://doi.org/10.1038/s41567-020-1018-2

191. Shah, B., Nguyen, T.T., Madhavan, S., 2013. Polarity independent effects of cerebellar tDCS on short term ankle visuomotor learning. Brain Stimulat. 6, 966–968. https://doi.org/10.1016/j.brs.2013.04.008

192. Sharott, A., Gulberti, A., Hamel, W., Köppen, J.A., Münchau, A., Buhmann, C., Pötter-Nerger, M., Westphal, M., Gerloff, C., Moll, C.K.E., Engel, A.K., 2018. Spatio-temporal dynamics of cortical drive to human subthalamic nucleus neurons in Parkinson's disease. Neurobiol. Dis. 112, 49–62. https://doi.org/10.1016/j.nbd.2018.01.001

193. Shettigar, N., Yang, C.-L., Tu, K.-C., Suh, C.S., 2022. On The Biophysical Complexity of Brain Dynamics: An Outlook. Dynamics 2, 114–148. https://doi.org/10.3390/dynamics2020006

194. Shirehjini, S.N., Shahrabi Farahani, M., Ibrahim, M.K., Salman, H.M., Motevalli, S., Mohammadi, M.H., 2023. Mechanisms of Action of Noninvasive Brain Stimulation with Weak Non-Constant Current Stimulation Approaches. Iran. J. Psychiatry 18, 72–82. https://doi.org/10.18502/ijps.v18i1.11415

195. SimNIBS Developers, 2019. Standard Conductivity Values [WWW Document]. URL https://simnibs.github.io/simnibs/build/html/documentation/conductivity.html?highlight=conduct

196. Sorrentino, P., Rucco, R., Baselice, F., De Micco, R., Tessitore, A., Hillebrand, A., Mandolesi, L., Breakspear, M., Gollo, L.L., Sorrentino, G., 2021. Flexible brain dynamics underpins complex behaviours as observed in Parkinson's disease. Sci. Rep. 11, 1–12. https://doi.org/10.1038/s41598-021-83425-4

197. Stebbins, G.T., Goetz, C.G., Burn, D.J., Jankovic, J., Khoo, T.K., Tilley, B.C., 2013. How to identify tremor dominant and postural instability/gait difficulty groups with the movement disorder society unified Parkinson's disease rating scale: Comparison with the unified Parkinson's disease rating scale. Mov. Disord. 28, 668–670. https://doi.org/10.1002/mds.25383

198. Stoodley, C.J., Desmond, J.E., Guell, X., Schmahmann, J.D., 2021. Functional Topography of the Human Cerebellum Revealed by Functional Neuroimaging Studies, in: Handbook of the Cerebellum and Cerebellar Disorders. Springer International Publishing, Cham, pp. 1–37. https://doi.org/10.1007/978-3-319-97911-3_30-2

199. Stoodley, C.J., Valera, E.M., Schmahmann, J.D., 2012. Functional topography of the cerebellum for motor and cognitive tasks: An fMRI study. NeuroImage 59, 1560–1570. https://doi.org/10.1016/j.neuroimage.2011.08.065

200. Strogatz, S., 2003. Synchronization: A Universal Concept in Nonlinear Sciences. Phys. Today 56, 47. https://doi.org/10.1063/1.1554136

201. Tahmasian, M., Bettray, L.M., van Eimeren, T., Drzezga, A., Timmermann, L., Eickhoff, C.R., Eickhoff, S.B., Eggers, C., 2015. A systematic review on the applications of resting-state fMRI in Parkinson's disease: Does dopamine replacement therapy play a role? Cortex 73, 80–105. https://doi.org/10.1016/j.cortex.2015.08.005

202. Takada, M., Sugimoto, T., Hattori, T., 1993. MPTP neurotoxicity to cerebellar Purkinje cells in mice. Neurosci. Lett. 150, 49–52. https://doi.org/10.1016/0304-3940(93)90105-T

203. Tavakoli, A.V., Yun, K., 2017. Transcranial alternating current stimulation (tACS) mechanisms and protocols. Front. Cell. Neurosci. 11, 214. https://doi.org/10.3389/fncel.2017.00214

204. Teufel, C., Fletcher, P.C., 2016. The promises and pitfalls of applying computational models to neurological and psychiatric disorders. Brain 139, 2600–2608. https://doi.org/10.1093/brain/aww209

205. The MathWorks, Inc., 2022. MATLAB version R2022b.

206. The MathWorks, Inc., 2021. MATLAB version R2021a.

207. Thielscher, A., Antunes, A., Saturnino, G.B., 2015. Field modeling for transcranial magnetic stimulation: A useful tool to understand the physiological effects of TMS?, in: Proceedings of the Annual International Conference of the IEEE Engineering in Medicine and Biology Society, EMBS. Institute of Electrical and Electronics Engineers Inc., pp. 222–225. https://doi.org/10.1109/EMBC.2015.7318340

208. Thut, G., Schyns, P., Gross, J., 2011. Entrainment of Perceptually Relevant Brain Oscillations by Non-Invasive Rhythmic Stimulation of the Human Brain. Front. Psychol. 2. https://doi.org/10.3389/fpsyg.2011.00170

209. Tomé, T., De Oliveira, M.J., 2012. Entropy Production in Nonequilibrium Systems at Stationary States. Phys. Rev. Lett. 108, 020601. https://doi.org/10.1103/PhysRevLett.108.020601

210. Toni, I., Bloem, B.R., Helmich, R.C., Hallett, M., Deuschl, G., Toni, I., Bloem, B.R., 2012. Cerebral causes and consequences of parkinsonian resting tremor : a tale of two circuits ? Brain 135, 3206–3226. https://doi.org/10.1093/brain/aws023

211. Tourbier, S., Rue-Queralt, J., Glomb, K., Aleman-Gomez, Y., Mullier, E., Griffa, A., Schöttner, M., Wirsich, J., Tuncel, M.A., Jancovic, J., Cuadra, M.B., Hagmann, P., 2022. Connectome Mapper 3: A Flexible and Open-Source Pipeline Software for Multiscale Multimodal Human Connectome Mapping. J. Open Source Softw. 7, 4248. https://doi.org/10.21105/joss.04248

212. Tournier, J.D., Smith, R., Raffelt, D., Tabbara, R., Dhollander, T., Pietsch, M., Christiaens, D., Jeurissen, B., Yeh, C.H., Connelly, A., 2019. MRtrix3: A fast, flexible and open software framework for medical image processing and visualisation. NeuroImage 202, 116137. https://doi.org/10.1016/j.neuroimage.2019.116137

213. Tsuzuki, D., Watanabe, H., Dan, I., Taga, G., 2016. MinR 10/20 system: Quantitative and reproducible cranial landmark setting method for MRI based on minimum initial reference points. J. Neurosci. Methods 264, 86–93. https://doi.org/10.1016/j.jneumeth.2016.02.024

214. Turi, Z., Ambrus, G.G., Janacsek, K., Emmert, K., Hahn, L., Paulus, W., Antal, A., 2013. Both the cutaneous sensation and phosphene perception are modulated in a frequency-specific manner during transcranial alternating current stimulation. Restor. Neurol. Neurosci. 31, 275–285. https://doi.org/10.3233/RNN-120297

215. Tustison, N.J., Avants, B.B., Cook, P.A., Zheng, Y., Egan, A., Yushkevich, P.A., Gee, J.C., 2010. N4ITK: Improved N3 bias correction. IEEE Trans. Med. Imaging 29, 1310–1320. https://doi.org/10.1109/TMI.2010.2046908

216. Van Den Berg, K.R.E., Helmich, R.C., 2021. The role of the cerebellum in tremor – evidence from neuroimaging. Tremor Hyperkinetic Mov. 11, 1–17. https://doi.org/10.5334/TOHM.660

217. van Eimeren, T., Monchi, O., Ballanger, B., Strafella, A.P., 2009. Dysfunction of the Default Mode Network in Parkinson Disease: A Functional Magnetic Resonance Imaging Study. Arch. Neurol. 66, 877–883. https://doi.org/10.1001/archneurol.2009.97

218. Van Rossum, G., Drake, F.L., 1995. Python reference manual. Centrum voor Wiskunde en Informatica Amsterdam.

219. Vandermeeren, Y., Jamart, J., Ossemann, M., 2010. Effect of tDCS with an extracephalic reference electrode on cardio-respiratory and autonomic functions. BMC Neurosci. 11, 1–10. https://doi.org/10.1186/1471-2202-11-38

220. Vignola, C., Necchi, D., Scherini, E., Bernocchi, G., 1994. MPTP-induced changes in the monkey cerebellum-immunohistochemistry of calcium-binding and cytoskeletal proteins. Neurodegeneration 3, 25–31.

221. Virtanen, P., Gommers, R., Oliphant, T.E., Haberland, M., Reddy, T., Cournapeau, D., Burovski, E., Peterson, P., Weckesser, W., Bright, J., van der Walt, S.J., Brett, M., Wilson, J., Millman, K.J., Mayorov, N., Nelson, A.R.J., Jones, E., Kern, R., Larson, E., Carey, C.J., Polat, İ., Feng, Y., Moore, E.W., VanderPlas, J., Laxalde, D., Perktold, J., Cimrman, R., Henriksen, I., Quintero, E.A., Harris, C.R., Archibald, A.M., Ribeiro, A.H., Pedregosa, F., van Mulbregt, P., 2020. SciPy 1.0: fundamental algorithms for scientific computing in Python. Nat. Methods 17, 261–272. https://doi.org/10.1038/s41592-019-0686-2

222. Wagner, T.A., Zahn, M., Grodzinsky, A.J., Pascual-Leone, A., 2004. Three-dimensional head model simulation of transcranial magnetic stimulation. IEEE Trans. Biomed. Eng. 51, 1586–1598. https://doi.org/10.1109/TBME.2004.827925

223. Washburn, S., Oñate, M., Yoshida, J., Vera, J., Bhuvanasundaram, R., Khatami, L., Nadim, F., Khodakhah, K., 2024. The cerebellum directly modulates the substantia nigra dopaminergic activity. Nat. Neurosci. 27, 497–513. https://doi.org/10.1038/s41593-023-01560-9

224. Weingarten, C.P., Sundman, M.H., Hickey, P., Chen, N., 2015. Neuroimaging of Parkinson's disease: Expanding views. Neurosci. Biobehav. Rev. 59, 16–52. https://doi.org/10.1016/j.neubiorev.2015.09.007

225. Wessel, M.J., Draaisma, L.R., Hummel, F.C., 2022. Mini-review: Transcranial Alternating Current Stimulation and the Cerebellum. Cerebellum. https://doi.org/10.1007/s12311-021-01362-4

226. West, T.O., Berthouze, L., Halliday, D.M., Litvak, V., Sharott, A., Magill, P.J., Farmer, S.F., 2018. Propagation of beta/gamma rhythms in the cortico-basal ganglia circuits of the parkinsonian rat. J. Neurophysiol. 119, 1608–1628. https://doi.org/10.1152/jn.00629.2017

227. West, T.O., Magill, P.J., Sharott, A., Litvak, V., Farmer, S.F., Cagnan, H., 2022. Stimulating at the right time to recover network states in a model of the cortico-basal ganglia-thalamic circuit. PLOS Comput. Biol. 18, e1009887. https://doi.org/10.1371/journal.pcbi.1009887

228. Wolters, A.F., van de Weijer, S.C.F., Leentjens, A.F.G., Duits, A.A., Jacobs, H.I.L., Kuijf, M.L., 2019. Resting-state fMRI in Parkinson's disease patients with cognitive impairment: A meta-analysis. Parkinsonism Relat. Disord. 62, 16–27. https://doi.org/10.1016/j.parkreldis.2018.12.016

229. Woods, A.J., Antal, A., Bikson, M., Boggio, P.S., Brunoni, A.R., Celnik, P., Cohen, L.G., Fregni, F., Herrmann, C.S., Kappenman, E.S., Knotkova, H., Liebetanz, D., Miniussi, C., Miranda, P.C., Paulus, W., Priori, A., Reato, D., Stagg, C., Wenderoth, N., Nitsche, M.A., 2016. A technical guide to tDCS, and related non-invasive brain stimulation tools. Clin. Neurophysiol. 127, 1031–1048. https://doi.org/10.1016/j.clinph.2015.11.012

230. Wu, T., Hallett, M., 2013. The cerebellum in Parkinson's disease. Brain 136, 696–709. https://doi.org/10.1093/brain/aws360

231. Wu, T., Wang, J., Wang, C., Hallett, M., Zang, Y., Wu, X., Chan, P., 2012. Basal ganglia circuits changes in Parkinson's disease patients. Neurosci. Lett. 524, 55–59. https://doi.org/10.1016/j.neulet.2012.07.012

232. Xu, S., He, X.-W., Zhao, R., Chen, W., Qin, Z., Zhang, J., Ban, S., Li, G.-F., Shi, Y.-H., Hu, Y., Zhuang, M.-T., Liu, Y.-S., Shen, X.-L., Li, J., Liu, J.-R., Du, X., 2019. Cerebellar functional abnormalities in early stage drug-naïve and medicated Parkinson's disease. J. Neurol. 266, 1578–1587. https://doi.org/10.1007/s00415-019-09294-0

233. Xue, A., Kong, R., Yang, Q., Eldaief, M.C., Angeli, P.A., DiNicola, L.M., Braga, R.M., Buckner, R.L., Thomas Yeo, B.T., 2021. The detailed organization of the human cerebellum estimated by intrinsic functional connectivity within the individual. J. Neurophysiol. 125, 358–384. https://doi.org/10.1152/jn.00561.2020

234. Yu, Y., Wang, X., Wang, Qishao, Wang, Qingyun, 2020. A review of computational modeling and deep brain stimulation: applications to Parkinson's disease. Appl. Math. Mech. Engl. Ed. 41, 1747–1768. https://doi.org/10.1007/s10483-020-2689-9

235. Zanin, M., Güntekin, B., Aktürk, T., Hanoğlu, L., Papo, D., 2020. Time Irreversibility of Resting-State Activity in the Healthy Brain and Pathology. Front. Physiol. 10, 1619. https://doi.org/10.3389/fphys.2019.01619

236. Zhong, Y., Liu, H., Liu, G., Zhao, L., Dai, C., Liang, Y., Du, J., Zhou, X., Mo, L., Tan, C., Tan, X., Deng, F., Liu, X., Chen, L., 2022. A review on pathology, mechanism, and therapy for cerebellum and tremor in Parkinson's disease. Npj Park. Dis. 8, 1–9. https://doi.org/10.1038/s41531-022-00347-2

Acknowledgement

Firstly, I would like to express my deepest gratitude to my supervisor and mentor, Dr. Simone Zittel, who invited me into her team and gave me the opportunity of a lifetime to pursue this PhD. Her guidance at every step and her emotional investment in this thesis have been invaluable. I will always be grateful for your belief in me, your support, and your mentorship, without which I would not be where I am today.

Special thanks go to Prof. Dr. Christian Gerloff, who provided life-changing guidance and support when I needed it most. He taught me to maintain a broad perspective and to be resilient and determined in pursuing my career.

I would also like to thank Prof. Gustavo Deco, whose generous and positive attitude was always heartwarming. His creative mind and innovative ideas, specially blending the worlds of neuroscience and physics, made working with him truly exciting.

Grateful acknowledgment to Prof. Dr. Andreas Engel and Prof. Dr. Claus Hilgetag for kindly agreeing to be on my thesis committee and evaluating my work.

Importantly, I extend my appreciation to the organizers and members of the European School of Network Neuroscience (euSNN) for making this amazing PhD program possible. They brought together great minds and gave me the opportunity to work with and learn from them. Heartfelt appreciation to Dr. Sina Alexa Trautmann-Lengsfeld, whose invaluable support throughout the PhD was a constant source of reassurance.

Furthermore, special recognition goes to my colleagues and friends in the Neurophysiology and Neuromodulation in Movement Disorders (MOVE) group, who generously shared their expertise and unwavering support. I also wish to express gratitude to all the fellow scientists with whom I have had the privilege of working and collaborating over these past three years. Special thanks to Dr. Robert Schulz, whose generous support and sharp insights always elevated the quality of my work, and Dr. Silke Wolf, whose timely support was instrumental to my success. Dr. med. Kai Grimm, Dr. med. Monika Pötter-Nerger, Dr. Jonas Misselhorn, Dr. Guido Nolte, Klaus Schellhorn, Elvira del Agua, and Alessandra Pizzuti, thank you—I had a wonderful time working with you!

Last but not least, I wish to thank my loving mother, my dear family, and my wonderful friends, whose love and prayers have accompanied me across long distances, and whose invaluable support has helped me through difficult times. I hope you are as proud of me as I am grateful to you.

Fatemeh

Eidesstattliche Versicherung

Ich versichere ausdrücklich, dass ich die Arbeit selbständig und ohne fremde Hilfe verfasst, andere als die von mir angegebenen Quellen und Hilfsmittel nicht benutzt und die aus den benutzten Werken wörtlich oder inhaltlich entnommenen Stellen einzeln nach Ausgabe (Auflage und Jahr des Erscheinens), Band und Seite des benutzten Werkes kenntlich gemacht habe.
Ferner versichere ich, dass ich die Dissertation bisher nicht einem Fachvertreter an einer anderen Hochschule zur Überprüfung vorgelegt oder mich anderweitig um Zulassung zur Promotion beworben habe.
Ich erkläre mich einverstanden, dass meine Dissertation vom Dekanat der Medizinischen Fakultät mit einer gängigen Software zur Erkennung von Plagiaten überprüft werden kann.

Unterschrift: .....  .....